A theoretical study of axion-like particle production by lasers and plasmas

PhD Thesis

Ruairidh McArthur

Strathclyde Intense Laser Interaction Studies (SILIS) group

Department of Physics

University of Strathclyde, Glasgow

August 25, 2026

Abstract

Axions/axion-like-particles (ALPs) are hypothetical particles, with their initial proposal aimed at solving the strong charge parity problem. They are now prominent candidates for dark matter and other astrophysical phenomena. Despite a significant international effort, ALPs have remained undetected. In this thesis, we provide a theoretical investigation into methods of producing substantial axion fluxes in laboratory contexts.

We derive the axion field that is produced from the overlap of two counter-propagating lasers. This is done using the framework of axion-photon oscillations which are akin to neutrino flavour oscillations. One laser (pump) is assumed to have a much larger amplitude than the other laser (probe) and their polarisations are chosen to maximise the axion flux. Conditions relating the energy of each field, laser and axion, are derived and govern the allowed axion parameters. This context allows for larger axion masses to be probed than what can typically be done using light-shining-through-a-wall experiments which suffer from decoherence for larger axion masses. For reasonable laser parameters, the theoretical produced axion flux is calculated and compared with that theoretically produced at the OSQAR experiment at CERN as well as at the ALPS II experiment at DESY.

We expand on previous work related to axion production via a longitudinally magnetised plasma wave, improving its accuracy. We account for the modal dependency of the axion's energy flux before calculating the average axion number flux. We demonstrate how the plasma frequency can be manipulated to fine-tune the produced flux and calculate that the produced axion flux, for reasonable laboratory parameters, is on the order of $N_\varphi \sim 10^{34}\ \mathrm{m}^{-2}\mathrm{s}^{-1}$, for axion parameters in the range where ADMX is searching for a dark-matter QCD axion.

Lastly, the axion flux produced from an electron, in a superposition of up and down spins, accelerated in a magnetic field, is calculated. An analytical derivation for the axion flux is illustrated, when the electron is in either the first or second level above its ground state, with numerical results given for larger mode numbers. The produced flux is found to have a significant amount of transverse spread in addition to having two distinct parameter regions which show either a sub-linear growth with mode number or decrease after the initial few modes.

Role of author

The work referenced in chapters 1 - 3 is taken from the wider literature and is not the work of the Author. In Chapter 4, Section 4.2, the derivation presented by the Author follows established results in the literature and has been adapted to the context of this work. The remaining derivations and analysis in Chapter 4 were carried out by the Author. Chapter 5 builds upon prior work in the field. The derivation of the oscillator equation and related material referenced in this chapter are not original contributions by the Author. The Author is responsible for the work found in Section 5.3 and onwards. In Chapter 6 the derivations and analysis presented are from the Author. All of this work was completed with the support of Dr. Adam Noble.

Contents

Abstract **ii**

Role of author **iv**

List of Figures **viii**

List of Tables **xiv**

Preface/Acknowledgements **xvi**

1 General Overview **2**

1.1 Introduction 2

1.2 Axion as an extension to electromagnetic theory 4

2 Background **12**

2.1 The strong CP problem 12

2.1.1 PQ solution to the CP problem 15

2.2 Axion detection 16

2.2.1 Laboratory based 17

2.2.2 Astrophysical 20

3 Notation Conventions and Key Equations **23**

3.1 Notation conventions 23

3.2 Key equations 25

3.2.1 The equations of motion 26
3.3 Table of symbols 29

4 Axion-Photon Oscillations in a Background Laser Field 32
4.1 Background on axion photon oscillations 32
4.2 Axion-Photon oscillations in a static magnetic field 34
4.3 Axion-Photon oscillations in a background laser field 36
4.4 Derivation of the coupled axion and laser equations 38
4.5 The propagating and flavour eigenstates 41
4.6 Boundary conditions and the axion number flux 43
4.6.1 Axion production by interaction of two laser beams 44
4.7 Analysis of the axion number flux 48
4.7.1 The flux dependency on axion mass 50
4.8 Axion-Photon oscillations starting with an axion 53
4.9 Numerical results 55
4.9.1 Suitable parameter values 55
4.9.2 Expected flux from axion-photon oscillations in a laser background 56
4.10 Dilaton 57
4.10.1 Dilaton production via two laser beam interactions 61
4.10.2 Dilaton-Photon oscillation starting with a dilaton 62
4.11 Chapter conclusions 63

5 Laser-Axion Interactions in Plasma 65
5.1 Plasma - a promising medium for axion searches 65
5.2 Background theory and summary of results 66
5.2.1 Deriving the axion field 69
5.3 The axion flux 72
5.4 Modal decomposition of the flux 74

5.4.1 Truncating the infinite series 76
5.5 Flux dependence on axion and plasma parameters 83
5.6 Comparisons with past and ongoing experiments 88
5.7 Dilaton 91
5.7.1 Approximate solutions by truncating the infinite series . . 100
5.8 Dependency of flux on dilaton and plasma parameters 101
5.8.1 Numerical dilaton flux estimates for idealised experiments 102
5.9 Chapter conclusion 103

6 Axion Fermionic Coupling 106

6.1 Axion fermionic coupling 106
6.2 The Dirac field of an electron in a constant magnetic field 108
6.3 The source of the axion field 112
6.4 Analysing the axion-Klein-Gordon equation 113
6.5 Calculating the axion modes using the Greens function 116
6.6 Calculating the axion field and axion flux 120
6.6.1 Determining the pseudoscalar and scalar contractions . . . 120
6.6.2 The charge density 122
6.6.3 The axion field 125
6.6.4 The axion flux 128
6.7 Analysing the axion flux 128
6.8 Dilaton 137
6.8.1 The dilaton field 137
6.9 Chapter conclusions 144

7 Summary 147

A Appendix 150

A.1 Derivation of the equations of motion 150

B Appendix **153**

B.1 Axion-Photon oscillations in a static magnetic field 153

B.1.1 Deriving the evolution equations 156

C Appendix **158**

C.1 Momentum and potentials 158

C.2 Derivation of the plasma wave oscillator equation 159

C.2.1 The wavelength of the oscillation 162

C.3 The axion Fourier series 164

D Appendix **165**

D.1 Gamma, Pauli matrices and conserved currents 165

D.2 Expanding out the Dirac equation 167

D.3 Deriving the Greens function 168

D.4 The momentum modulation 170

D.5 The transverse modes of the axion field 170

Bibliography **173**

List of Figures

1.1 A global map indicating the experiments aimed at detecting ALPs, their scalar/vector cousins, and dark photons including those experiments residing in space. 9

1.2 An exclusion plot of the axion electromagnetic coupling. The diagonal yellow band indicates the parameter space in which the QCD axion must reside. Much of the area for stronger couplings has been excluded by experiments but there are some gaps around the optical frequencies that makes laser axion production particularly interesting. Large portions of the map for heavier axions have been excluded on astrophysical and cosmological grounds. 10

1.3 An exclusion plot of the axion fermionic coupling. The diagonal yellow band indicates the parameter space in which the QCD axion must reside. 11

4.1 The axion flux vs oscillation frequency. The oscillation frequency varies from 0.1% to 0.5% of the background laser's frequency. . . . 47

4.2 The flux increases and oscillates due to the increase in axion mass. The slow oscillation frequency is $\omega = 0.1\omega_A$. 51

4.3 The flux initially increases over consecutive oscillations due to the increased axion mass before tending to zero. The slow oscillation frequency is $\omega = 0.5\omega_A$. 51

4.4 The axion flux as a function of the interaction length. The background laser frequency is $\omega_A = 0.5$ eV and the slow oscillation frequency has been set to $\omega = 1n$eV. 53

5.1 Comparison of the axion's spectral and averaged number flux. The dimensionless parameter ranges from $s = 0.24 - 1.22$ in the graph. The averaged number flux over counts for $s < 1$ and diverges from the number flux of this work. 69

5.2 Comparison of the axion spectral and averaged flux. The dimensionless parameter ranges from $s = 0.69 - 3.44$ in the graph. Both fluxes are close in value for $s \approx 1$. 70

5.3 Comparison of the axion's spectral and averaged flux. The dimensionless parameter ranges from $s = 7.70 - 38.46$ in the graph. . . . 71

5.4 The finite-sum $H_N(s)$ is shown for the continuous variable s. The peak occurs at $s = 0.59$ with a value of 0.687, and the vertical lines mark the peak, two-thirds peak, and half-peak positions which occur at 0.25, 1.19 and 0.17, 1.47 respectively. 75

5.5 When $s = 0.01$ $h_1(s)$ the flux contribution comprising roughly 96% of the total flux. 76

5.6 Even for $s = 1$ $h_n(1)$ drops off rapidly as $s < n$. $h_1(1)$ contributes approximately 91% of the total flux. 77

5.7 As s gets larger the contributions from each consecutive $h_n(s)$ mode become comparable. In this example $h_1(100)$ contributes roughly 21% of the total flux. 78

5.8 For the orange curve the parameter s will always be less than the mode number resulting in the flux being inversely proportional to n^5. For the red curve, initially $s \gg n$ causing a linear drop-off with n. However, there will exist a set of mode numbers for which $s \ll n$ and the flux's relationship with the mode number will change - see Figure 5.9. 79

5.9 Again, for the orange curve we have $s \ll 1$ and the same relationship as seen in Figure 5.8 is shown. For the red curve, in this range of mode numbers $s \ll n$ and the flux's relationship with mode number is now inversely proportional to n^5. 80

5.10 The total axion number flux for an increasing axion mass. The maximum value of the dimensionless parameter reached in this scan is $s = 2.2$. Additionally, 100 modes have been summed for each value of the axion mass to give the total flux. 84

5.11 Increases in γ leads to a rapid increase in the number flux. The maximum value of the dimensionless parameter reached in this scan is $s = 1.8$ (black curve) and $s = 0.36$ (blue curve). Additionally, 100 modes have been summed for each value to give the total flux. 85

5.12 The total axion number flux for an increasing γ factor. The maximum value of the dimensionless parameter reached in this scan is $s = 1.74$ (black curve) and $s = 0.35$ (blue curve). Additionally, 100 modes have been summed for each value to give the total flux. 86

5.13 Axion flux as a function of plasma frequency. The maximum value of the dimensionless parameter reached in this scan is $s = 4.1$. Additionally, 100 modes have been summed for each value to give the total flux. 87

5.14 The produced number flux vs γ for $\gamma = (500 - 10,000)$. The growth of the curve slows down as γ is increased, resembling that of a graph of $y = \sqrt{x}$. 89

5.15 When $s = 0.01$ the first mode dominates the flux contribution comprising roughly 99% of the total flux. 97

5.16 For $s = 1$ the flux contribution per mode continues to drop off rapidly as $s < n$. The first mode contributes approximately 97% of the total flux. 98

5.17 Even as s gets larger and is greater than half of the modes the contribution from each consecutive mode still drops off steeply. In this example the first contributes roughly 83% of the total flux. . 99

5.18 Variation in the dilaton's number flux with dilaton mass. The maximum value of the dimensionless parameter reached in this scan is $s = 2.18$. 102

5.19 The total dilaton number flux for increasing plasma frequency. The maximum value of the dimensionless parameter reached in this scan is $s = 4.1$ 103

5.20 The total dilaton flux for an increasing γ. Plots for two different dilaton masses are shown. The maximum value of the dimensionless parameter reached in this scan is $s = 1.80$ (black curve) and $s = 0.36$ (blue curve). 104

5.21 The total dilaton flux for an increasing plasma frequency. Plots for two different frequencies are shown. The maximum value of the dimensionless parameter reached in this scan is $s = 0.36$ (black curve) and $s = 0.07$ (blue curve). 105

6.1 Transverse variation of the flux for modes $n = 1$–4 for $\bar{\omega} = 10$. The peak position of the flux is at $\bar{x} = 1.13$, $\bar{x} = 1.65$, $\bar{x} = 2.08$, $\bar{x} = 2.45$, respectively. 129

6.2 Transverse variation of the flux for modes $n = 5–8$ for $\bar{\omega} = 10$. The peak position of the flux is at $\bar{x} = 2.78$, $\bar{x} = 3.10$, $\bar{x} = 3.37$, $\bar{x} = 3.63$, respectively. 130
6.3 Transverse variation of the flux for modes $n = 9–12$ for $\bar{\omega} = 10$. The peak position of the flux is at $\bar{x} = 3.88$, $\bar{x} = 4.11$, $\bar{x} = 4.33$, $\bar{x} = 4.54$, respectively. 130
6.4 Transverse variation of the flux for modes $n = 1–12$ for $\bar{\omega} = 0.0001$. The peak values of the flux are closer to the origin and are located at $\bar{x} = 1.01$, $\bar{x} = 0.00$, $\bar{x} = 0.30$, $\bar{x} = 0.00$, $\bar{x} = 0.20$, $\bar{x} = 0.00$, $\bar{x} = 0.10$, $\bar{x} = 0.00$, $\bar{x} = 0.10$, $\bar{x} = 0.00$, respectively. 131
6.5 Peak flux versus mode number for $\bar{\omega} = 7.42 \times 10^{-6}$. The peak flux increases with mode number but at a decreased rate. The peak flux is near $\bar{x} = 0$ with it alternating between $\bar{x} = 0$ and $\bar{x} \leq 1$ for the modes sampled. 134
6.6 Peak flux versus mode number for $\bar{\omega} = 10$. The peak flux is largest in one of the initial modes after which it decreases with mode number. The transverse position of the peak flux increases with mode number. 135
6.7 Transverse variation of the flux for modes $n = 1–4$. The peak flux is at a position of $\bar{x} = 0.86$, $\bar{x} = 1.53$, $\bar{x} = 2.00$, $\bar{x} = 2.40$ respectively. 140
6.8 Transverse variation of the flux for modes $n = 5–8$. The peak flux is at a position of $\bar{x} = 2.74$, $\bar{x} = 3.06$, $\bar{x} = 3.34$, $\bar{x} = 3.61$ respectively. 140
6.9 Transverse variation of the flux for modes $n = 9–12$. The peak flux is at a position of $\bar{x} = 3.86$, $\bar{x} = 4.09$, $\bar{x} = 4.32$, $\bar{x} = 4.53$ respectively. 141
6.10 Transverse variation of the flux for modes $n = 1–12$ for $\bar{\omega} = 0.0001$. The peak values of the flux are all located at $\bar{x} = 0$. 141

6.11 The change in the peak flux with mode number for $\bar{\omega} = 10$. The peak flux and location of the peak increase with mode number. . . 142

6.12 The change in the peak flux with mode number for $\bar{\omega} = 7.42 \times 10^{-6}$. The peak flux grows linearly with mode number, with the location of the peak being always being at $\bar{x} = 0$. 143

6.13 The peak dilaton flux vs mode number. A fit of the form $f(n) = an + b$ has been applied to the whole data set. The R^2 of the fit is 0.9999. 143

6.14 The peak dilaton flux vs mode number. A fit of the form $f(n) = a\sqrt{n} + b$ has been applied to a subset of the data beginning with $n = 5$. The R^2 of the fit is 0.9934. 144

D.1 The plot of the modulation applied to the longitudinal momentum of the electrons. This was chosen for its mathematical convenience whilst have a Gaussian-like shape. 170

List of Tables

3.1 Table of Symbols 29

5.1 Upper bound on the mode number needed to obtain an approximation of the closed form result 82

6.1 The dominant terms $\bar{\omega}$ depends on, and the corresponding axion mass for an electron energy spread of $\delta = 0.66$ eV 133

6.2 The dominant terms $\bar{\omega}$ depends on, and the corresponding axion mass for an electron energy spread of $\delta = 1$ MeV 133

6.3 Energy flux for $\bar{\omega} = 7.42 \times 10^{-6}$ measured at $\bar{x} = 0$. 135

6.4 Extrapolated peak dilaton flux, $\bar{\omega} = 7.42 \times 10^{-6}$ 145

Preface/Acknowledgements

I would like to thank both of my supervisors, Prof. Dino Jarozszynski and Dr. Adam Noble for their constant support throughout my PhD. I would especially like to thank Dr. Adam Noble, who helped me through every part of my PhD journey and who was always available for chats whenever I got panicked or lost my way. I would also like to extend my gratitude to both Dr.Bernhard Ersfeld and Dr. Samuel Yoffe who each helped me with their technical knowledge.

Chapter 1

General Overview

1.1 Introduction

The last century in physics has seen many paradigm shifts in how we view and quantify the universe. Our most accurate theory of the universe is quantum electrodynamics (QED), a type of quantum field theory (QFT) of which, in general, there are many. The most famous and one of the great achievements in physics, is the development of the standard model (SM) of particle physics. It describes all the known forces (excluding gravity) in addition to the elementary particles. In spite of its successes there are phenomena observed in the universe that are incompatible with the SM. These unanswered mysteries include: the absence of antimatter in the universe, where models suggest both matter and anti-matter should have been created equally [1]. The observed gravitational effects of many galaxies cannot fully be accounted for by their matter content, which has led to the postulate of the existence of unseen dark-matter (DM) [2–4]. Furthermore, observations, on the cosmological scale, of the expansion of the universe indicate an unknown energy, dark-energy, that drives it [5–7]. Experimental evidence shows that neutrinos, an abundant subatomic particle, oscillate between the three flavours [8–10] thereby requiring them to be massive when the SM implies that they are massless. Another example of an issue with the SM is that the theory of the strong force suggests that it should favour particular processes linked to their 'handedness', while in reality no such preferences are observed. This final issue is known as the strong charge parity (CP) problem, which will be more extensively discussed in Section 2.1.

Note that the SM is by no means a complete description of observed phenomena, and it is well known that additional theories are required. Many of these extensions to the SM predict a plethora of beyond-the-standard model (BSM) particles, in what is known as the 'hidden sector' [11]. This is an important area of physics given the above stated 'mysteries'. Many of theses 'hidden' particles are well motivated candidates to resolve these issues. Theories such as string theories and supersymmetric theories naturally[1] predict particles such as the sterile neutrino [12] [2], dark photon[3] as well as axions and dilatons [13].

The axion is of particular interest, and axion-like particles (ALPs) will be the central focus of this thesis, with the dilaton additionally investigated and compared with the axion. For various cosmological reasons, many of these particles – known collectively as WIMPs/WISPs (weakly interacting massive/slim particles) – would have been produced in abundance in the early universe. Furthermore, the axion also originates from the Peccei-Quinn (PQ) solution [14, 15] to the aforementioned strong CP problem. Wilczek and Weinberg [16, 17] pointed out that the PQ solution should lead to a new boson via the spontaneous breaking of a global symmetry. Wilczek coined the name axion, after a detergent brand, as he felt it would 'clean up' an issue in physics. Since then the axion and ALPs – a larger family of particles with similar couplings to the axion – have been actively

[1] By this we mean the particles are a consequence of the building blocks of the theory in question.

[2] This particle is relevant to the question 'are all neutrinos left handed?' (opposite for antiparticles).

[3] Given the rich interaction of matter with light, does DM have an equivalent? If so, then there might be dark photons.

sought after from many areas of physics.

In brief, axions are pseudoscalar particles that have no charge and are spin zero. They typically have very low mass (sub eV), which arises from the fact that the spontaneously broken Goldstone symmetry was an approximate symmetry. Additionally, they would have been produced in copious amounts during the early universe via the vacuum misalignment mechanism [18]. In addition, they are very long lived particles with a characteristic lifetime greater than the age of the universe. These qualities have made them an ideal candidate for DM searches [19–23]. The axion couples to the electromagnetic field via a two-photon interaction, which is the primary mechanism exploited in detection experiments. Common methods used in such experiments include light-shining-through-wall (LSW) experiments, and cavity searches. The former attempts to detect axions converting to photons in a chamber which blocks external electromagnetic (E-M) waves from entering, and the latter has the cavity tuned to the axion's mass to detect a stimulated decay from axion to photon, which results in an increase in power in the cavity. The axion's mass and coupling strength are unknown parameters and to date no axions have been detected, but experiments around the world are placing ever more stringent bounds on its mass and coupling to the electromagnetic field. See Figure 1.1 for a picture of the global experimental activity; Figures 1.1 - 1.3 have been taken from [24].

1.2 Axion as an extension to electromagnetic theory

Before we discuss more detail on the axion and its origins arising from the CP problem, we introduce the axion in a more general way, considering the simplest extension to Maxwell's electrodynamics. Extensions to theories are a useful tool in physics, providing explanations for phenomena incompatible with the SM, without undermining its many successes. The aforementioned dilaton originates from Kaluza-Klein theory, an extension of Einstein's general relativity to five dimensions [25]. The dilaton is the fifth diagonal element of the metric tensor of this theory. In addition, in many string theories the dilaton appears alongside gravity. Likewise, many supersymmetric theories predict axion-particles [13, 26].

Electromagnetism expressed in the language of the Lagrangian density has the following form:

$$\mathcal{L}_{em} = -\frac{1}{4}F^{\mu\nu}F_{\mu\nu} - A_\mu J_e^\mu, \tag{1.1}$$

where $F^{\mu\nu}$ is the electromagnetic field tensor with $F_{0i} = E_i$ and $B^i = -\frac{1}{2}\epsilon_{ijk}F^{jk}$, where ϵ is the totally antisymmetric Levi-Civita tensor. A_μ is the electromagnetic 4 vector potential, J_e^μ the 4 current and E_i and B^i are components of the electric and magnetic fields, respectively. The field tensor is defined by the 4 potential as $F^{\mu\nu} = \partial^\mu A^\nu - \partial^\nu A^\mu$, where the field tensor is antisymmetric.

The simplest particle that could couple to E-M fields would be a spinless scalar particle, which can be described by the Klein-Gordon (KG) Lagrangian

$$\mathcal{L}_\varphi = \frac{\partial_\mu\varphi\partial^\mu\varphi}{2} - \frac{m_\varphi^2\varphi^2}{2}. \tag{1.2}$$

Coupling such a particle to an E-M field is determined by a term in the Lagrangian proportional to the product of the new particle's field with the electromagnetic field. In electromagnetism there are only two Lorentz invariant terms, $F^{\mu\nu}F_{\mu\nu}$ and $\tilde{F}^{\mu\nu}F_{\mu\nu}$ (where $\tilde{F}^{\mu\nu} = \frac{1}{2}\epsilon^{\mu\nu\alpha\beta}F_{\alpha\beta}$ is the dual field tensor), and therefore we will consider two beyond the standard model (BSM) particles, described by the free Lagrangian of (1.2), with one coupled to each of the electromagnetic invariants

$$\mathcal{L}_{int,\phi} = -\frac{1}{2} g_{\Phi\gamma} \Phi F^{\mu\nu} F_{\mu\nu} \tag{1.3}$$
$$\mathcal{L}_{int,\varphi} = -\frac{1}{4} g_{\varphi\gamma} \varphi \tilde{F}^{\mu\nu} F_{\mu\nu}, \tag{1.4}$$

where the BSM particles are denoted by the symbols ϕ and φ.

In this context, the total Lagrangian is constructed by summing the Maxwell Lagrangian, the KG Lagrangian, and the interaction Lagrangian that couples the particle to the electromagnetic field:

$$\mathcal{L}_T = \mathcal{L}_{em} + \mathcal{L}_{\varphi} + \mathcal{L}_{int,\varphi}. \tag{1.5}$$

A similar total Lagrangian can be obtained for the particle ϕ coupled to E-M.

Using the Euler-Lagrange equation one can show that each of these particles is described by the Klein-Gordon equations

$$\left(\Box + m_{\varphi}^2\right) \varphi = -\frac{g_{\varphi\gamma}}{4} \tilde{F}^{\mu\nu} F_{\mu\nu} = -g_{\varphi\gamma} \mathbf{E} \cdot \mathbf{B} \tag{1.6}$$
$$\left(\Box + m_{\phi}^2\right) \phi = -\frac{g_{\Phi\gamma}}{2} F^{\mu\nu} F_{\mu\nu} = g_{\Phi\gamma} (\mathbf{E^2} - \mathbf{B^2}). \tag{1.7}$$

From the source terms in the equations of motion, we identify φ as a pseudoscalar and ϕ as a scalar field. This distinction arises from their coupling to the electromagnetic invariants: $\tilde{F}^{\mu\nu} F_{\mu\nu}$ and $F^{\mu\nu} F_{\mu\nu}$, respectively. By extending electromagnetic theory to include spinless scalar fields, we obtain a framework that accommodates particles with axion-like interactions with light. In this context, the pseudoscalar field φ resembles the axion, whilst the scalar field ϕ resembles the dilaton, a charge neutral scalar field originally arising in Kaluza–Klein and string theories, and coupling to the scalar electromagnetic invariant. Such extensions serve as valuable interim models in the development of more complete theories.

There is strong motivation to augment the Standard Model with BSM particles. Although the QCD axion was introduced to solve the strong CP problem, its defining parameters, particle mass and its couplings to photons, depend on model-dependent coefficients and are not fixed uniquely by QCD. This observation motivates searches for axion-like particles (ALPs): pseudoscalar bosons that share the QCD axion's photon coupling but whose mass and coupling strength are independent parameters and do not need be tied to the strong CP solution. As Hook asks [27]: "If we're searching for a particle whose couplings are unrelated to the strong CP problem, why must it solve the strong CP problem?".

To avoid ambiguity, we define the terminology used throughout this thesis as follows:

QCD Axion - The pseudo-Goldstone boson generated from the spontaneous breaking of the PQ symmetry. This particle solves the CP problem. There is an explicit relationship between the coupling strength and mass of the QCD axion. In axion exclusion plots (see Figures 1.2, 1.3) this is often characterized by a diagonal line of constant thickness on the coupling vs mass graph.

ALP - A pseudoscalar particle that interacts with electromagnetic fields, as the QCD axion does, but its properties do not necessarily solve the CP problem, nor is the particle necessarily a result of the breaking of the PQ symmetry. For ALPs there is no explicit relationship between the coupling strength and mass, making them two independent parameters.

Axion - From this point onwards, this term will be interchangeable with ALP.

Dilaton - The term "dilaton" is used in this thesis in a broad sense. Historically, the dilaton arises from Kaluza–Klein theory as the scalar component of a higher-dimensional metric, which, after dimensional reduction, couples to the scalar electromagnetic invariant $F^{\mu\nu}F_{\mu\nu}$. In this respect, the KK dilaton acts as a scalar partner to electromagnetism, modulating the strength of the Maxwell term. The scalar field introduced in this thesis plays an analogous role: it is a charge-zero scalar that couples to the scalar electromagnetic invariant. Although the field does not necessarily originate from extra dimensions, its coupling structure and physical function mirror those of the KK dilaton, justifying the use of the same terminology. This usage is common in beyond-Standard-Model contexts, though not universally adopted, and is therefore stated explicitly here

Although many axion searches rely only on order-of-magnitude estimates, the purpose of this thesis is different: we aim to understand in detail how different production mechanisms depend on the underlying field dynamics. The axion flux in laser–laser, laser–plasma and fermionic systems is highly sensitive to resonance conditions, phase matching, modal structure and the spectral content of the driving fields. These features cannot be captured by simple scaling arguments. For this reason the derivations presented in each chapter retain the full dependence on the relevant parameters, allowing us to identify where enhancements occur. Furthermore, this enables us to probe different mass ranges, and investigate how the theoretical limits compare across production methods. The detailed expressions therefore serve not only to obtain flux estimates, but to reveal the physical structure of each mechanism.

The remainder of the thesis proceeds as follows: Chapter 2 reviews the strong CP problem and the Peccei–Quinn solution that introduces the axion, and Section 2.2 summarises experimental architectures for detecting axions and axion-like particles. Chapter 3 lays out the notation and conventions used throughout the the-

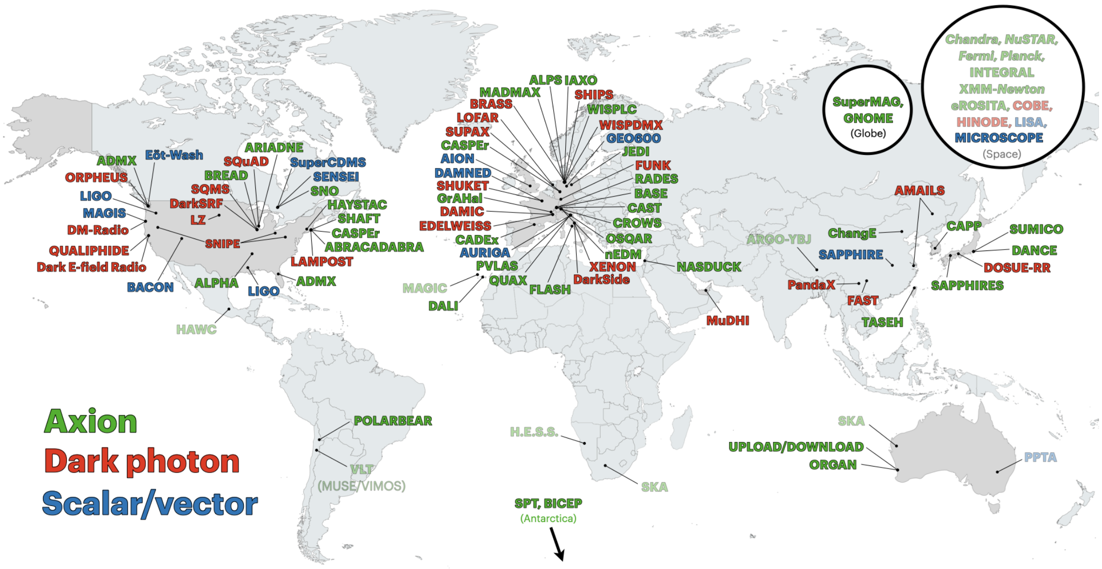

Figure 1.1: A global map indicating the experiments aimed at detecting ALPs, their scalar/vector cousins, and dark photons including those experiments residing in space.

sis. Chapter 4 derives the coupled differential equations describing axion–photon oscillations in a background laser field and presents numerical estimates of the resulting photon and axion fluxes, with comparisons to existing experiments. Chapter 5 explores axion production via driven plasma waves, improving on previous treatments and computing axion number fluxes for comparison with the literature. Chapter 6 treats axion production from fermionic couplings, deriving analytical expressions for the axion energy flux produced by an electron in the presence of a magnetic field. Chapter 7 summarises the main results and outlines directions for future work.

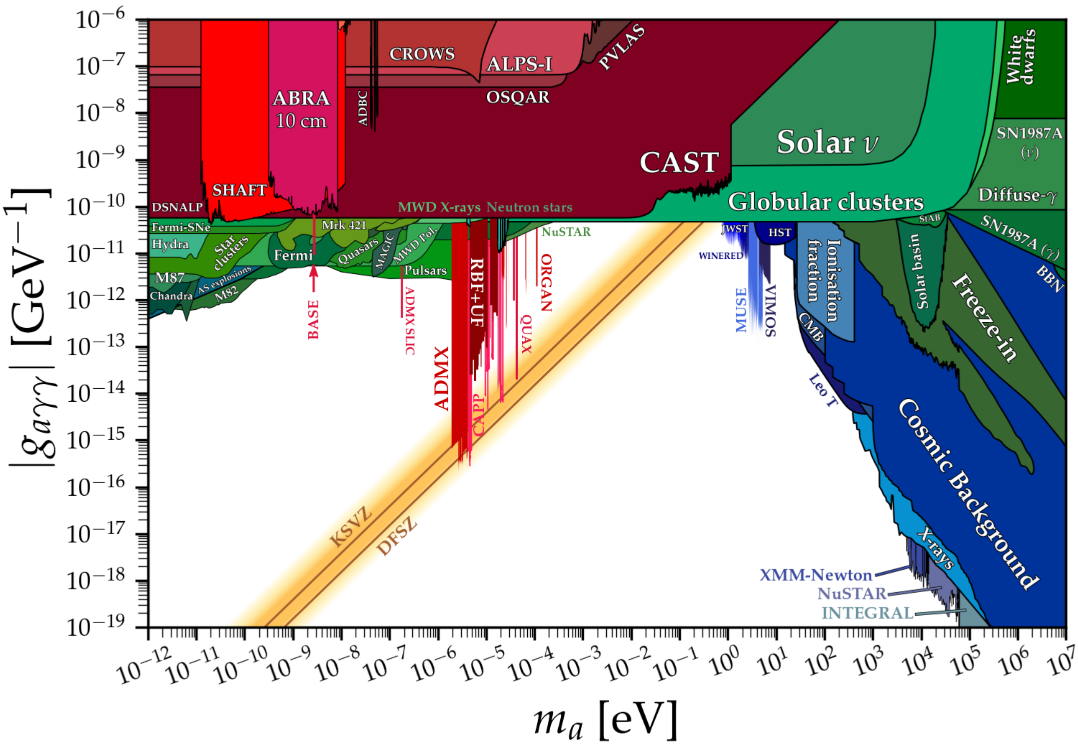

Figure 1.2: An exclusion plot of the axion electromagnetic coupling. The diagonal yellow band indicates the parameter space in which the QCD axion must reside. Much of the area for stronger couplings has been excluded by experiments but there are some gaps around the optical frequencies that makes laser axion production particularly interesting. Large portions of the map for heavier axions have been excluded on astrophysical and cosmological grounds.

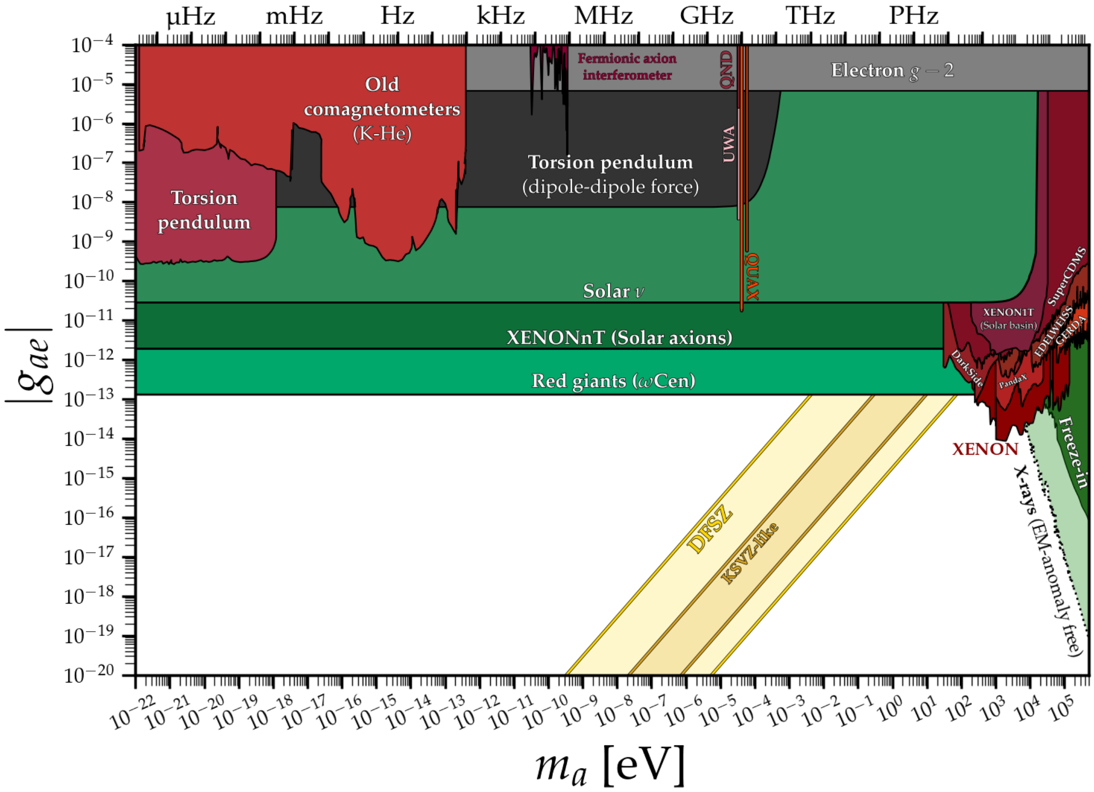

Figure 1.3: An exclusion plot of the axion fermionic coupling. The diagonal yellow band indicates the parameter space in which the QCD axion must reside.

Chapter 2

Background

2.1 The strong CP problem

As we have already mentioned, the axion itself is a by-product of a solution to the strong CP problem, and this therefore is a natural starting point for discussion on ALPs and axions.

The strong CP problem within the framework of the standard model is specific to quantum chromodynamics (QCD), an area of physics that deals with the strong interactions between quarks and gluons. The symmetries C (charge conjugation), P (parity transformation), and T (time reversal), are fundamental symmetries in nature, and Lorentz invariant systems must respect the composition CPT [28]. QCD, a non-abelian quantum field theory (QFT) based on the symmetry group SU(3), might naively be expected to respect these symmetries. Experimentally, this is exactly what we observe. The QCD Lagrangian density could naively[1] be written as:

$$\mathcal{L}_{QCD} = -\frac{1}{4} G^a_{\mu\nu} G^{\mu\nu}_a + \sum_{i=1}^{N} \bar{q}^i \left(\gamma^\mu D_\mu - m_i\right) q^i, \tag{2.1}$$

[1]Without knowing the complex nature of the vacuum one would not add instanton solutions - this was pointed out by 't Hooft [29].

where G is the gluon field strength tensor and q are the quarks with the last term being the Dirac Lagrangian for the quarks.

Weinberg realised, however, that there is a CP violating chiral symmetry in this Lagrangian, $U(1)_A$ [30]. This issue was later resolved by 't Hooft [29] who pointed out the non-trivial nature of the QCD vacuum and that instanton solutions must be added [31,32]. In short, the $U(1)_A$ symmetry was anomalous - higher-order quantum corrections resulted in what was thought to be a conserved current becoming non-vanishing. For our purposes, an additional term, the theta term, is added to the QCD Lagrangian:

$$\mathcal{L}_{QCD} \subset \theta \frac{g^2}{32\pi^2} G_a^{\mu\nu} \tilde{G}^a_{\mu\nu}, \tag{2.2}$$

where $\tilde{G}$ is the dual tensor and g is a coupling parameter, the specific details of which are not important for the purposes of this thesis.

Analogous to electromagnetism we can view the QCD field strength tensors as being QCD electric and magnetic fields that can express the contraction in (2.2) as

$$G_a^{\mu\nu} \tilde{G}^a_{\mu\nu} \propto \mathbf{E}^a \cdot \mathbf{B}_a. \tag{2.3}$$

Although a total derivative, this term cannot be ignored and does result in physical observations when analysed non-perturbatively, which is required in QCD[2].

Nevertheless, while the $U(1)_A$ problem is resolved via instanton effects, this does not eliminate the CP violating nature of the QCD Lagrangian. The θ term, given in equation (2.2), couples the gluonic electric and magnetic fields, which transform differently. The electric (QCD) field is odd under parity transformations, whereas the magnetic (QCD) field is even. Consequently, their scalar

[2]For this thesis the consequence rather than the reasons for this are important.

product is CP violating. This is the origin of the strong CP problem, as experimentally no such violations are observed. As we shall see, the CP problem is really an issue of fine tuning.

A common way to experimentally investigate CP violation in the strong sector is through the electric dipole moment (EDM) that the neutron would acquire. Of the various ways to calculate this value, the lattice QCD sum rules [33] is the most quoted. Currently, experimental efforts to measure this quantity have resulted in null results, but give an upper bound on the magnitude of this EDM:

$$|d_n| \leq 3.6 \times 10^{-26} e \cdot \mathrm{cm} \tag{2.4}$$

at a 95% C.L. (confidence level). This bound can then be re-expressed as a restriction on the QCD angle [34]:

$$|\theta| \leq 10^{-9}. \tag{2.5}$$

This is a very surprising result, as the QCD angle can be expressed, via chiral transformations, as the sum of two parts written as:

$$\bar{\theta} = \theta_{QCD} + \arg\ \mathrm{Det}[M], \tag{2.6}$$

where M is the quark mass matrix.

This new term, $\bar{\theta}$, violates CP symmetry. As discussed above, experimental bounds on the neutron EDM constrain θ to be less than 10^{-9}, a result that is both surprising and theoretically troubling. The issue of fine-tuning becomes clear when one realises that the two contributions to $\bar{\theta}$ (θ and arg Det$[M]$) arise from entirely distinct physical mechanisms. Their perfect cancellation lacks any known symmetry-based justification within the standard model. If θ were sufficiently large to produce observable CP violation, it would manifest as a measurable neutron EDM, yet no such effect has been detected. This is the origin of the strong CP problem. The question then arises: why has nature set these completely unrelated parameters to cancel so precisely? For some, the notion of this fine-tuning is sufficient motivation to seek an answer to the strong CP problem.

There are various proposals to rectify this: such as massless quark models. However, here we will focus on a solution suggested by Peccei and Quinn [35]. Other proposals for resolving the CP problem can be found in Refs. [18, 36]

2.1.1 PQ solution to the CP problem

Peccei and Quinn [35] proposed the existence of a new field, φ, (the axion field) and a new global chiral symmetry $U(1)_{PQ}$, which is spontaneously broken at energies proportional to f_φ, the decay constant of the axion. This new field (φ) modifies the term proportional $\tilde{G}G$ in (2.2)[3]. Ultimately, the theta term is cancelled from a PQ symmetry transformation. The necessity for instantons in QCD results in an axion potential, which is minimised when $\varphi = -f_\varphi \bar{\theta}$ (the vacuum expectation value of the axion being opposite and equal to the theta term):

$$\mathcal{L}_{\bar{\theta}+\varphi} \propto \left(\cancel{\bar{\theta} + \frac{\varphi}{f_\varphi}} \right) \frac{g^2}{32\pi^2} G_a^{\mu\nu} \tilde{G}_{a\mu\nu} \tag{2.7}$$

For these reasons the PQ solution to the strong CP problem is sometimes referred to as a dynamical solution.

The initial axion model, known as the PQWW (Peccei, Quinn, Weinberg, Wilczek) [16, 17] was quickly ruled out due to disagreement with branching ratios [37]. Consequently, the energy scale at which the PQ symmetry is spontaneously

[3] This is because the PQ symmetry is intentionally anomalous.

broken increased to greater than that of the electroweak scale, making the axion far less interactive, the so-called *invisible* axion. The two most prominent axion models are DFSZ (Dine-Fischler-Srednicki-Zhitnitsky) [38, 39] and KSVZ (Kim, Shifman, Vainshtein, Zakharov) [40, 41]. See Refs [42, 43] for details on various axion models. The primary focus of this thesis is on axion-like particles (ALPs), and the precise nature of the model is unimportant when the focus is on ALPs rather than on the QCD axion. For reasons outside the scope of this thesis, the coupling to gluon fields (via gluon triangle diagrams) induces axion coupling to two photons, which is model independent. Furthermore, the presence of a new charge (PQ charge) carried by fermions requires the existence of a fermionic coupling. This thesis does not examine the coupling mechanisms themselves, but rather investigates the experimental manifestations they produce.

2.2 Axion detection

The axion couples to both electromagnetic fields and fermions, and these interactions are exploited experimentally to search for its existence. Axion detection experiments can be broadly classified into two broad categories: laboratory-based and astrophysical. The former aims to produce and detect axions under controlled conditions, while the latter seeks to observe axions generated by natural processes beyond Earth. For example, the CAST experiment [44] at CERN aims to detect axions produced in the interior of the Sun via energetic collisions. Generally astrophysical experiments provide stricter bounds but also have more inherent unknowns associated with them, whereas laboratory experiments are not as confining but involve fewer model dependencies.

Despite the current lack of experimental confirmation of the axion, groups around the world have put increasingly stringent bounds on its coupling and mass. Experiments such as ADMX have given the best bounds from cavity experiments geared towards axionic dark matter, and CAST has given the best bounds for helioscopes. However, we can derive bounds on the axion from astrophysics and cosmology, without resorting to an experimental procedure. For example, the interior of stars will produce an abundance of axions that would be a mechanism of energy loss for a star. The bounds can then be derived from the fact that this energy loss cannot significantly alter the predictions of solar physics [45,46]. This is also true for the axion-electron coupling. Specifically, for stars of the red giant branch, their helium burning phases could be delayed by axion cooling, leading to differences in their perceived brightness [47]. Similar arguments can be made for the cooling of white dwarfs [48].

We will give a brief description of experiments in these two categories and discuss their differing aims, mechanisms, and what they are sensitive to, in order to provide a foundation of the current experimental methods used in the field.

2.2.1 Laboratory based

As mentioned, laboratory searches seek to produce axions, usually by exactly the same means as for stimulating their decay back into detectable photons. A prominent class of experiments in this category is called light-shining-through-wall (LSW) experiments, which involve a laser beam directed across a static magnetic field, such that the polarisation of the laser is aligned with the magnetic field that in turn provides the $\mathbf{E} \cdot \mathbf{B}$ product required to source the axions. These experiments are split into two distinct sections separated via some optical barrier which acts as a shield to optical light, only allowing axions to traverse it. The second half of the experiment sees another static magnetic field applied such that a process akin to the inverse Primakoff process [49–51] can take place, where the applied field acts as a virtual photon inducing the decay of the axion back into a single photon that can be detected. The presence of the obstruction gives confidence that any detected light must be due to axion decay. The characteristics of the detected signal are related to the properties of the axion.

For conventional LSW setups it is optimal to be in the small momentum transfer limit [52] as in this regime the phase of ALPs produced at each point along the length of the magnetic field will not cancel, leading to the 'maximization' of the conversion probability. For a one-dimensional model where the laser is much smaller in the transverse direction compared with the magnetic field the probability for a photon to convert to an axion is given by:

$$P_{\varphi\to\gamma} = \frac{1}{4}\frac{\omega}{k_\varphi}\left(g_{\varphi\gamma}BL\right)^2 |F(qL)|^2, \tag{2.8}$$

where $F(qL)$ is the 'form factor' proportional to an integral over the magnetic field region with $F(0) = 1$. q is the momentum transferred to the magnetic field by the incoming photon. It can be expressed as the difference in the photon and the axion's k vectors. L is the length of the magnetic field region. For the small momentum limit to be applicable, the photon must approximately satisfy the axion dispersion relation, which puts an upper bound on the axion mass that can be probed (see equation (2.9)). Given that there will be a large difference between the axion's energy and its mass, it is clear from a power expansion to first order that $q = \frac{m_\varphi^2}{2\omega}$, where we have assumed the interaction is in vacuum. Optimisation of the form factor requires $qL \ll 1$ and limits the axion mass to [52]:

$$m_\varphi \ll 8.9 \times 10^{-4} \left[\frac{\omega}{\mathrm{eV}}\right]^{\frac{1}{2}} \left[\frac{L}{\mathrm{m}}\right]^{-\frac{1}{2}}. \tag{2.9}$$

It should be noted that gaseous materials can be added to the chamber, which allows the photon to more readily satisfy the axion's dispersion relation, in turn allowing larger masses to be probed still within the small momentum transfer limit. The maximum probability for a photon to convert to an axion is:

$$P_{\varphi\to\gamma} = \left(\frac{g_{\varphi\gamma} B L}{2}\right)^2 . \tag{2.10}$$

Experiments intended to be run for long periods utilise relativity low-power lasers that are constantly on. The continuous flux of photons compensates for the low probability of a conversion. Typical LSW experimental parameters are $B = 10$ T, $L = 10$ m, which gives the conversion probability $P \approx 10^{-17}$, assuming the upper bound $g_{\varphi\gamma} = 10^{-10}$ GeV^{-1} for the axion-photon coupling strength.

An example of an axion search of this kind can be seen at CERN with the Optical Search of QED vacuum magnetic birefringence, Axion and photon Regeneration (OSQAR) [53] collaboration. Their experiment searched for both ALPs and dilatons using 2×14.3 m long magnets of 9 T and a laser of 532 nm wavelength, which was run continuously for 1.5 hours. At the end of the experiment, analysis of the data revealed the exclusion limits for particles with masses $m < 2\times10^{-4}$ eV, finding that the strength of their electromagnetic coupling must be $g_{\varphi\gamma} < 3.5 \times 10^{-8}$ GeV^{-1} for ALPs and $g_{\Phi\gamma} < 3.2 \times 10^{-8}$ GeV^{-1} for dilatons. Beyond photon regeneration, OSQAR also investigates vacuum birefringence, a QED effect, that can be modified by axion-like particles. This approach offers model-independent sensitivity to BSM physics. Since the development of QED in the early 20th century it has been known that the vacuum can act as an optical medium for light propagating through an applied magnetic field. By measuring the relative change in the polarisation (birefringence) of a laser propagating in this background, information on the existence of ALPs can be gained. Due to the ALP coupling to electromagnetic fields, the component of the laser polarisation parallel to the magnetic field will be affected by the axionic coupling, whereas the component perpendicular will not be affected (opposite for a dilaton). Pure QED calculations give a very precise value to the change in polarisation and do not include the existence of BSM particles, therefore a measurable difference in the polarization change between QED theory and experiments could be due to the presence of BSM particles. Vacuum birefringence experiments have the advantage that there are no model dependencies[4] to consider, therefore leading to more confidence in the results. Furthermore, unlike the LSW experiments, their results scale with $g_{\varphi\gamma}^2$ and not $g_{\varphi\gamma}^4$. However, this is more than offset by the magnitude of the effects one is trying to measure.

2.2.2 Astrophysical

The CERN Axion Solar Telescope (CAST) is an astrophysical axion search, which uses a detection mechanism similar to that used in the LSW experiments. In this experiment the source of axions is the interior of the Sun. They are produced by collisions of photons under the influence of E-M fields from surrounding charged particles (Primakoff effect). The CAST group found [54] that the solar axion flux at the Earth's surface was

$$N_\varphi = g_{10}^2 3.75 \times 10^{11} \text{ cm}^{-2}\text{s}^{-2}, \tag{2.11}$$

where $g_{10} = g_{\varphi\gamma}/\left(10^{-10} \text{ GeV}^{-1}\right)$. Their experimental parameters ($L = 9.26$ m, $B = 9$ T) set bounds on the coupling and mass: $g_{\varphi\gamma} < 8.8 \times 10^{-11}$ GeV^{-1} for $m_\varphi \leq 0.02$ eV.

The Axion Dark Matter eXperiment (ADMX) is designed to search for axions that are suitable candidates as DM particles. If axions exist they would have been produced in the early universe (via vacuum misalignment) and the enormous quantities could potentially make up all of the cold dark matter (CDM)[5] mass

[4] This is more relevant to astrophysical experiments, where various gravitational, cosmological and solar dynamics can have a large influence on the outcomes of an experiment.

[5] Cold dark matter refers to non-relativistic dark matter. This type of DM would have

observed [22, 43]. This indicates that they are long lived and calculations show that their natural characteristic decay time $\tau_{decay} > \tau_{universe}$ is larger than the age of the universe. In general, weakly interacting massive particles (WIMPs) are excellent dark-matter candidates with axions also being candidates. See [23,43,55] for reviews of axionic CDM. The experiment utilises a microwave cavity that is tuned to the axion energy (decayed photon's frequency). Due to the presence of an applied magnetic field an axion should have a probability to decay into a photon, which in turn, due to resonance with the cavity, will result in a power increase that can be measured. For the photon frequency to be resonant with the cavity, ADMX primarily focuses on axions in the mass range of $2.66 - 3.33$ μeV. The probed axion parameters overlap that of the QCD axion, making any results of the ADMX experiment anticipated by a wide range of scientists. ADMX holds the record for being the most sensitive probe of the axion with the expected coherent power spikes from successfully tuned decays being of the order of 10^{-24} W. Reviews of the ADMX experiment and their results can be found in Refs. [22, 23, 56, 57]

Other notable ALP searches include: MADMAX [20], a dark-matter dielectric haloscope experiment, and CASper, another haloscope experiment, this time aimed at detecting the nuclear magnetic resonance of the coupling to gluons and nucleons [58]. Lastly, we mention PVLAS [59], which aims to detect BSM particles via vacuum birefringence and famously measured a false positive reading in 2006 [60]. For a comprehensive review on axions and axion experiments see Refs. [18, 61]. We also briefly mention that interest in axions spans both ends of the mass spectrum. Ultra-light axions (ULAs) are considered promising dark matter candidates, particularly fuzzy dark matter due to their long de Broglie wavelengths which help resolve small-scale structure issues such as the cusp-core problem [62]. At the opposite end, heavier axions with masses exceeding 100 eV have gained renewed attention. In particular, Beyer *et al.* [63] demonstrated that

---

clumped together, forming structures in the early universe.

cosmological constraints on domain wall decay and post-inflationary PQ symmetry breaking may favour heavier axions. These models challenge the assumption that viable axions must lie in the sub-eV regime and motivate new experimental approaches.

Chapter 3

Notation Conventions and Key Equations

3.1 Notation conventions

This section defines symbols, metric signature, and index conventions used throughout the thesis to avoid ambiguity when comparing with the laser–plasma and particle-physics literature.

In this work, we denote the axion field by φ rather than the customary a because a is reserved for the normalised vector potential in laser–plasma notation, $\vec{a} = (e/m_e)\vec{A}$ where $\vec{A}$ is the 3 vector potential−a symbol that will be used throughout this thesis.

Additionally, in this work we will use the 'mostly minus' metric $\eta_{\mu\nu} = \mathrm{diag}\,(1, -1, -1, -1)$ and define the four-dimensional totally antisymmetric Levi-Civita tensor as $\epsilon_{0123} = 1$ ($\epsilon^{0123} = -1$). The electromagnetic tensor is then

$$F_{\mu\nu} = \begin{pmatrix} 0 & E_x & E_y & E_z \\ -E_x & 0 & -B_z & B_y \\ -E_y & B_z & 0 & -B_x \\ -E_z & -B_y & B_x & 0 \end{pmatrix}, \tag{3.1}$$

where $F_{01} = E_1$, $F_{12} = -B_3$ etc. We work in natural units $c = \hbar = 1$ throughout this thesis, but will explicitly include factors of c and $\hbar$ when it aids clarity.

The indices of the tensor can be raised by applying the metric twice,

$$F^{\mu\nu} = \eta^{\mu\alpha} F_{\alpha\beta} \eta^{\nu\beta}, \tag{3.2}$$

giving

$$F^{\mu\nu} = \begin{pmatrix} 0 & -E_x & -E_y & -E_z \\ E_x & 0 & -B_z & B_y \\ E_y & B_z & 0 & -B_x \\ E_z & -B_y & B_x & 0 \end{pmatrix}. \tag{3.3}$$

The electromagnetic dual tensor is formed using the totally antisymmetric tensor,

$$\tilde{F}^{\mu\nu} = \frac{1}{2} \epsilon^{\mu\nu\alpha\beta} F_{\alpha\beta} \tag{3.4}$$

$$\tilde{F}_{\mu\nu} = \begin{pmatrix} 0 & -B_x & -B_y & -B_z \\ B_x & 0 & -E_z & E_y \\ B_y & E_z & 0 & -E_x \\ B_z & -E_y & E_x & 0 \end{pmatrix}. \tag{3.5}$$

Two invariants can be formed by contracting the electromagnetic tensor with itself and with its dual:

$$\tilde{F}^{\mu\nu} F_{\mu\nu} = 4\mathbf{E} \cdot \mathbf{B}, \tag{3.6}$$

$$F^{\mu\nu} F_{\mu\nu} = 2\left(\mathbf{B}^2 - \mathbf{E}^2\right). \tag{3.7}$$

3.2 Key equations

In natural units, all physical quantities are assigned a mass dimension, meaning that every dimensionful variable can be expressed as a power of mass. In this convention, quantities such as energy, momentum, mass and frequency all have mass dimension of $[E] = [p] = [m] = [\omega] = +1$, while length and time both have mass dimension of $[L] = [t] = -1$. Derivatives ∂_μ therefore carry mass dimension $+1$, the integration measure d^4x has mass dimension $[\chi] = -4$, and any quantity with dimension n corresponds to a physical unit of mass^n. This unifies the dimensional structure of the theory and allows all fields and couplings to be assigned consistent mass dimensions within the requirement $[\mathcal{L}] = 4$. This is required to ensure that the action is dimensionless $S = \int d^4x\, \mathcal{L}$

All fields and couplings introduced below must therefore be assigned dimensions consistent with this requirement.

The Axion–Maxwell Lagrangian is

$$\mathcal{L}_{\varphi,EM} = -\frac{1}{4}F^{\mu\nu}F_{\mu\nu} - A_\mu J_e^\mu + \frac{1}{2}\partial_\mu\varphi\,\partial^\mu\varphi - \frac{1}{2}m_\varphi^2\varphi^2 - \frac{g_{\varphi\gamma}}{4}\,\varphi\,\tilde{F}^{\mu\nu}F_{\mu\nu}. \tag{3.8}$$

Coupling to a fermion leads to the addition of a free Dirac term in the Lagrangian, and another interaction term[1],

$$\mathcal{L}_{\text{Dirac, EM}} = \bar{\Psi}\left(i\gamma^\mu\partial_\mu - q\gamma^\mu A_\mu - m\right)\Psi, \tag{3.9}$$

$$\mathcal{L}_{\varphi\Psi} = -ig_{\varphi\Psi}\,\varphi\,\bar{\Psi}\gamma^5\Psi, \tag{3.10}$$

where Ψ is the Dirac field and $\bar{\Psi} = \Psi^\dagger\gamma^0$, with γ^0 the time component of the gamma matrices in the Dirac representation (see Appendix D.1).

3.2.1 The equations of motion

Applying the Euler–Lagrange equations to the axion–Maxwell Lagrangian,

$$\frac{\partial\mathcal{L}}{\partial A_\rho} - \partial_\mu\frac{\partial\mathcal{L}}{\partial(\partial_\mu A_\rho)} = 0, \tag{3.11}$$

$$\frac{\partial\mathcal{L}}{\partial\varphi} - \partial_\mu\frac{\partial\mathcal{L}}{\partial(\partial_\mu\varphi)} = 0, \tag{3.12}$$

yields

$$\partial_\mu\left(F^{\mu\rho} + g_{\varphi\gamma}\varphi\tilde{F}^{\mu\rho}\right) = J^\rho, \tag{3.13}$$

$$\left(\partial_\mu\partial^\mu + m_\varphi^2\right)\varphi = -\frac{g_{\varphi\gamma}}{4}\tilde{F}^{\mu\rho}F_{\mu\rho}. \tag{3.14}$$

[1]For the dilaton, the interaction term lacks the imaginary unit i and the γ^5 matrix.

In 3-vector notation,

$$\nabla \times (\mathbf{B} + g_{\varphi\gamma}\varphi\mathbf{E}) = \partial_t (\mathbf{E} - g_{\varphi\gamma}\varphi\mathbf{B}) + \mathbf{J}, \tag{3.15}$$

$$\nabla \cdot (\mathbf{E} - g_{\varphi\gamma}\varphi\mathbf{B}) = \rho, \tag{3.16}$$

$$\left(\Box + m_\varphi^2\right) \varphi = -g_{\varphi\gamma}\, \mathbf{E} \cdot \mathbf{B}, \tag{3.17}$$

where $\Box = \partial_t^2 - \nabla^2$ is the d'Alembertian. Including the fermionic coupling modifies the Klein–Gordon equation to

$$\left(\Box + m_\varphi^2\right) \varphi = -g_{\varphi\gamma}\, \mathbf{E} \cdot \mathbf{B} - i g_{\varphi\Psi}\, \bar{\Psi}\gamma^5\Psi. \tag{3.18}$$

For a scalar dilaton field Φ with analogous couplings, the equations of motion become

$$\nabla \times [\mathbf{B}(1 + g_{\Phi\gamma}\Phi)] = \partial_t[\mathbf{E}(1 + g_{\Phi\gamma}\Phi)] + \mathbf{J}, \tag{3.19}$$

$$\nabla \cdot [\mathbf{E}(1 + g_{\Phi\gamma}\Phi)] = \rho, \tag{3.20}$$

$$\left(\Box + m_\Phi^2\right) \Phi = \frac{g_{\Phi\gamma}}{2} \left(\mathbf{E}^2 - \mathbf{B}^2\right) - g_{\Phi\Psi}\, \bar{\Psi}\Psi. \tag{3.21}$$

The interaction term used here is

$$\mathcal{L}_{\text{interacting}} = \frac{g_{\Phi\gamma}}{4} \Phi F^{\mu\nu} F_{\mu\nu},$$

though some conventions absorb the factor of $1/2$ into the definition of g.

The following table is provided to give a quick review of the dimensions of of the terms in the equations and can be used to confirm the dimensions of the axion/dilaton couplings

Summary.

Quantity	Mass dimension
A_μ	1
$F^{\mu\nu}$	2
φ	1
Φ	1
Ψ	$\frac{3}{2}$
$g_{\varphi\gamma},\ g_{\Phi\gamma}$	-1
$g_{\varphi\Psi},\ g_{\Phi\Psi}$	0

3.3 Table of symbols

The following table collects the principal symbols used throughout this thesis. Each entry includes a brief description, the units/dimension in which the quantity is expressed, and the equation in which it first appears. This is intended as a reference point for the reader and complements the notation conventions introduced earlier.

Table 3.1: Table of Symbols

Symbol	**Name / Meaning**	**Units**	**First Defined**
$g_{\varphi\gamma}, g_{\Phi\gamma}$	Axion/Dilaton electromagnetic coupling	eV	Eq. (1.3),(1.4)
m_φ, m_Φ	Axion/Dilaton mass	eV	Eq. (1.6),(1.7)
A	Background laser field amplitude	Vsm^{-1}	Eq. (4.18)
a	Probe laser field amplitude	Vsm^{-1}	Eq. (4.19)
φ	Axion field	J	Eq. (4.20)
ω_A, ω_a	Background and probe frequencies	eV	Eq. (4.18)
k_A, k_a	Background and probe wavenumbers	eV	Eq. (4.18)
$k_\varphi, \omega_\varphi$	Axion wavenumber, frequency	eV	Eq. (4.20)
ω	Slow envelope frequency	eV	Eq. (4.28)
α^2	Effective coupling parameter	eV^2	Eq. (4.31)
R	Frequency ratio ω_a/ω_A	–	Eq. (4.46)
$\Theta_\pm$	Phases of propagation eigenstates	–	Eq. (4.32)
$\delta\Theta$	Phase difference $\Theta_+ - \Theta_-$	–	Eq. (4.51)
L	Oscillation length	m	Eq. (4.52)
N_φ, N_Φ	Axion/Dilaton number flux	m^{-2}s^{-1}	Eq. (4.50)
ξ	Electrostatic plasma potential (wave frame)	–	Eq. (5.1)

Symbol	**Name / Meaning**	**Units**	**First Defined**
ω_p	Plasma frequency	rads^{-1}	Eq. (5.1)
γ	Lorentz factor of plasma wave	–	Eq. (5.1)
λ	Plasma wavelength	m	Eq. (5.7)
s	Dimensionless spectral parameter	–	Eq. (5.34)
ξ_n	Fourier coefficients of plasma potential	–	Eq. (5.9)
φ_n, Φ_n	Axion/Dilaton Fourier mode	eV	Eq. (5.12)
$\kappa_\varphi, \kappa_\Phi$	Plasma axion/dilaton Energy flux prefactor	Wm^{-2}	Eq. (5.21)
n	Mode index (Fourier mode)	–	Eq. (5.7)
$H(s), H_N(s)$	Infinite mode sum and finite mode sum	–	Eg. 5.25
$h(s), h_N(s)$	continuous modal and finite modal contribution	–	Eg. 5.27
ψ, Ψ	Dirac field	$[\text{L}]^{-3/2}$	Eq. (6.1)
$U_{n\pm}$	Landau spinor states	$[\text{L}]^{-3/2}$	Eq. (6.20)
$\Theta_n(\bar{x})$	Hermite–Gaussian transverse mode	–	Eq. (6.12)
$\bar{x}$	Transverse coordinate in magnetic field	m	Eq. (6.9)
n	Landau level index	–	Eq. (6.14)
ω_n	Landau level energy	eV	Eq. (6.14)
$g_{\varphi\Psi}, g_{\Phi\Psi}$	Axion/Dilaton–fermionic coupling	–	Eq. (6.24)
$\bar{\psi}\gamma^5\psi$	Pseudoscalar source term	$[\text{L}]^{-3}$	Eq. (6.59)
$\bar{\psi}\psi$	Pseudoscalar source term	$[\text{L}]^{-3}$	Eq. (6.61)
$\bar{\omega}$	Effective transverse decay constant	–	Eq. (6.35)

Symbol	**Name / Meaning**	**Units**	**First Defined**
$\varphi_p(\bar{x}), \Phi_p(\bar{x})$	Transverse axion/dilaton mode of order p	–	Eq. (6.48)

Chapter 4

Axion-Photon Oscillations in a Background Laser Field

4.1 Background on axion photon oscillations

We begin our discussion of axions by considering their interaction with laser beams — a promising experimental pathway to unmask the elusive axion. Advances in high-power laser technology have driven many scientific breakthroughs over recent decades, and numerous facilities around the world are now operational or under development. These laboratories offer ideal conditions for exploiting the axion's two-photon coupling, which lies at the heart of many detection experiments.

When a photon propagates through a region with a constant magnetic background — particularly when its polarisation has a component parallel to the field — the axion–electromagnetic coupling modifies Maxwell's equations by introducing additional source terms. These terms couple the photon and axion fields, preventing them from propagating independently. Instead, the system evolves according to a set of coupled wave equations, and the physical propagation eigenstates become linear combinations of the original axion and photon fields.

Following the language of neutrino oscillations, we name the original axion and photon fields ‘flavour states’ and the combinations that describe independent propagation, ‘propagation eigenstates’. This coupling allows a photon entering a magnetised region to oscillate into an axion and vice versa, directly analogous to neutrino flavour oscillations.

Axion–photon oscillations in static magnetic fields have been extensively studied, with foundational work by Raffelt and Stodolsky [64]. In such setups, a photon whose polarisation aligns with the magnetic field mixes coherently with the axion via the axion–electromagnetic coupling. The resulting propagation eigenstates are linear mixtures of the original flavour states, and the beam oscillates between photon and axion components as it travels. Importantly, the total number or energy flux of the two-field system is conserved, while the partitioning between flavour components oscillates with propagation distance. This behaviour is analogous to light traversing a birefringent medium, where total intensity remains constant, but the polarisation state rotates periodically.

Axion–photon oscillations may also play a role on wider astrophysical and cosmological scales. Supernovae and their apparent brightness are used to measure extremely long distances in the universe; however, if light from them traverses intergalactic magnetic fields, photon–axion conversion can cause a dimming of the light. This effect, if unaccounted for, could introduce a bias into luminosity distance measurements and distort inferences about cosmic expansion [65]. For low axion mass, it could potentially conflict with measurements of the universe’s acceleration [66]. Additionally, ultra-high-energy cosmic rays may be connected to oscillations of this kind. The existence of cosmic rays with energies above the Greisen–Zatsepin–Kuzmin (GZK) cut-off [67, 68] has been observed. Axion–photon oscillations have been proposed [69] as an explanation for why these photons have not lost energy by interactions with the cosmic microwave background, since axions do not interact with the CMB in the same way as photons.

This phenomenon is not only of astrophysical interest but is the same mechanism described in Section 2.2.1 when discussing light shining through a wall (LSW) experiments.

4.2 Axion-Photon oscillations in a static magnetic field

To give more concrete detail on these oscillations we consider the simple case of axion-photon oscillations in a constant background magnetic field. This will provide a useful comparison when the static background field is replaced by an oscillating laser field.

The axion-Maxwell and axion-Klein-Gordon equations can be written as follows:

$$\nabla \times (\mathbf{B} + g_{\varphi\gamma}\varphi\mathbf{E}) = \partial_t (\mathbf{E} - g_{\varphi\gamma}\varphi\mathbf{B}) \tag{4.1}$$

$$\left(\Box + m_\varphi^2\right)\varphi = - g_{\varphi\gamma}\mathbf{E}\cdot\mathbf{B}. \tag{4.2}$$

Assuming that the background magnetic field is larger than the photon and axion fields, we can linearise the equations to yield two coupled equations that can be expressed by the matrix equation below. We assume that the fields behave as plane waves - $A, \varphi \sim e^{i(kz-\omega t)}$, where A is the component of the vector potential parallel to the magnetic field

$$\overbrace{\begin{pmatrix} \left(\omega^2 - k^2 - m_\varphi^2\right) & -g_{\varphi\gamma}B_0\omega \\ -g_{\varphi\gamma}B_0\omega & \left(\omega^2 - k^2\right) \end{pmatrix}}^{\mathrm{M}} \begin{pmatrix} \varphi \\ iA \end{pmatrix} = 0. \tag{4.3}$$

It should be clear from the above that if the magnetic field were switched off, we recover the two uncoupled axion and laser waves. The existence of the magnetic field mixes the two states, as previously mentioned. The exact procedure to get from the above matrix equation to an equation giving the axion number flux will be outlined in Section 4.5. The case of axion-photon oscillations in a magnetic field has been extensively covered in the literature and therefore we only quote our result[1]. Assuming we start with a pure laser field with no axion field, the number flux can be shown to be

$$N_{\varphi} = N_A \frac{k\Omega^2}{2\omega\left(m_{\varphi}^4 + \Omega^2\right)} \left[1 - \cos(\delta\Theta)\right], \tag{4.4}$$

where we have defined the following terms

$$N_A = \frac{\omega|A|^2}{2} \quad \text{Photon Number Flux} \tag{4.5}$$

$$\Omega^2 = 4g_{\varphi\gamma}^2 B_0^2 \omega^2 \quad \text{Modified Coupling} \tag{4.6}$$

$$\delta\Theta = \frac{z}{\sqrt{2}}\sqrt{\frac{m_{\varphi}^4 + \Omega^2}{2\omega^2 - m_{\varphi}^2}} \quad \text{Phase difference between the propagating states.} \tag{4.7}$$

If we consider a small phase difference $\delta\Theta$ ($\delta\Theta \ll 1$) we can expand the oscillating term to give a flux of

$$N_{\varphi} = N_A \frac{\omega}{k} \left(\frac{gBz}{2}\right)^2, \tag{4.8}$$

where

$$k = \sqrt{\frac{2\omega^2 - m_{\varphi}^2}{2}}. \tag{4.9}$$

This result is often depicted in terms of the probability of a photon to convert into an axion or vice versa in published work, see for example [64,70,71]. Defining the probability of conversion as the ratio of the axion number flux to the photon

[1] A detailed derivation is presented in the Appendix B, where we show that our methodology recovers the standard published result.

number flux we can show, using equation (4.8), that the probability is

$$P = \frac{\omega}{k}\left(\frac{g_{\varphi\gamma}Bz}{2}\right)^2 . \tag{4.10}$$

A more detailed derivation of the number flux (and conversion probability) is presented in Appendix B. It is different to the usual published approach where a unitary rotation matrix is used to diagonalise the axion-Maxwell equations to determine the 'mass matrix'. In that approach the probability for a photon to 'convert' to an axion is given by

$$P = \frac{\sin^2(2\theta)}{2}\left[1 - \cos(\Theta_1 - \Theta_2)\right], \tag{4.11}$$

where θ is the mixing angle, which is the argument of the 2-D rotational unitary matrix.

4.3 Axion-Photon oscillations in a background laser field

A natural generalisation is to consider a non-static background magnetic field. In this chapter we implement this by introducing a second laser field that drives mixing between axion and photon states. Specifically, we consider two laser fields that interact to produce axion–photon oscillations, calculate the resulting axion number flux and compare it with the static magnetic-field case. We then evaluate the flux across experimental parameters and contrast our results with published work. Our emphasis is on using high-intensity lasers to maximise the axion flux: electromagnetic fields achievable with high-power lasers far exceed those from conventional magnets, and the axion flux scales with the square of the driving field amplitude.

Section 4.4 examines the resonance condition and the beam geometry that maximise axion production. Section 4.6 defines the boundary conditions and derives the expression for the number flux. Section 4.9 presents numerical results across relevant parameter ranges and shows that, under favourable parameters, the produced axion flux can exceed the solar axion flux at Earth's surface. Finally, Section 4.10 repeats the calculation for a scalar particle, the dilaton.

Published work similar to this thesis chapter exists, in that a secondary laser field is used to stimulate the axion production, [72–74]. Mendonça [72] proposes that the interaction between two intense electromagnetic waves in vacuum can resonantly excite, and subsequently grow an axion field. He derives coupled equations that govern the energy transfer between pump, probe and axion modes. He predicts that sideband generation would be a clear experimental signature and estimates that Petawatt-class lasers could probe the effect. Dobrich et al., [73] theoretically showed that conversion from photons to axions and back to photons when three laser beams interact, is possible. Two act as a background field (akin to the background field in this work), whilst the third laser beam acts as the probe, which are subject to axion-photon conversion and vice versa. The specific geometry and frequencies of the laser fields, enables the axion's existence to be inferred from a photon signal that has undergone a frequency shift making it distinct from initial laser fields. The distinct frequency as a result of the axion to photon conversion eliminates the requirement for axion production and for de-excitation to be separated by a 'wall'. The work of Beyer et al., [74] investigated a light shining through set up similar to ours in which two lasers are used to generate the axions. They additionally incorporate a third laser which is used to stimulate the axion reconversion back into a detectable photon signal. Furthermore, the work considered axion mass closer to the optical range, $m_\varphi \approx 1$ eV, with the possibility of using a free-electron laser to push that towards masses of 100 eV.

4.4 Derivation of the coupled axion and laser equations

The axion-Maxwell and axion Klein-Gordon equations can be written as follows:

$$\nabla \times (\mathbf{B} + g\hat{\varphi}\mathbf{E}) = \partial_t (\mathbf{E} - g_{\varphi\gamma}\hat{\varphi}\mathbf{B}) \tag{4.12}$$

$$\left(\Box + m_\varphi^2\right)\hat{\varphi} = -\, g_{\varphi\gamma}\mathbf{E}\cdot\mathbf{B}, \tag{4.13}$$

where $\mathbf{E}$ and $\mathbf{B}$ are the electric and magnetic fields, $\hat{\varphi}$ the axion field and g is the axion's coupling to electromagnetic fields. Note the use of $\hat{\varphi}$ instead of φ. We use this syntax here anticipating that we will be left with φ in our equations.

Expressing the electric and magnetic fields in terms of the vector potential $\mathbf{A}_T$, we have

$$\overbrace{\nabla\left(\nabla\cdot\mathbf{A}\right)}^{=0} - \nabla^2\mathbf{A} - g\left(\nabla\hat{\varphi}\right)\times\mathbf{A}_{,t} = -\mathbf{A}_{,tt} - g\hat{\varphi}_{,t}\nabla\times\mathbf{A} \tag{4.14}$$

$$\Box\mathbf{A}_T = g_{\varphi\gamma}\left[\left(\nabla\hat{\varphi}\right)\times\mathbf{A}_{T,t} - \hat{\varphi}_{,t}\nabla\times\mathbf{A}_T\right] \tag{4.15}$$

$$\left(\Box + m_\varphi^2\right)\hat{\varphi} = g_{\varphi\gamma}\left[\left(\mathbf{A}_{T,t}\right)\cdot\nabla\times\mathbf{A}_T\right] \tag{4.16}$$

where we have assumed there are no sources $\rho = \mathbf{J} = \mathbf{0}$ and we have used the Coulomb gauge.

In the above equations $\mathbf{F}_{,t}$ indicates the time derivative of the function $\mathbf{F}$.

We will have three fields, the background laser field $\mathbf{A}$, the probe laser field, $\mathbf{a}$ and the axion, $\hat{\varphi}$. These waves will propagate in the $\pm\mathbf{z}$ direction. We let the background wave be polarised in the $\hat{\mathbf{y}}$ direction and the probe in the $\hat{\mathbf{x}}$ direction. We express the waves in complex notation (see below), where all phases have the form $\theta_j = k_j z - \omega_j t$, where j runs over A, a, φ (background laser, probe laser and axion field). The background and probe waves must counter propagate, and we define the positive direction $\hat{\mathbf{z}}$ as the direction in which the probe wave ($\mathbf{a}$) propagates. As a result of this choice we have that $k_A < 0$, additionally the magnitude of k_φ is yet to be determined.

We express the waves using complex notation, explicitly:

$$\mathbf{A}_T = \mathbf{A} + \mathbf{a} \tag{4.17}$$

$$\mathbf{A} = \frac{1}{2}\left[Ae^{i(k_A z - \omega_A t)} + \text{C.C}\right]\hat{\mathbf{y}} \tag{4.18}$$

$$\mathbf{a} = \frac{1}{2}\left[ae^{i(k_a z - \omega_a t)} + \text{C.C}\right]\hat{\mathbf{x}} \tag{4.19}$$

$$\hat{\varphi} = \frac{1}{2}\left[\varphi e^{i(k_\varphi z - \omega_\varphi t)} + \text{C.C}\right], \tag{4.20}$$

where $\mathbf{A}_T$ is the total vector potential and C.C stands for the complex conjugate. Lastly, we point out that the amplitudes, A, a, φ are not constant. To determine their evolution we solve the axion-Maxwell's equations (4.15, 4.16) considering only terms that are in phase with each other. For the axion-photon oscillations to occur we set up the system in a way that allows the coherent flow of energy between each of the waves. This is what we mean by in phase with each other. We can use the conservation of energy to define relations between the waves frequency components, which we refer to as our resonance conditions. Letting the two light waves be described as ω_A (background) and ω_a (probe) the possible resonance conditions for the axion wave are $\omega_\varphi = \omega_a \pm \omega_A$ (likewise for the wavenumber). Only one of these is physically realisable due to the axion's finite mass. Using the free space dispersion relation ($\omega_\varphi^2 = k_\varphi^2 + m_\varphi^2$) the resonance conditions must be[2] $\omega_\varphi = \omega_A + \omega_a$, $k_\varphi = k_A + k_a$ and we conclude that the laser waves must counter propagate.

We apply the slowly varying envelope approximation (SVEA) to the coupled

[2] Using the alternative resonance condition would imply the axion to have a negative mass squared.

systems such that the left-hand sides of equations (4.15) and (4.16) result in only the first derivatives of the waves times their frequency components (we assume we are in a vacuum such that the free space dispersions are satisfied: $k_a = \omega_a$, $k_A = -\omega_A$). We can derive equations corresponding to the evolution of each of the waves by substituting equations (4.18–4.20) into equations (4.15) and (4.16). We consider the case where the resonance condition is $\omega_\varphi = \omega_A + \omega_a$ and $k_\varphi = \omega_a - \omega_A$, neglecting all non-resonant terms. This enables derivation of the following three evolution equations

$$\begin{aligned}&(k_\varphi \varphi_{,z} + \omega_\varphi \varphi_{,t})\\ =&\frac{g_{\varphi\gamma} i}{4}\left[Aa\omega_A\omega_a + i\left(\omega_a a A_{,t} - \omega_A A a_{,z}\right) + A_{,t}a_{,z}\right]\\ -&\frac{gi}{4}\left[-Aa\omega_a\omega_A - i\left(\omega_A A a_{,t} + \omega_a a A_{,z}\right) + a_{,t}A_{,z}\right]\end{aligned} \tag{4.21}$$

$$\begin{aligned}&(\omega_A A_{,t} + k_A A_{,z})\\ =&\frac{g_{\varphi\gamma} i}{4}\left[-\varphi a^* k_\varphi \omega_a + i\left(k_\varphi \varphi a^*_{,t} + \omega_a a^* \varphi_{,z}\right) + \varphi_{,z} a^*_{,t}\right]\hat{\mathbf{y}}\\ +&\frac{gi}{4}\left[\varphi a^* \omega_a \omega_\varphi + i\left(\omega_\varphi \varphi a^*_{,z} + \omega_a a^* \varphi_{,t}\right) - \varphi_{,t} a^*_{,z}\right]\hat{\mathbf{y}}\end{aligned} \tag{4.22}$$

$$\begin{aligned}&(\omega_a a_{,t} + k_a a_{,z})\\ =-&\frac{g_{\varphi\gamma} i}{4}\left[-\varphi A^* k_\varphi \omega_A + i\left(k_\varphi \varphi A^*_{,t} + \omega_A A^* \varphi_{,z}\right) + \varphi_{,z} A^*_{,t}\right]\hat{\mathbf{x}}\\ -&\frac{gi}{4}\left[-\varphi A^* \omega_A \omega_\varphi + i\left(\omega_\varphi \varphi A^*_{,z} - \omega_A A^* \varphi_{,t}\right) - \varphi_{,t} A^*_{,z}\right]\hat{\mathbf{x}},\end{aligned} \tag{4.23}$$

where we have neglected terms that are non-resonant and second derivatives on the right-hand side. See Appendix section B for a fuller derivation.

In the absence of any interaction ($g = 0$) the amplitudes of the waves are constant. As interaction between the axion and electromagnetic fields is weakly coupled we can neglect the derivatives on the right-hand side of the equations because the terms proportional to the fields dominate

$$\omega_\varphi \varphi_{,t} + k_\varphi \varphi_{,z} = \left(\frac{g_{\varphi\gamma} i \omega_A \omega_a}{2} A \right) a \tag{4.24}$$

$$\omega_a a_{,t} + \omega_a a_{,z} = \left(\frac{g_{\varphi\gamma} i \omega_A \omega_a}{2} A^* \right) \varphi \tag{4.25}$$

$$\omega_A A_{,t} + k_A A_{,z} = \left(\frac{g_{\varphi\gamma} i \omega_A \omega_a}{2} \right) \varphi a^*. \tag{4.26}$$

We make one further assumption, that the amplitude of the background field, A is much greater than that of the axion and probe laser fields, $|A| \gg |a|, |A| \gg |\varphi|$. This assumption and the weak coupling of the axion to E-M fields allow us to show that the interaction does not cause any significant variation of the background laser field. This in turn results in equations (4.24) and (4.25) becoming two coupled linear differential equations. Finally, the coupled equation can be expressed in the form of a matrix equation

$$\begin{pmatrix} \omega_\varphi \partial_t + k_\varphi \partial_z & -i g_{\varphi\gamma} \frac{\omega_A \omega_a A}{2} \\ -i g_{\varphi\gamma} \frac{\omega_A \omega_a A^*}{2} & \omega_a \left(\partial_t + \partial_z \right) \end{pmatrix} \begin{pmatrix} \varphi \\ a \end{pmatrix} = 0. \tag{4.27}$$

4.5 The propagating and flavour eigenstates

In what follows, the quantities ω and k are not the laser carrier frequencies ω_A and ω_a. They arise from the slowly varying envelope approximation (SVEA): after factoring out the fast optical oscillations $e^{i(k_j z - \omega_j t)}$ of each laser field, the remaining envelopes evolve on a much longer timescale. The parameters ω and k therefore describe the *slow modulation* of the coupled axion–photon system (the beat between the two propagation eigenstates), rather than new physical laser frequencies. This distinction becomes important when we write $\varphi, a \sim e^{i(kz-\omega t)}$ for the slowly varying fields below

$$\begin{pmatrix} kk_\varphi - \omega\omega_\varphi & -\frac{g_{\varphi\gamma}A\omega_A\omega_a}{2} \\ -\frac{g_{\varphi\gamma}A^*\omega_A\omega_a}{2} & \omega_a\left(k-\omega\right) \end{pmatrix} \begin{pmatrix} \varphi \\ a \end{pmatrix} = \begin{pmatrix} 0 \\ 0 \end{pmatrix}. \tag{4.28}$$

Only two combinations of the axion and photon field satisfy the above equation (given that we require the fields to be non zero), which we will call the propagating states. We partially adopt the language used to describe neutrino oscillations, where the fields, of unique particle type, are 'flavour' states and the solution to the matrix equation (4.28) where the fields are non zero, are propagating states. The dispersion relation of the propagating states can be derived by setting the determinant of the matrix to zero. Computing this we derive the following equation

$$k^2k_\varphi - 2k\omega\omega_a + \omega^2\omega_\varphi - \frac{g^2|A|^2\omega_A^2\omega_a}{4} = 0. \tag{4.29}$$

This equation has two solutions that give the wavenumber of each propagating state. In each case we assume the frequency (ω) to be the same

$$k_\pm = \frac{\omega\omega_a}{k_\varphi} \pm \frac{\omega_A}{k_\varphi}\sqrt{\omega^2 + \alpha^2}, \tag{4.30}$$

where we have defined the following parameter

$$\alpha^2 = \frac{g_{\varphi\gamma}^2|A|^2\omega_a k_\varphi}{4}. \tag{4.31}$$

This parameter is a measure of the mutual influence of the axion and laser fields resulting from the presence of the background field. We refer to this as the effective coupling.

We can now form a matrix equation for the propagating states by substituting (4.30) into (4.28),

$$\begin{pmatrix} \left(\omega_A\left(\sqrt{\omega^2+\alpha^2}-\omega\right)\right) & -\frac{g_{\varphi\gamma}A\omega_A\omega_a}{2} \\ -\frac{g_{\varphi\gamma}A^*\omega_A\omega_a}{2} & \frac{\omega_A\omega_a}{k_\varphi}\left(\omega-\sqrt{\omega^2+\alpha^2}\right) \end{pmatrix} \begin{pmatrix} \varphi \\ a \end{pmatrix} = \begin{pmatrix} P_+ \\ P_- \end{pmatrix}, \tag{4.32}$$

where P_+ and P_- are the two branches of the propagating states, each propagating with phase $\Phi_\pm = k_\pm z - \omega t$, respectively.

The matrix can be inverted and expressed in equation form to illustrate how the flavour states can be expressed as a superposition of propagating states

$$\varphi = \frac{\left(\sqrt{\omega^2+\alpha^2}-\omega\right)}{\omega_A\left[\alpha^2+\left(\omega-\sqrt{\omega^2+\alpha^2}\right)^2\right]}P_+ - \frac{g_{\varphi\gamma}Ak_\varphi}{2\omega_A\left[\alpha^2+\left(\omega-\sqrt{\omega^2+\alpha^2}\right)^2\right]}P_- \tag{4.33}$$

$$a = \frac{k_\varphi\left(\omega-\sqrt{\omega^2+\alpha^2}\right)}{\omega_A\omega_a\left[\alpha^2+\left(\omega-\sqrt{\omega^2+\alpha^2}\right)^2\right]}P_- - \frac{g_{\varphi\gamma}A^*k_\varphi}{2\omega_A\left[\alpha^2+\left(\omega-\sqrt{\omega^2+\alpha^2}\right)^2\right]}P_+. \tag{4.34}$$

Expressing the equations in this way emphasises the flavour state oscillation. The phase difference between the propagating states, as in the neutrino case, means that a well defined flavour state evolves and the probability of measuring the other flavour state changes. Starting with a pure photon there is a probability to measure an axion and vice versa.

4.6 Boundary conditions and the axion number flux

We consider two sets of boundary conditions to analyse the evolution equations 4.33,4.34 which describe each the flavour states in terms of the propagating states. They describe the case where initially, at coordinate $z = 0$, either the probe wave,

a, or the axion wave, φ is present. Away from this initial coordinate, the waves couple and at subsequent coordinates there is a finite chance that the other wave will be present on measurement. We determine the flux of the wave for each case and show how it depends on the axion mass. The boundary conditions enable calculation of the probability of producing axions in the laboratory via laser interactions. They also allow calculation of the probability of detecting axions from a known source, such as the Sun, using a laser interaction[3].

4.6.1 Axion production by interaction of two laser beams

Applying the following boundary conditions to equation (4.32),

$$\hat{\varphi}(0,t) = 0 \tag{4.35}$$

$$\mathbf{a}(0,t) = a\hat{\mathbf{x}}, \tag{4.36}$$

allows expression of the propagating states in terms of the probe wave

$$P_+ = -\left(\frac{g_{\varphi\gamma} A\omega_A\omega_a}{2}\right) a \tag{4.37}$$

$$P_- = \left(\frac{\left(\omega - \sqrt{\omega^2+\alpha^2}\right)\omega_A\omega_a}{k_\varphi}\right) a. \tag{4.38}$$

We can therefore show that the axion field at a general position is proportional to the probe wave amplitude multiplied by an oscillatory term derived from the phase differences between the propagating states

[3] By "known" we mean that, if axions exist, the source would be identifiable, although no axion source has yet been experimentally verified.

$$\varphi = \frac{gA\omega_a}{2} \frac{\left(\omega - \sqrt{\omega^2 + \alpha^2}\right)}{\left[\alpha^2 + \left(\omega - \sqrt{\omega^2 + \alpha^2}\right)^2\right]} e^{i\Theta_+} \left(1 - e^{-i\delta\Theta}\right) a. \tag{4.39}$$

The physical axion field is then the real part of this expression

$$\mathcal{R}[\varphi] = \frac{g_{\varphi\gamma}A\omega_a}{2} \frac{\left(\omega - \sqrt{\omega^2 + \alpha^2}\right)}{\left[\alpha^2 + \left(\omega - \sqrt{\omega^2 + \alpha^2}\right)^2\right]} \left[\cos(\Theta_+)\left(1 - \cos(\delta\Theta)\right) - \sin(\Theta_+)\sin(\delta\Theta)\right] a, \tag{4.40}$$

where $\delta\Theta = \Theta_+ - \Theta_-$ and where $\mathcal{R}[F]$ represents the real part of F.

The energy flux of the axion wave can be shown to be (**??**)

$$S_\varphi = -\partial_t \varphi \nabla \varphi *, \tag{4.41}$$

which can be expressed as the following

$$S_\varphi = \omega_\varphi k_\varphi < |\mathcal{R}\varphi|^2 > \tag{4.42}$$

$$= |a|^2 \frac{\alpha^2 \omega_\varphi \omega_a}{4\left(\omega^2 + \alpha^2\right)} \left[1 - \cos(\delta\Theta)\right], \tag{4.43}$$

where

$$\delta\Theta = 2z \frac{\omega_A}{k_\varphi} \sqrt{\omega^2 + \alpha^2}, \tag{4.44}$$

and where $< \cdot >$ denotes the time average of the oscillation. Studying the oscillating term reveals that, for small $\delta\Theta$, the field deviates very little from its starting point.

We define the number flux as the energy flux over the energy per axion.

$$N_\varphi = \frac{S_\varphi}{\omega_\varphi}. \tag{4.45}$$

It is useful to define a variable equal to the ratio of the frequencies of the laser fields. We show the relationship between the axion mass and this ratio, derived from the resonance conditions.

$$R = \frac{\omega_a}{\omega_A} \tag{4.46}$$

$$R = \frac{m_\varphi^2}{4\omega_A^2}. \tag{4.47}$$

The number flux, expressed in terms of the intensity of the laser fields

$$|a|^2 = \frac{2I_a}{\omega_a^2} \tag{4.48}$$

$$|A|^2 = \frac{2I_A}{\omega_A^2}, \tag{4.49}$$

and in terms of R (where appropriate) has the following form

$$N_\varphi = g_{\varphi\gamma}^2 c^2 I_A I_a \frac{(R-1)}{4\omega_A\left(\omega^2+\alpha^2\right)}\left[1-\cos(\delta\Theta)\right]. \tag{4.50}$$

As expected, the axion flux is proportional to the intensity of the two laser fields. More interesting is the inverse relationship to the square of the frequency ω. The term ω is the slow envelope frequency of the oscillations. It is a measure of the degree by which the probe laser frequency is modulated when propagating in the presence of the background laser field. Realistically, due to the weak coupling of the axion any probe laser propagating in a background laser field will experience very little change. In Figure 4.1 we illustrate the variation in number flux with this frequency. In the plots shown in this chapter we assume an axion electromagnetic coupling of $g_{\varphi\gamma} = 1 \times 10^{-10}$ GeV^{-1}, and, unless otherwise stated, the intensities of the laser fields are taken to be $I_A = 10^{22}$ Wm^{-2} and $I_a = 10^{20}$ Wm^{-2}. Lastly, the length of the interaction is assumed to be 100 times the wavelength of the background laser.

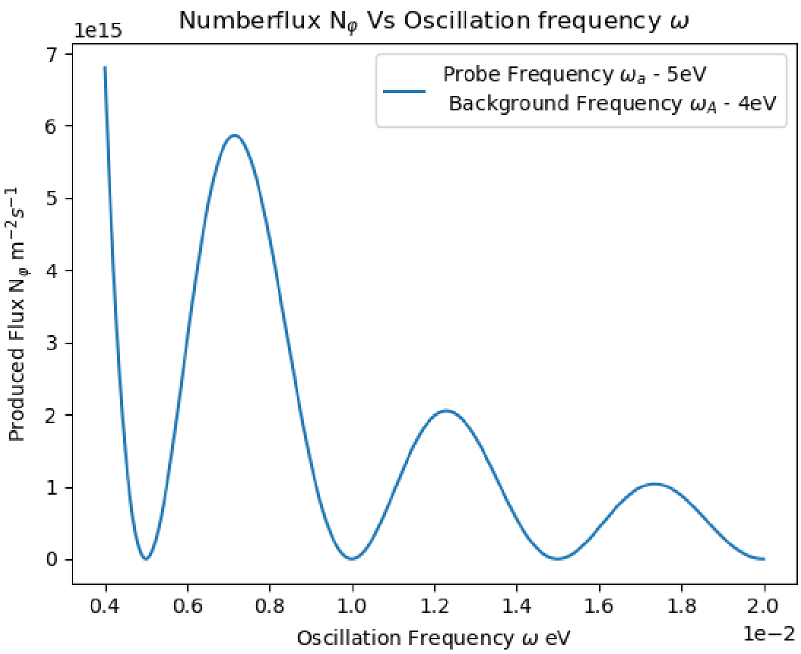

Figure 4.1: The axion flux vs oscillation frequency. The oscillation frequency varies from 0.1% to 0.5% of the background laser's frequency.

Although we illustrate the full oscillatory structure for clarity, it is important to note that for any realistic choice of parameters, the phase difference $\delta\Theta$ remains much smaller than unity. In practice, the system never reaches the first oscillation peak, and the flux is always in the small-angle regime.

The figure shows that the flux decreases with frequency as expected from the denominator in equation (4.50). However, due to the presence of this frequency term in the phase difference, this decrease is not universal. As the frequency (ω) increases, the oscillating term takes over and the flux peaks when $\delta\Theta = \pi$ before the oscillation repeats. Each additional oscillation peak diminishes due to the presence of the frequency in the denominator in the equation for the flux. We explore this oscillation more closely in the next section, examining $\delta\Theta$ and the contribution to the overall flux for various parameter ranges.

4.7 Analysis of the axion number flux

The phase difference between the two propagating states results in an oscillation of the flux. We take a closer look at that oscillation's dependencies. Specifically, the phase difference is

$$\delta\Theta = 2z\frac{\sqrt{\omega^2+\alpha^2}}{(R-1)}, \tag{4.51}$$

where we have assumed the same frequency for the propagating states. This phase difference is the ratio of the distance propagated to the wavelength of the oscillation, where the length of the oscillation is defined as

$$L = \frac{(R-1)}{2\sqrt{\omega^2+\alpha^2}}. \tag{4.52}$$

The part of the flux responsible for the oscillation ($[1-\cos(\delta\Theta)]$) increases slowly for small $\delta\Theta$, which critically affects the flux. For small $\delta\Theta$, less than a radian, we can expand the oscillating term.

$$[1-\cos(\delta\Theta)] \approx \frac{\delta\Theta^2}{2}. \tag{4.53}$$

If the expression (4.53) is valid - $\delta\Theta \ll 1$ - the result is to significantly reduce the flux from its peak value. In this case, the expression for the flux is the following

$$N_\varphi = g_{\varphi\gamma}^2 I_A I_a \frac{z^2}{2\omega_A(R-1)}, \tag{4.54}$$

where z is the propagation distance.

An interesting comparison can be made with the case of a static magnetic field background in this limit. In the static case, the probability of conversion is given by equation (2.10). If we define the flux in our case as $N_\varphi = P_{a\to\varphi}N_a$ we have

$$P = \left(\frac{g_{\varphi\gamma}|A|\omega_A z}{2}\right)^2 \frac{\omega_a}{k_\varphi} \tag{4.55}$$

$$P = \frac{g_{\varphi\gamma}^2 I_A z^2}{2}\frac{\omega_a}{k_\varphi}, \tag{4.56}$$

which has a very similar form to Equation 2.10, the idealised conversion probability from the small momentum transfer limit. Note that this limit, the static magnetic field case, requires $m_\varphi \ll \omega$ (see Section 2.2.1). In this work the axion mass probed comes from the resonance conditions. This illustrates the difference in the regimes explored in these works. Here, we are able to probe for larger axion masses without suffering a loss of coherence (coherence is a measure of the phase mismatch between flavour states). In each case, static field and background laser field, the probabilities have different origins. Finally, comparing the derived probability (2.10, 4.56) we see that, with all else equal, a significant magnetic field strength is required to compare with the laser intensities realisable today. A magnetic field of $B_0 \approx 6.5 \times 10^3$ T would be comparable to a laser intensity of $I = 1 \times 10^{22}$ Wm^{-2}.

We will analyse the flux and its oscillating component in two more regimes, $\alpha^2 \gg \omega^2$ and $\omega^2 \gg \alpha^2$. If we consider $\delta\Theta$ for $\alpha^2 \gg \omega^2$ and express the result using equation (4.31), we have

$$\delta\Theta = z g_{\varphi\gamma}\sqrt{2I_A}\sqrt{\frac{R}{(R-1)}}, \tag{4.57}$$

which for $R \gg 1$ only depends on the background laser intensity. In deriving equation (4.57) we have used equations (4.31), (4.46) and (4.49). In such a situation, equation (4.53) will be valid, because the alternative would require a very high intensity background laser, which remains constant over a considerable distance. In this situation the flux is

$$N_\varphi = g_{\varphi\gamma}^2 I_A I_a \frac{z^2}{2\omega_a}, \tag{4.58}$$

where $\delta\Theta \ll 1$. In the other regime, $\omega^2 \gg \alpha^2$, the flux is identical for $\delta\Theta \ll 1$. We can see this to be the case when we first derived equation (4.50) from the 'symmetry' between the amplitude of the flux and the oscillating angle $\delta\Theta$. This is the same structure as the probability of an axion converting to a photon (or vice versa) for the case of the background static magnetic field - see equation (4.4). Moreover, this is the same expression as (4.54) but for $R \gg 1$. Realistically, equation (4.51) will be small so the oscillating term can be expanded and the flux expressed as (4.54). In this regime, knowing the exact magnitude of the slow frequency ω is unimportant because the flux is expressed in quantities that we can control.

4.7.1 The flux dependency on axion mass

In our calculation of the flux - equation (4.50), the explicit dependence on the axion mass is obscured. It is intrinsically linked to the resonant conditions and is thus implied when the laser frequency or effective coupling is shown. In Figures 4.2 and 4.3 we plot the variation of the axion flux as a function of axion mass, indicating the resultant change in the ratio of the laser frequencies on a third axis - note the background laser frequency is held fixed in each case.

In Figure 4.2 we observe that the oscillations (in parameter space of the axion mass) increase in both 'wavelength' and amplitude. From equation (4.52) it is clear that an increase in axion mass increases the wavelength of the (physical) oscillation. Additionally, from the numerator of equation (4.50), we see that it also increases the amplitude. However, further increase of the axion mass reduces $\delta\Theta$ until equation (4.53) becomes applicable, eventually leading to a point

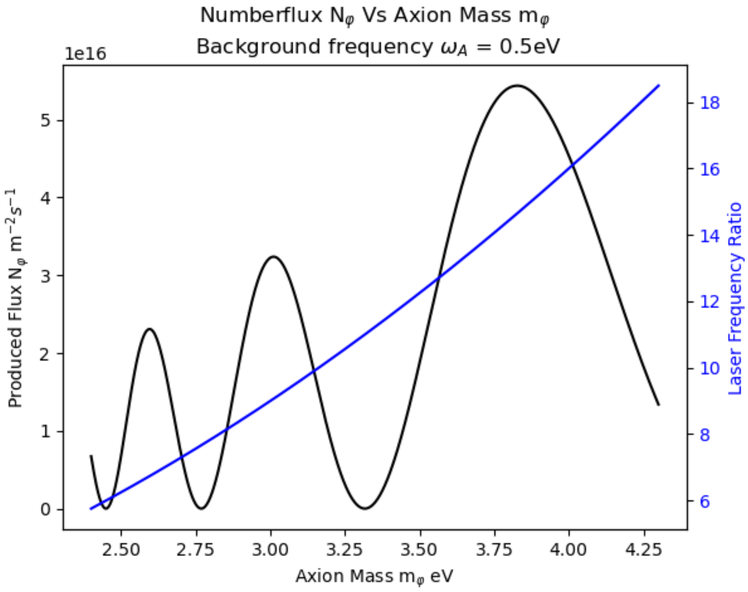

Figure 4.2: The flux increases and oscillates due to the increase in axion mass. The slow oscillation frequency is $\omega = 0.1\omega_A$.

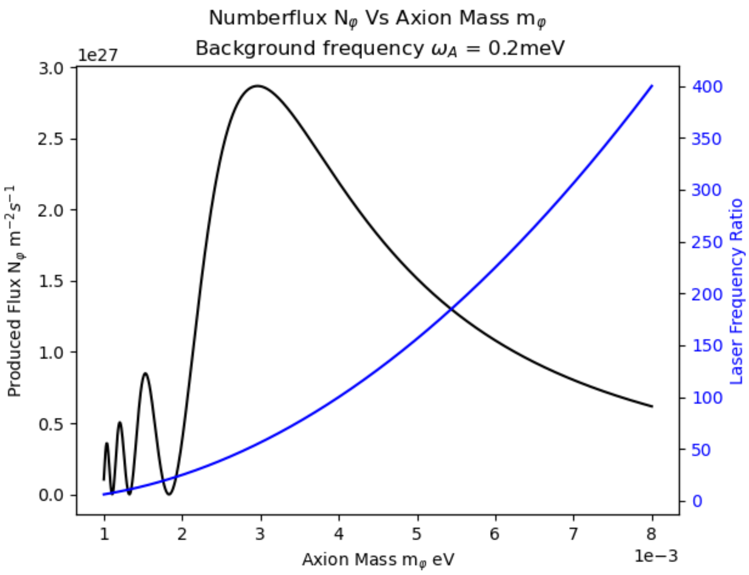

Figure 4.3: The flux initially increases over consecutive oscillations due to the increased axion mass before tending to zero. The slow oscillation frequency is $\omega = 0.5\omega_A$.

where the increase in amplitude no longer outpaces the reduction from the small value of $\delta\Theta$. Equation (4.54) illustrates this point, and as can be seen, the axion number flux has the following dependence[4], $N_\varphi \propto m_\varphi^{-2}$. This is shown in Figure 4.3, where it can be seen that the flux tends to zero for sufficiently large mass. It should be noted that as we vary the laser frequencies or axion mass, the corresponding laser intensities and/or fluxes are held fixed. This is reasonable as long as each of these variables are not changed too drastically. Additionally, they should not be varied to the point that the resonance conditions no longer hold. This is discussed more in section (4.9.1).

The last dependency we highlight is that of the propagation distance - denoted by z in our equations. This only factors into the flux through the term $\delta\Theta$, which it is directly proportional to. However, it plays a more crucial role in the assumptions that have gone into deriving the number flux. The length of the interaction is necessarily dictated by the length over which the background laser field can be held constant. This is likely the primary constraint inhibiting the axion flux reaching its peak value. In Figure 4.4 we plot the flux as a function of interaction length, over lengths up to one hundred times the wavelength of the background field. There is an approximate factor of two between the peak of each of the curves, highlighting the sensitivity of the flux to change in the axion mass. This corresponds to a doubling of the probe frequency ($R = 5$ in the blue curve while $R = 10$ in the black curve). Furthermore, careful consideration needs to be given to the propagation distance; the peak of the black curve nearly overlaps the minimum of the blue curve, emphasising the importance of where a measurement is made.

[4]We take $R \gg 1$ here so that $(R-1) \approx R$.

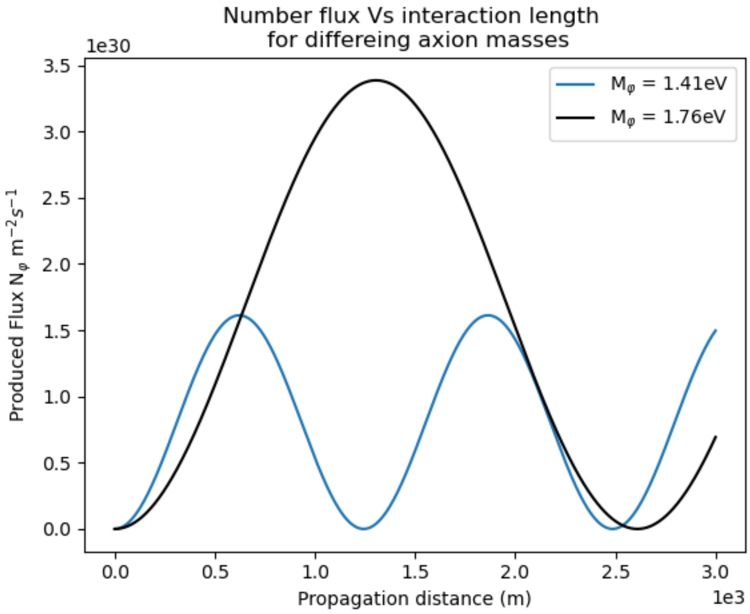

Figure 4.4: The axion flux as a function of the interaction length. The background laser frequency is $\omega_A = 0.5$ eV and the slow oscillation frequency has been set to $\omega = 1n$eV.

4.8 Axion-Photon oscillations starting with an axion

In this section we consider an axion wave propagating into the background laser field region. Here we reverse the boundary conditions (shown below) such that initially we have an axion source and our background laser field. One would then detect the newly produced photons, which we had previously referred to as the probe wave with a frequency determined by the resonance conditions. The procedure to arrive at a measurable quantity - the photon number flux/intensity, is similar to the steps followed in the previous section, and therefore we show only the key equations here. Additionally, a significant amount of the analysis in the previous section also applies here and therefore we omit this. In this case, the boundary conditions are

$$\hat{\varphi}(0,t) = \varphi \tag{4.59}$$

$$\mathbf{a}(0,t) = 0. \tag{4.60}$$

Applying these boundary conditions to equations (4.33) and (4.34) we express our propagating states in terms of the axion field

$$P_{+} = \omega_A \left(\sqrt{\omega^2+\alpha^2} - \omega\right)\varphi \tag{4.61}$$

$$P_{-} = \frac{g_{\varphi\gamma} A^{*} \omega_A \omega_a}{2}\varphi \tag{4.62}$$

Note the symmetry between this section and the previous in expressing our propagating states in terms of the initial wave.

We can then express the photon field in terms of our initial axion field multiplied by an oscillating term that arises from the difference in wavelengths of the propagating states.

$$a = \frac{g_{\varphi\gamma} A^{*} k_{\varphi}}{2} \frac{\left(\omega - \sqrt{\omega^2+\alpha^2}\right)}{\left[\alpha^2 + \left(\omega - \sqrt{\omega^2+\alpha^2}\right)^2\right]} \varphi e^{i\Theta_{+}} \left[1 - e^{-i\delta\Theta}\right]. \tag{4.63}$$

The intensity of this photon field can be determined as

$$I_a = \frac{\alpha^2 k_{\varphi} \omega_a}{8\left(\omega^2+\alpha^2\right)} |\varphi|^2 \left[1 - \cos(\delta\Theta)\right]. \tag{4.64}$$

Expressing the result in terms of the intensity of the background laser and flux of the axion source, where possible, and in terms of R, the laser frequency ratio $R = \frac{\omega_a}{\omega_A}$, the result for the intensity and consequently photon flux N_a ($N_a = \frac{I_a}{\omega_a}$)

of the produced light wave is as follows

$$I_a = g_{\varphi\gamma}^2 I_A N_\varphi \frac{R^2(R-1)\omega_A}{16\,(\omega^2+\alpha^2)} \left[1-\cos(\delta\Theta)\right], \tag{4.65}$$

$$N_a = g_{\varphi\gamma}^2 I_A N_\varphi \frac{R(R-1)}{16\,(\omega^2+\alpha^2)} \left[1-\cos(\delta\Theta)\right]. \tag{4.66}$$

The difference in form of the equations (4.66) and (4.50) is because the former is expressed in terms of the axion flux while the latter in terms of the probe intensity.

4.9 Numerical results

4.9.1 Suitable parameter values

Given that the boundary conditions require the presence of an axion source, one might consider existing axion-producing experiments as a guide for numerical parameters. We have discussed two such experiments in Section 2.2 - LSW experiments such as [53] and solar axion experiments such as [54]. Unfortunately, these experimental parameters make a poor choice for our axion-photon oscillations, with an optical source for a background field: The LSW experiment is optimised in the small momentum transfer limit (see equation (2.9)). As shown in [53], these experiments use optical lasers and are sensitive to particle production in the μeV range. This makes conforming to our resonance conditions difficult. When considering solar axions we see that their energy distribution is peaked at around 3 keV (with an average energy of about 4.2 keV) [54]. In this case the frequency separation between the axion source and an optical background laser would be too great to enable the resonance conditions to hold. This axion-photon oscillation process should then be viewed as another alternative approach in the search for axions.

4.9.2 Expected flux from axion-photon oscillations in a laser background

To provide an example calculation of the produced flux we consider optical and infrared lasers, $\omega_A = 1$ eV and $\omega_a = 2$ eV, and assume that the background laser amplitude is held constant for 25 wavelengths ($25\lambda_A$). We take the laser intensities to be $I_A = 1 \times 10^{22}$ Wm^{-2}, $I_a = 1 \times 10^{20}$ Wm^{-2} and the electromagnetic coupling of the axion to be $g = 2 \times 10^{-11}$ GeV^{-1}, yielding an axion flux of $N_\varphi = 4.97 \times 10^{15}$ m^{-2}s^{-1}, where we have assumed $\omega \leq 30$ μeV such that we have $\delta\theta \ll 1$. For the flux to reach its peak, assuming the same frequency ω, the background laser would need to be held constant over a length of 10.35 mm[5] ($8333\lambda_A$), resulting in a flux of $N_\varphi = 2.24 \times 10^{20}$ m^{-2}s^{-1}. Alternatively, if the frequency ω was such that at the measurement point ($z = 25\lambda_A$) the maximum flux was reached, the flux would be $N_\varphi = 2.02 \times 10^{15}$ m^{-2}s^{-1} with $\omega = 10$ meV. Each of the fluxes calculated here exceeds that of the solar axion flux at Earth's surface[6]. Although it should be noted that the solar axion flux at Earth's surface is a continuous, time-independent flux, whereas the flux calculated in this chapter corresponds to the peak axion flux generated during a laser pulse and is therefore not a time-averaged or steady-state quantity. We compare our predicted axion flux with two light shining through a wall axion searches. For comparison, the OSQAR experiment at CERN [53] and the ALPS II experiment at DESY [75]. We estimate their axion fluxes to be $N_\varphi = 3.95 \times 10^7$ m^{-2}s^{-1} and $N_\varphi = 7.35 \times 10^{13}$ m^{-2}s^{-1}, respectively for the same axion electromagnetic coupling strength[7]. These results are based on the parameters given in the respec-

[5]This is clearly not realistic for our set up and is only meant for illustration purposes.

[6]This is calculated from the results of [44].

[7]The OSQAR experiment is not sensitive to an axion of this coupling strength. The ALPS II experiment achieves a lower sensitivity and that is the coupling strength we used in the

tive papers as well as the manufacturing specifications of the Coherent Verdi V18 and Coherent Monolith Mephisto MOPA. This demonstrates that the laser–laser mechanism produces axion fluxes that are competitive with, those of existing light-shining-through-a-wall experiments, while providing a complementary approach that is sensitive to a different region of axion mass parameter space.

The boundary conditions in Sections 4.6.1 and 4.8 could be used to envision a scenario in which a background laser field is used to generate an axion flux and subsequently de-excite (oscillate) into photons. If we assume the same background field for each boundary condition and that it is constant over 25 wavelengths ($\delta\theta \ll 1$) we obtain a photon flux of $N_a = 1.98 \times 10^{-8}$ m^{-2}s^{-1}. Comparing this with the work in [53], we estimate that they would have expected a photon flux (after the 'wall') of $N_a = 6.66 \times 10^{-11}$ m^{-2}s^{-1}. The ALPS II experiment, for its predicted future operation, boasts the largest photon flux at the detector, to our knowledge. Their predicted photon rate is around $N = 4 \times 10^{-5}$ s^{-1} (3.5 per day). This is achieved in part due to the enhancement of the signal on either side of the wall by a Fabry-Perot cavity, which increases the signal by 5000 and 40000,[8] respectively. Our work aims at maximising the axion flux and not necessarily achieving the largest photon flux. We have not extended our work to explore techniques to increase the resultant photon flux.

4.10 Dilaton

As we have alluded to in the introductory sections, axions are far from the only weakly coupled particles that result from generalised extensions to the standard model. The dilaton is one such particle that we investigate. As has been discussed already in Section 1.2, the dilaton is closely related to the axion and couples to the electromagnetic scalar invariant - see Chapter 3 for more details on the dilaton calculations.

[8]With their current equipment this is closer to 16000.

equations and electromagnetic coupling.

We repeat the calculations of the preceding section for the dilaton, similarly deriving the fluxes and analysing the scaling with dilaton mass. Throughout, we will comment on and discuss the differences in the derived equations, comparing the pseudoscalar and scalar particles. We will not demonstrate numerical calculation however, as, given the approximations used in this work, there is a near equivalence between the equations for the dilaton and axion.

The dilaton-Maxwell's equations were derived in Section 3 but are shown again here, where in equations (4.69) and (4.70) we express them using the electromagnetic vector potential, $\mathbf{A}$.

$$\nabla \times \left[\mathbf{B}\left(1+g_{\Phi\gamma}\hat{\Phi}\right)\right] = \partial_{,t}\left[\mathbf{E}\left(1+g_{\Phi\gamma}\Phi\right)\right] \tag{4.67}$$

$$\left(\Box + m_{\Phi}^2\right)\hat{\Phi} = \frac{g_{\Phi\gamma}}{2}\left(\mathbf{E}^2-\mathbf{B}^2\right) \tag{4.68}$$

$$\left(1+g_{\Phi\gamma}\hat{\Phi}\right)\Box\mathbf{A}_T = -\,g_{\Phi\gamma}\left[\mathbf{A}_{T,t}\hat{\Phi}_{,t} + \left(\nabla\hat{\Phi}\right)\times\nabla\times\mathbf{A}_T\right] \tag{4.69}$$

$$\left(\Box + m_{\Phi}^2\right)\hat{\Phi} = \frac{g_{\Phi\gamma}}{2}\left[\left(-\mathbf{A}_{T,t}\right)^2-\left(\nabla\times\mathbf{A}_T\right)^2\right]. \tag{4.70}$$

A key difference between the axion and dilaton equations can be seen by the fact that the dilaton scales the results. In the grouping of differential operators, time derivates appear beside time derivates and spatial derivatives beside spatial derivatives. Additionally, in equation (4.68) it is clear that the source of the dilaton is maximised when the either the electric or the magnetic field goes to zero, whereas, for the axion, this results in a vanishing source. As this work pertains to laser-dilaton interactions we cannot set the magnetic field to zero. Furthermore, from equations (4.69) and (4.70), the polarisation of the lasers must be parallel, which contrasts with that of the axion.

As with the axion we collect only resonant terms to derive the evolution equations of each of the waves. We however assume that the background laser field, $\mathbf{A}$, is constant over the interaction length, thus we will only derive two evolution equations.

The resonance conditions are similar to that of the axion: $\omega_\Phi = \omega_A + \omega_a$, with the probe and dilaton waves travelling in the $+\mathbf{z}$ direction and the pump in the $-\mathbf{z}$ direction. The difference here is that we will assume the probe and pump waves are similarly polarised in the $\mathbf{x}$ direction.

$$\hat{\Phi} = \frac{1}{2}\left[\Phi e^{i(k_\varphi z - \omega_\varphi t)} + \text{C.C}\right] \tag{4.71}$$

$$\mathbf{A} = \frac{1}{2}\left[A e^{i(k_A z - \omega_A t)} + \text{C.C}\right]\hat{\mathbf{x}} \tag{4.72}$$

$$\mathbf{a} = \frac{1}{2}\left[a e^{i(k_a z - \omega_a t)} + \text{C.C}\right]\hat{\mathbf{x}}. \tag{4.73}$$

$$\begin{aligned}(\omega_a a_{,t} + k_a a_{,z}) = \frac{-ig_{\Phi\gamma}}{4}&\left[\omega_A\omega_\Phi A^*\Phi + i\left(\omega_A A^*\Phi_{,t} - \omega_\Phi \Phi A^*_{,t}\right) + A^*_{,t}\Phi_{,t}\right.\\ &-k_A k_\Phi \Phi A^* - i\left(k_\Phi \Phi A^*_{,z} - k_A A^*\Phi_{,z}\right) + \Phi_{,z}A^*_{,z}\\ &\left. i\Phi\left(\omega_A A^*_{,t} + k_A A^*_{,z}\right)\right]\end{aligned} \tag{4.74}$$

$$\begin{aligned}(\omega_\Phi \Phi_{,t} + k_\Phi \Phi_{,z}) = \frac{ig_{\Phi\gamma}}{8}&\left[-\omega_A\omega_A aA - i\left(\omega_a a A_{,t} + \omega_A A a_{,t}\right) + a_{,t}A_{,t}\right.\\ &\left.+k_A k_a aA + i\left(k_a a A_{,z} + k_A A a, z\right) + a_{,z}A_{,z}\right]\end{aligned} \tag{4.75}$$

There is a clear similarity in the evolution equations for dilatons and axions. One difference, however, originates from the term on the left-hand side of equation (4.69) - $(1+g_{\Phi\gamma}\Phi)\,\Box\mathbf{A}$. In the case of the probe evolution this term yields additional terms that are proportional to the change in the background field - these terms present in the last line of equation (4.74). A further point to note is that these 'extra' terms are not multiplied by an imaginary unit. While the assumption of a constant background field eliminates the additional terms in equation (4.74), their structure suggests that introducing a modulation could alter the dynamics of the dilaton–photon system in ways not mirrored by the axion case. A comparison utilising such a modulation could reveal further differences in the coupling mechanisms of scalar versus pseudoscalar particles, specifically in how they influence the evolution of the probe field.

Our evolution equations reduce to two coupled differential equations

$$\omega_a\left(a_{,t}+a_{,z}\right) = -\left(\frac{ig_{\Phi\gamma}\omega_A\omega_a A^*}{2}\right)\Phi \tag{4.76}$$

$$\omega_\Phi\Phi_{,t}+k_\Phi\Phi_{,z} = -\left(\frac{ig_{\Phi\gamma}\omega_A\omega_a A}{4}\right)a. \tag{4.77}$$

Following a similar process to that of the axion, we express these equations in matrix form, taking the solution to be of the form of a plane wave $e^{i(kz-\omega t)}$.

$$\begin{pmatrix} kk_\Phi-\omega\omega_\Phi & \frac{g_{\Phi\gamma}A\omega_A\omega_a}{4} \\ \frac{g_{\Phi\gamma}A^*\omega_A\omega_a}{2} & \omega_a\left(k-\omega\right)\end{pmatrix}\begin{pmatrix}\Phi\\ a\end{pmatrix}=\begin{pmatrix}0\\0\end{pmatrix} \tag{4.78}$$

$$k_\pm = \frac{\omega\omega_S}{k_\Phi}\pm\frac{\omega_I}{k_\Phi}\sqrt{\omega^2+\alpha^2} \tag{4.79}$$

$$\alpha^2 = \frac{g^2_{\Phi\gamma}|A_I|^2\omega_a k_\Phi}{8}. \tag{4.80}$$

Note the factor of two difference between α defined for the dilaton and that of the axion. This originates from the differences in their Klein-Gordon equations where a factor of two difference is obtained from the contraction of the electromagnetic tensor and its dual, and the contraction of the dual with itself.

The propagating states can be expressed in terms of the flavour states, and vice versa

$$P_+ = \omega_A \left(\sqrt{\omega^2+\alpha^2}-\omega\right)\Phi + \frac{g_{\Phi\gamma}A\omega_A\omega_a}{4}A_S \tag{4.81}$$

$$P_- = \frac{\omega_A\omega_a}{k_\Phi}\left(\omega-\sqrt{\omega^2+\alpha^2}\right)a + \frac{g_{\Phi\gamma}A^*\omega_A\omega_a}{2}\Phi \tag{4.82}$$

$$\Phi = \frac{\left(\sqrt{\omega^2+\alpha^2}-\omega\right)}{\omega_A\left[\alpha^2+\left(\sqrt{\omega^2+\alpha^2}-\omega\right)^2\right]}P_+ + \frac{g_{\Phi\gamma}Ak_\Phi}{4\omega_A\left[\alpha^2+\left(\sqrt{\omega^2+\alpha^2}-\omega\right)^2\right]}P_-, \tag{4.83}$$

$$a = \frac{k_\Phi\left(\omega-\sqrt{\omega^2+\alpha^2}\right)}{\omega_a\omega_A\left[\alpha^2+\left(\sqrt{\omega^2+\alpha^2}-\omega\right)^2\right]}P_- + \frac{g_{\Phi\gamma}A^*k_\Phi}{2\omega_A\left[\alpha^2+\left(\sqrt{\omega^2+\alpha^2}-\omega\right)^2\right]}P_+, \tag{4.84}$$

where the phase of the propagating states is $\Theta_\pm = k_\pm z - \omega t$.

4.10.1 Dilaton production via two laser beam interactions

Application of the boundary conditions (same as for the axion case) allows expression of the propagating states in terms of the probe field

$$\hat{\Phi}(0,t) = 0 \tag{4.85}$$

$$\mathbf{a}(0,t) = a\hat{\mathbf{x}} \tag{4.86}$$

$$P_{+} = \left(\frac{g_{\Phi\gamma} A \omega_A \omega_a}{4}\right) a \tag{4.87}$$

$$P_{-} = \omega_A \left(\omega - \sqrt{\omega^2 + \alpha^2}\right) a. \tag{4.88}$$

Substituting these equations back into equation (4.83), we can express the dilaton field as being proportional to the probe field a times an oscillatory term, which arises from the different phases of the propagating states.

$$\Phi = \frac{g_{\Phi\gamma} A \omega_a}{4} \frac{\left(\sqrt{\omega^2 + \alpha^2} - \omega\right)}{\left[\alpha^2 + \left(\sqrt{\omega^2 + \alpha^2} - \omega\right)^2\right]} |a| \left[e^{i\Theta_+} - e^{i\Theta_-}\right]. \tag{4.89}$$

We can express the dilaton energy and flux as

$$S_\Phi = - \partial_t \Phi \nabla \Phi \tag{4.90}$$

$$S_\Phi = g_{\Phi\gamma}^2 |A|^2 |a|^2 \frac{\omega_a^2 k_\Phi \omega_\Phi}{64\left(\omega^2 + \alpha^2\right)} \left[1 - \cos(\delta\Theta)\right] \tag{4.91}$$

$$N_\Phi = g_{\Phi\gamma}^2 I_A I_a \frac{(R-1)}{16\omega_A\left(\omega^2 + \alpha^2\right)} \left[1 - \cos(\delta\Theta)\right]. \tag{4.92}$$

There is a clear symmetry with the axion case, with the only difference being that of the constant value on the denominator, which originates from the factor of $\frac{g}{2}$ in the dilaton KG equation as opposed to g in the axion KG equation - see equations (3.19) and (3.21).

4.10.2 Dilaton-Photon oscillation starting with a dilaton

For completeness, we derive a general expression for the photon field $\mathbf{a}$ at general coordinates in terms of the dilaton field. The derivation uses the 1-D boundary condition in which the origin contains only the dilaton together with the background laser field and no initial probe laser. Since the same method was applied earlier for the complementary boundary condition (origin containing the probe and background), we only quote the final expressions here.

Using the following boundary conditions

$$\hat{\Phi}(0,t) = \Phi \tag{4.93}$$
$$\mathbf{a}(0,t) = 0, \tag{4.94}$$

expressing the propagating states in terms of the dilaton field,

$$P_{-} = \left(\frac{g_{\Phi\gamma}A^{*}\omega_A\omega_a}{2}\right)\Phi \tag{4.95}$$
$$P_{+} = \omega_A\left(\sqrt{\omega^2+\alpha^2}-\omega\right)\Phi \tag{4.96}$$

allows us to write the laser field as a superposition of the two propagating states' phases

$$a = \frac{g_{\Phi\gamma}A^{*}k_{\Phi}\left(\sqrt{\omega^2+\alpha^2}-\omega\right)}{2\left[\alpha^2+\left(\sqrt{\omega^2+\alpha^2}-\omega\right)\right]}\Phi\left(e^{i\Phi_{+}}-e^{i\Phi_{-}}\right). \tag{4.97}$$

Finally, we derive equations for the intensity and flux of the photons. Note that we have taken the time average of the oscillations to derive the results below.

$$I_a = \frac{g_{\Phi\gamma}^2|A|^2k_{\Phi}^2\omega_a^2}{16\left(\omega^2+\alpha^2\right)}|\Phi|^2\left[1-\cos(\delta\Phi)\right], \tag{4.98}$$

$$N_a = g_{\Phi\gamma}^2 I_A N_{\Phi}\frac{R(R-1)}{8\left(\omega^2+\alpha^2\right)}\left[1-\cos(\delta\Phi)\right]. \tag{4.99}$$

4.11 Chapter conclusions

Axion–photon oscillations are well established for static magnetic fields; here we generalise that formalism to the case where a laser background field provides the interaction, offering an alternative perspective on axion-photon oscillations. For realistic laboratory parameters the produced axion flux in our experimental setup can exceed the instantaneous solar axion flux at the Earth's surface and can also exceed the predicted axion fluxes associated with existing light shining through wall experiments such as OSQAR and ALPS II. Replacing a static magnetic field with a background laser changes the 'resonance condition' and therefore the axion mass range probed by the interaction. Using higher harmonics of the background laser can extend the axion mass region without the experimental constraints typical of traditional light shining through wall experiments.

Our analysis assumes a spatially and temporally constant background field; relaxing that assumption to investigate realistic pulse profiles is a natural next step. Future work will explore evolving background fields and compare axion fluxes produced by typical laser pulse shapes, to assess how pulse structure and finite interaction regions modify the coupled wave equations and resonance conditions. This will provide practical requirements for the probe and background lasers and quantify how feasible this proposed setup would be for the production and detection of axions.

Chapter 5

Laser-Axion Interactions in Plasma

5.1 Plasma - a promising medium for axion searches

Plasma as a medium for axion searches is promising as there is a vast range of plasmas, with a wide density range. Being able to control electromagnetic interactions is of interest for both astrophysical and terrestrial environments. A common motivation for using plasma in axion searches is the fact that they can produce and sustain very large field strengths. Since axions are weakly interacting, stronger sources produce higher signals. Laboratory plasma used for wakefield accelerators [76] can create extremely large fields (in excess of 100 GVm^{-1}). There are a variety of axion-plasma experiments (conceptual and actual) including: plasma wakefields [77] where the electrostatic plasma wave in conjunction with an applied magnetic field acts as a source of axions. 'Plasma shining through a wall' (PSW) experiments [78] form hybrid axion plasmons. There are also plasma haloscope experiments [79] [80], which do not utilise a plasma but instead make use of plasma-like dispersion from engineered metamaterials. These can be tuned so that the axion mass matches the 'plasma' frequency, without being restricted by a cavity volume.

Perhaps the simplest design is to investigate electrostatic modes in plasmas. In the 1-D limit, a longitudinally applied magnetic field will not disrupt the dynamics of the electrons and will maximise the source of the axions ($\mathbf{E} \cdot \mathbf{B}$ component). Given this set up, what would be the expected flux of axions from a strongly driven[1] plasma wave and how does that compare with the aforementioned sources in Section 2.2? Previous work on this topic [77], investigated a 1-D model of this and showed that the peak flux could exceed that of the axion flux generated in the Sun as measured on Earth, using realistically achievable experimental parameters. This is a promising result and deserves further and more detailed examination. A key element of this (more specific details will be given later) is to study the spectra of the axion flux. In [77] the flux was estimated by averaging over the whole spectrum. Here, we derive the full spectral distribution, obtaining a more accurate value for the flux. Before presenting the original contribution to this work in Section 5.3, we outline the key points and results of [77] and show how our approach differs in Section 5.2. In Section 5.4 and Section 5.5 we analyse the flux modal distribution and dependency on axion and plasma parameters such as axion mass, plasma frequency and gamma factor. In Section 5.7 we repeat the work this time for a scalar particle, the dilaton.

5.2 Background theory and summary of results

The work in this chapter is based on [77] and therefore a conceptual overview of that work is provided before presenting our new results in Section 5.3. A more detailed derivation of the work of [77] can be found in Appendix C.

We investigate the non-linear regime and restrict ourselves to 1-D. A well-known method [81] used to analyse travelling waves in this limit involves solu-

[1] A strongly driven plasma will highlight the nonlinearities in the Maxwell-plasma equations. This will allow for the largest electric field and consequently the largest axion source.

tions that depend on a coordinate $\zeta = x - \beta t$, which co-moves with the plasma driver, where β is the normalised phase velocity of the plasma wave. The analysis assumes that the plasma driver and the wave frame don't evolve. Due to the extremely weak axion-electromagnetic coupling, the plasma and axion equations can be solved independently, allowing the solutions for the plasma equations to be used as a source in the axion-KG equation. As the plasma is magnetised longitudinally, the electric field of the plasma wave with the applied magnetic field, acts as the source for the axions.

A key result of [77] is the derivation of an oscillator equation for an electrostatic potential in the wave frame

$$\frac{1}{2}\left(\xi'\right)^2 + \omega_p^2\gamma^2\left(\xi - \beta\sqrt{\xi^2 - \gamma^{-2}}\right) = \omega_p^2\gamma \tag{5.1}$$

$$E = -\frac{m_e}{e}\xi', \tag{5.2}$$

where ω_p is the plasma frequency and $\gamma = (1-\beta^2)^{-\frac{1}{2}}$.

This provides an analytical expression for the maximum electric field that can be achieved in the driven plasma and, by extension, as a source of axions. The turning points of the oscillator equation coincide with the electrons travelling at the phase velocity of the wave (wavebreaking) which yields the largest electric field. In calculating the energy flux of the axion an average was taken and consequently the spectral dependence of the individual axion modes was lost. The resulting axion energy and number flux are found to be

$$P_\varphi = \kappa_\varphi\left(\frac{\pi}{2s^3}[\pi s\coth^2(\pi s) + \coth(\pi s) - \pi s] - \frac{1}{s^4}\right) \tag{5.3}$$

$$N_\varphi = \frac{P_\varphi}{m_\varphi\gamma}, \tag{5.4}$$

where $\kappa_\varphi = \frac{m_e^2}{e^2}\frac{16\gamma^6 g_{\varphi\gamma}^2 B^2}{\pi^4}$. The flux is defined as the average energy flux over the estimated energy of an axion ($\mathcal{E}_\varphi = m_\varphi\gamma$). The key result of [77] is equation (5.4), which gives an estimate for the axion flux sourced from a non-linear plasma wave.

Our new result provides a more accurate representation of the expected axion flux by first considering the spectral energy flux before dividing by the axion energy per mode ($\mathcal{E}_{n\varphi} = \frac{nm_\varphi\gamma}{s}$):

$$\langle N_\varphi \rangle = \frac{k_\varphi}{m_\varphi\gamma}\sum_{n=1}^{+\infty}\frac{2s}{n(n^2+s^2)^2}. \tag{5.5}$$

As in the work of [77], our results are parametrised with the dimensionless variable s, defined as

$$s = \frac{m_\varphi\gamma\lambda}{2\pi}. \tag{5.6}$$

There is no limit of s in which our results conform to that of [77]. However, when $s \approx 1$ they are within an order of magnitude of each other as shown in Figure 5.2.

In Figures 5.1–5.3 we plot the flux derived in [77] and in this chapter (5.5) for three different parameter regions of s: $s < 1$, $s \approx 1$ and $s > 1$.

For $s < 1$ the flux of [77] will over estimate. For $s > 1$ the flux derived in this work will be greater – Figure 5.3.

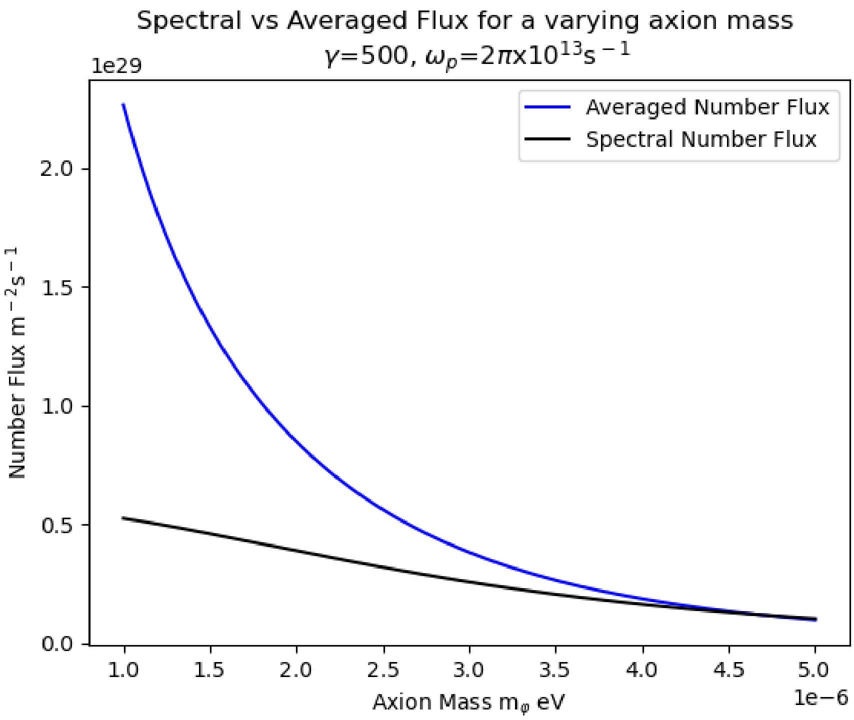

Figure 5.1: Comparison of the axion's spectral and averaged number flux. The dimensionless parameter ranges from $s = 0.24 - 1.22$ in the graph. The averaged number flux over counts for $s < 1$ and diverges from the number flux of this work.

5.2.1 Deriving the axion field

Due to the periodicity of the plasma wave, the electric field, ξ and the axion inherit the same periodicity, and can both be described using a Fourier series

$$\xi = \sum_n \xi_n \exp\left(2\pi i n \frac{\zeta}{\lambda}\right) \tag{5.7}$$

$$\varphi = \sum_n \varphi_n \exp\left(2\pi i n \frac{\zeta}{\lambda}\right). \tag{5.8}$$

The Fourier coefficients of the electric potential, ξ_n can be shown to be

$$\xi_{n\neq 0} = -\frac{4\gamma}{\pi^2 n^2} \tag{5.9}$$

$$\xi_0 = \frac{4}{3}\gamma, \tag{5.10}$$

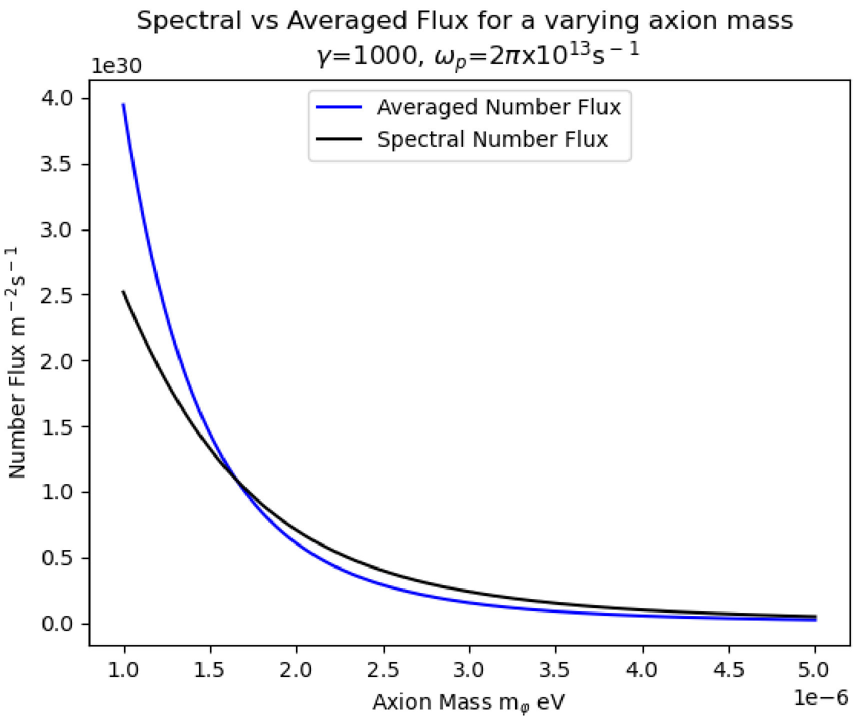

Figure 5.2: Comparison of the axion spectral and averaged flux. The dimensionless parameter ranges from $s = 0.69 - 3.44$ in the graph. Both fluxes are close in value for $s \approx 1$.

See Appendix section C.2.1 for details. The Fourier coefficient for the axion field, φ_n is derived from the axion-KG equation

$$\left(\Box + m_\varphi^2\right)\varphi = -g_{\varphi\gamma}\boldsymbol{E}\cdot\boldsymbol{B}, \tag{5.11}$$

in conjunction with equations (5.2), (5.8), (5.9) and (5.10),

$$\varphi_{n\neq 0} = -\frac{2ig_{\varphi\gamma}B_0 m_e\gamma^3\lambda}{(n^2+s^2)e\pi^2 n} \tag{5.12}$$

$$\varphi_0 = 0, \tag{5.13}$$

where $\boldsymbol{B} = B_0\hat{\mathbf{x}}$.

The factor of i and λ in the numerator of equation (5.12) contrasts with the

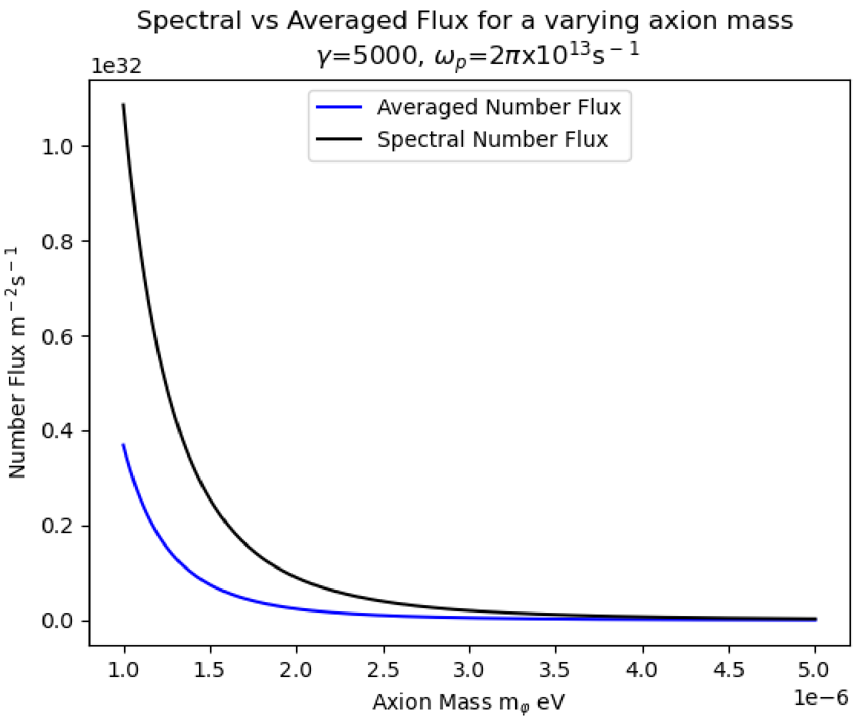

Figure 5.3: Comparison of the axion's spectral and averaged flux. The dimensionless parameter ranges from $s = 7.70 - 38.46$ in the graph.

analogous expression for a scalar particle in Section 5.7.

The axion energy flux arises from the stress energy momentum tensor and can be defined as

$$I_\varphi = -\partial_t\varphi\nabla\varphi \tag{5.14}$$

$$=\beta\varphi'^2. \tag{5.15}$$

In [77] the average energy flux is defined as

$$P_\varphi = \frac{\beta}{\lambda}\int_0^\lambda \varphi'^2 d\zeta, \tag{5.16}$$

from which it was calculated that

$$
\begin{aligned}
P_\varphi =& \beta g_{\varphi\gamma}^2 B_0^2 \frac{m_e^2}{e^2}\frac{16\gamma^6}{\pi^4}\sum_{\substack{n=-\infty\\ \neq\{0\}}}^{+\infty}\frac{1}{(n^2+s^2)^2} && (5.17)\\
=& g_{\varphi\gamma}^2 B_0^2 \frac{m_e^2}{e^2}\frac{16\gamma^6}{\pi^4}\left[\frac{\pi\left[\coth^2(\pi s)s-\pi s+\coth(\pi s)\right]}{2s^3}-\frac{1}{s^4}\right], && (5.18)
\end{aligned}
$$

where we use the symbol P_φ for the energy flux calculated in [77], as this uses similar notation. It can be obtained from our result for the energy flux, which will be denoted by I_φ, by averaging over ζ.

In computing the sum in equation (5.17) it is clear it is only a function of s and therefore information on the modes or spectral information is lost. This does not have to be the case and in going from equation (5.15) - (5.17) we can express each copy of the derivative of the axion field as a separate Fourier series. Ultimately, this will preserve the spectral information and we can analyse the individual modes of the resultant energy/number flux. These results are illustrated in the following sections, where we highlight the error accrued in the results of [77] for different parameter ranges in s.

5.3 The axion flux

To preserve the spectral information in the energy flux, we first express it as a product of two sums

$$
\varphi'^2 = \left(\frac{2\pi i}{\lambda}\sum_{\substack{n=-\infty\\ \neq\{0\}}}^{+\infty} n\varphi_n e^{2\pi i n\frac{\zeta}{\lambda}}\right)\left(\frac{2\pi i}{\lambda}\sum_{\substack{m=-\infty\\ \neq\{0\}}}^{+\infty} m\varphi_m e^{2\pi i m\frac{\zeta}{\lambda}}\right). \qquad (5.19)
$$

We express this as a Cauchy product such that the axion energy flux is

$$\varphi'^2 = -\frac{4\pi^2}{\lambda^2}\sum_{p=-\infty}^{+\infty}\left(\sum_{\substack{n=-\infty \\ \neq\{0,p\}}}^{+\infty} n(p-n)\varphi_n\varphi_{p-n}\right)e^{\frac{2\pi i p\zeta}{\lambda}} \tag{5.20}$$

$$I_\varphi(\zeta) = \kappa_\varphi \sum_{p=-\infty}^{+\infty}\left(\sum_{\substack{n=-\infty \\ \neq\{0,p\}}}^{+\infty} \frac{1}{(n^2+s^2)((p-n)^2+s^2)}\right)e^{\frac{2\pi i\zeta p}{\lambda}}, \tag{5.21}$$

where $\kappa_\varphi = \frac{\hbar c^4}{\mu_0^2}\frac{m_e^2}{e^2}\frac{16\gamma^6 g_{\varphi\gamma}^2 B^2}{\pi^4}$ is defined as in [77].

The instantaneous energy flux in equation (5.21) varies with ζ. The more meaningful, and measurable, quantity is the average energy flux, which is obtained by letting $p = 0$. However, to retain the flux modes we define a modal frequency $|n\Omega|$, where $\Omega = \frac{2\pi}{\lambda} = \frac{m_\varphi\gamma}{s}$. Dividing (5.21) by the energy of each individual mode (where $E_n = \hbar n\Omega$) results in the instantaneous number flux, with the spectral information intact. The more meaningful quantity of the average flux can then be obtained.

We compare the average flux with that of [77] below

$$\langle P_\varphi\rangle = I_\varphi(\zeta)|_{p=0} \tag{5.22}$$

$$\langle N\rangle = \frac{\kappa_\varphi}{m_\varphi\gamma}\sum_{-\infty}^{\infty}\frac{1}{(n^2+s^2)^2}, \tag{5.23}$$

$$N_\varphi(\zeta) = \frac{\kappa_\varphi}{m_\varphi\gamma}\sum_{p=-\infty}^{+\infty}\left(\sum_{\substack{n=-\infty \\ \neq\{0,p\}}}^{+\infty}\frac{s}{n(n^2+s^2)((p-n)^2+s^2)}\right)e^{ip\Omega\zeta} \tag{5.24}$$

$$\langle N_\varphi\rangle >= \frac{k_\varphi}{m_\varphi\gamma}\sum_{n=1}^{+\infty}\frac{2s}{n(n^2+s^2)^2} \tag{5.5 Revisited}$$

$$= \frac{k_\varphi}{m_\varphi\gamma}H(s). \tag{5.25}$$

It is clear that evaluation of the sum $H(s)$ results in the loss of the spectral information. However, one can analyse the modal dependence of the flux (the summand of $H(s)$) by considering various magnitudes of n vs s.

We point out that equation (5.5) resembles the Riemann zeta function

$$\sum_{n=1}^{+\infty} \frac{1}{n(n^2+s^2)^2}\bigg|_{s=0} = H(0) = \zeta_{\mathrm{Reim}}(5), \tag{5.26}$$

where ζ_{Reim} is the Riemann zeta function[2] when $H(s) \equiv H(0)$. A solution in a closed-form expression of the above sum is not possible because it is evaluated at an odd integer value. Note that for (5.23) (evaluated at $s = 0$) we have $\zeta(4)$ and a closed-form expression exists. It is the step of deriving the number flux (dividing by the modal frequency) that results in a closed-form expression not being available. We will see this again in Section (5.7) when we investigate the flux for a dilaton particle sourced by a non-linear plasma wave.

Returning to equation (5.5) and examining $H(s)$, we find that it has a peaked shape as shown in Figure 5.4. The amplitude of the curve in Figure 5.4 is approximately 0.69. This enables a quick calculation of the maximum axion flux by a strongly driven plasma wave based on the axion mass - 69% of κ_φ.

5.4 Modal decomposition of the flux

The total flux $\langle N_\varphi \rangle$ does not depend on the mode number n. However, the modal flux $h(s)$

$$H(s) = \sum_{n=1}^{n=\infty} h_n(s) \tag{5.27}$$

, does depend on n, which is a key contribution of this work. The modal flux will be analysed in three regions: $s < n$, $s \approx n$, $s \gg n$. In general, without

[2]This use of ζ_{Riem} is specific to this instance only. Outwith here it should not be confused with the coordinate defined as $\zeta = x - \beta t$.

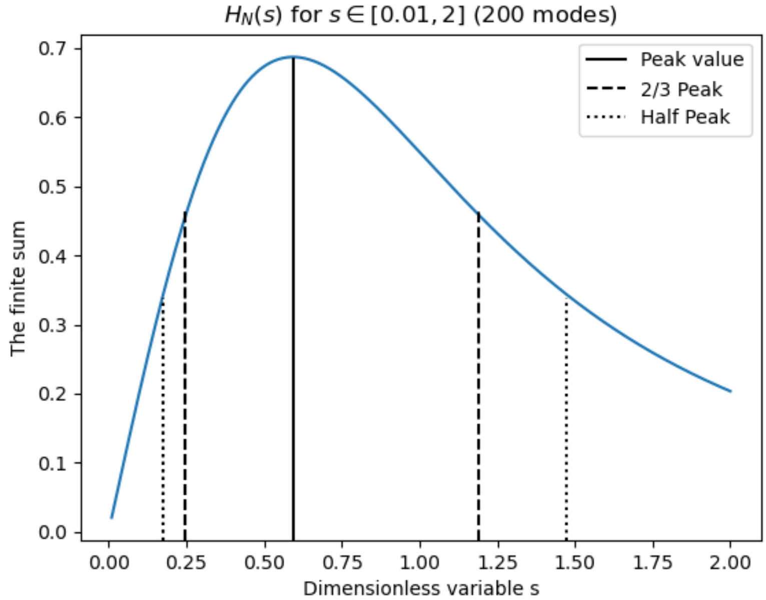

Figure 5.4: The finite-sum $H_N(s)$ is shown for the continuous variable s. The peak occurs at $s = 0.59$ with a value of 0.687, and the vertical lines mark the peak, two-thirds peak, and half-peak positions which occur at 0.25, 1.19 and 0.17, 1.47 respectively.

confining ourselves to one of these regions, one can see that the majority of the contribution comes from the first few modes. Therefore, one can explicitly sum several modes yielding a close approximation to the total flux. Recall that a closed-form expression does not exist. The exact number of modes required depends on s and will be investigated in Section 5.4.1.

Figures 5.5 - 5.7 illustrate the flux contained within the first 10 modes for three different values of s. Clearly, the fundamental mode is the most dominant, but other modes can have a considerable flux when $s > 1$. This is illustrated in Figure 5.7, with each mode containing a non-negligible amount of flux. Analysing the number flux, equation (5.5), for this regime, we have an approximate linear decrease in the flux with mode number. For $s < n$ and $s \approx n$ the modal number flux drops off with the mode number to the power 5, resulting in the first few modes containing the majority of the flux, as seen in Figure 5.5 and 5.6. As s does

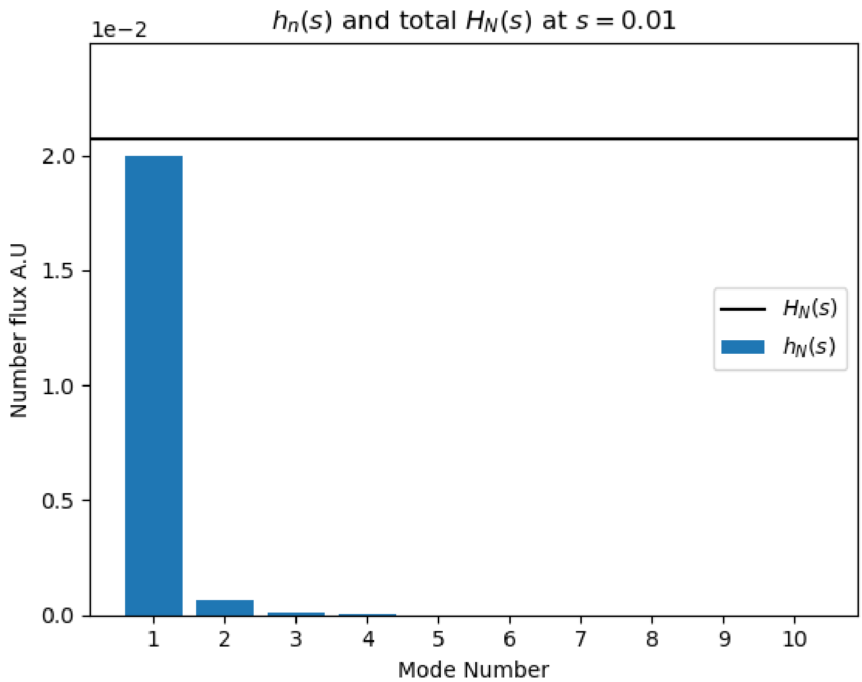

Figure 5.5: When $s = 0.01$ $h_1(s)$ the flux contribution comprising roughly 96% of the total flux.

not have to be an integer, it is possible for $s < n$ for all modes, whereas it is only possible for $s > n$ for a finite number of modes. Figures 5.8 and 5.9 demonstrate this by plotting the modal flux for two regimes of s ($s \ll 1$ and $s \gg 1$). For visualization, we represent the modal data (integer n) with continuous curves An^{-5} and Bn^{-1} to demonstrate the two distinct behaviours. Treating n as a continuous variable in the plotted fits is solely a graphical device to make the dependence clear; the calculated flux remains a sum over integer n. The plotted curves are scaled so each comparison appears on the same vertical range, allowing the change between the two regimes to be seen at a glance.

5.4.1 Truncating the infinite series

A closed form expression for the total axion flux does not exist. To evaluate the infinite series $H(s)$ (5.5) we must make an approximation by truncating the series

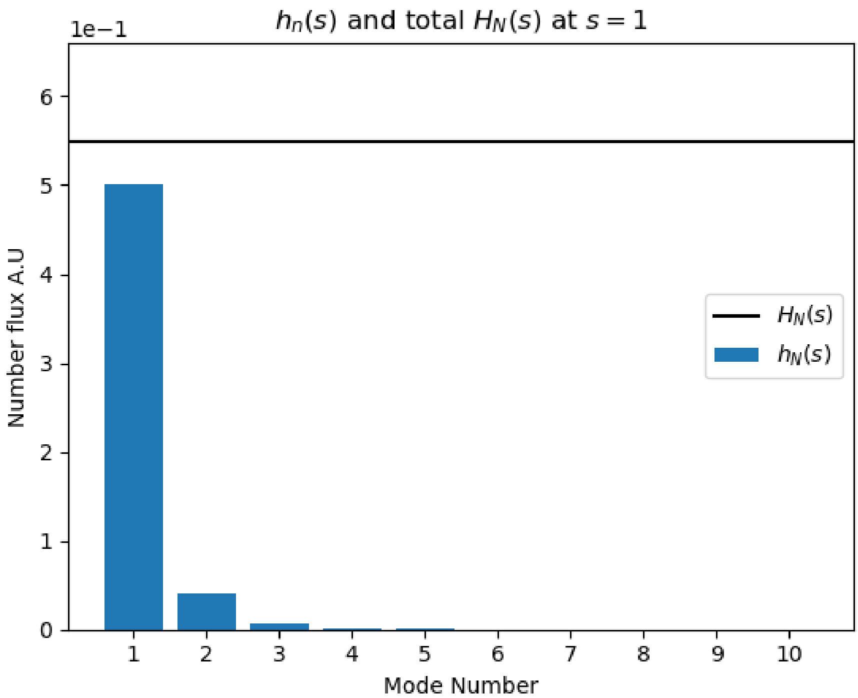

Figure 5.6: Even for $s = 1$ $h_n(1)$ drops off rapidly as $s < n$. $h_1(1)$ contributes approximately 91% of the total flux.

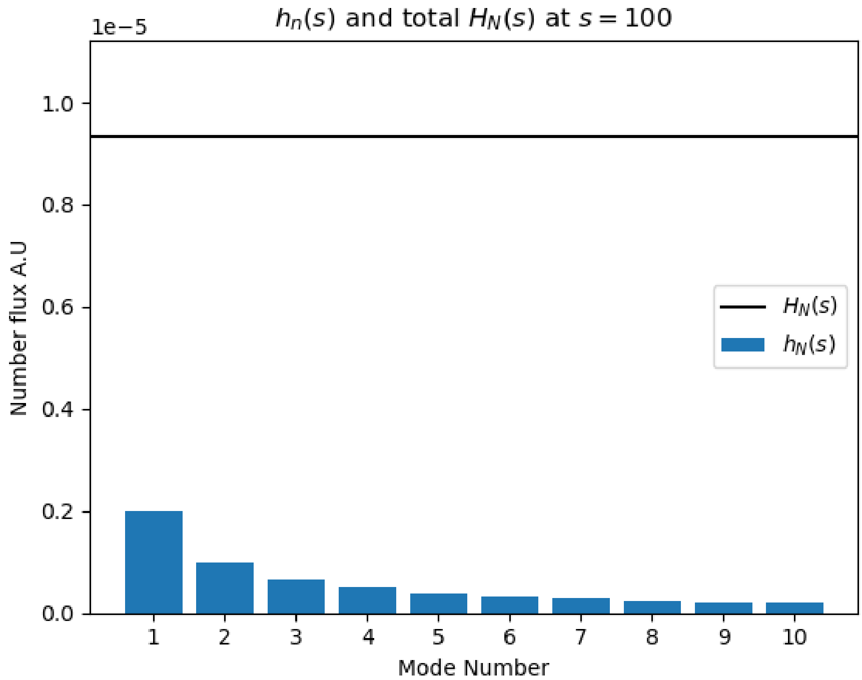

Figure 5.7: As s gets larger the contributions from each consecutive $h_n(s)$ mode become comparable. In this example $h_1(100)$ contributes roughly 21% of the total flux.

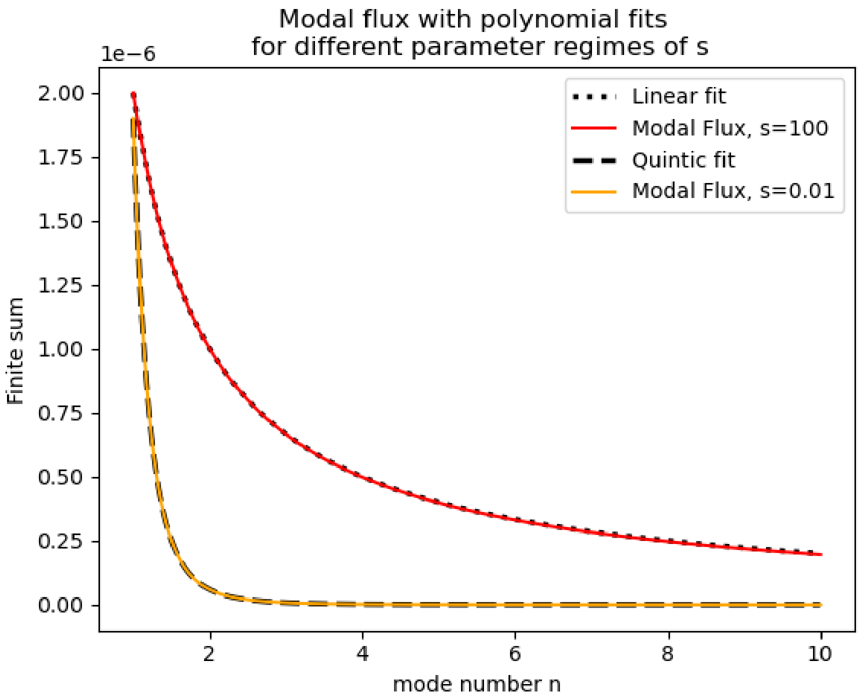

Figure 5.8: For the orange curve the parameter s will always be less than the mode number resulting in the flux being inversely proportional to n^5. For the red curve, initially $s \gg n$ causing a linear drop-off with n. However, there will exist a set of mode numbers for which $s \ll n$ and the flux's relationship with the mode number will change - see Figure 5.9.

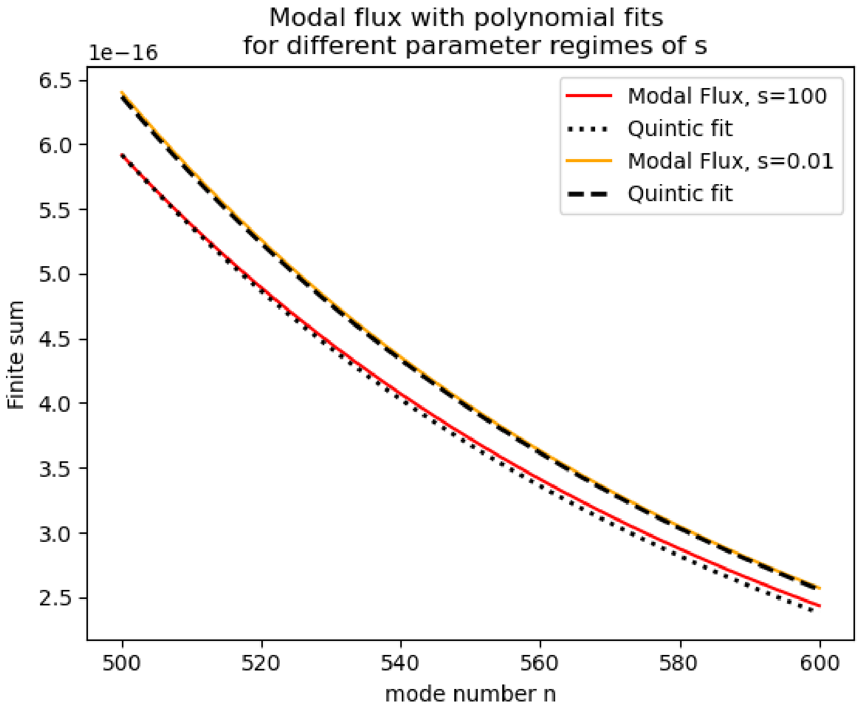

Figure 5.9: Again, for the orange curve we have $s \ll 1$ and the same relationship as seen in Figure 5.8 is shown. For the red curve, in this range of mode numbers $s \ll n$ and the flux's relationship with mode number is now inversely proportional to n^5.

at a finite number N

$$\sum_{n=1}^{\infty} \frac{1}{n(n^2+s^2)^2} \approx \sum_{n=1}^{N} \frac{1}{n(n^2+s^2)^2}. \tag{5.28}$$

We know that the number flux drops off with mode number faster than the energy flux, thus the upper bound of the finite series that approximates the infinite series of the energy flux will also be a good upper bound for the approximation of the number flux series:

$$\text{If} \quad \sum_{n=1}^{N} \frac{1}{(n^2+s^2)^2} \approx \sum_{n=1}^{\infty} \frac{1}{(n^2+s^2)^2}, \tag{5.29}$$

$$\text{then} \quad \sum_{n=1}^{N} \frac{1}{n(n^2+s^2)^2} \approx \sum_{n=1}^{\infty} \frac{1}{n(n^2+s^2)^2}. \tag{5.30}$$

A closed-form expression exists for the energy flux, and thus finding a suitable N for a given value of s is straightforward. Our criteria for what makes N suitable are that the resulting values obtained from the finite sum are within 5% of the value obtained from evaluating the closed-form expression. As the number flux falls off with a factor of $1/n$ more than the energy flux, the error will be less than 5% for the number flux approximation. We illustrate this numerically in table (5.1) for different s values, concluding that, as a rule of thumb, provided $N = 2s$ the approximation is sound. Note that, for $s = 1$ three modes provide a result of 97.8% the value of the closed-form expression, whereas only two modes yield 94.5%, thus for the range of numbers provided in table (5.1) this is the exception to our stipulation. For $s < 1$ two modes are also needed.

The last two lines of table 5.1 are the values of s used in our numerical calculation of the axion flux in Section 5.6. In those calculations 100 modes were summed to obtain the result.

Table 5.1: Upper bound on the mode number needed to obtain an approximation of the closed form result

s	N	Closed form $C(s)$	$H_N(s)$	Error (%)
0.1	2	2.12	2.08	1.9
1	2	0.614	0.580	5.5
10	20	1.471×10^{-3}	1.411×10^{-3}	4.1
100	200	1.561×10^{-6}	1.498×10^{-6}	4.0
1000	2000	1.570×10^{-9}	1.506×10^{-9}	4.0
10000	20000	1.571×10^{-12}	1.507×10^{-12}	4.0
2.18	100	0.173	0.173	<0.1
43.52	100	1.878×10^{-5}	1.824×10^{-5}	2.84

The headers in table (5.1) are defined as

$$C(s) = \left(\frac{\pi}{2s^3}[\pi s \coth^2(\pi s) + \coth(\pi s) - \pi s] - \frac{1}{s^4}\right) \tag{5.31}$$

$$H_N(s) = \sum_{n=1}^{N} \frac{2}{(n^2+s^2)^2}. \tag{5.32}$$

We can see from Table (5.1) truncating the infinite series at a mode number equal to that of twice the value of s yields a numerical result within about 5% the true answer[3]. Given this, we always truncate our series for the number flux (5.5) at a mode number at least twice the value of the largest value of s (if varying any variable implicit in s there will naturally be a range of s values present). For the majority of the results and plots in this chapter 100 modes will be summed unless otherwise stated. In this way, we can soundly conclude that our truncated series closely approximates the exact result. One can see that the number of modes summed in the previous Figures 5.5 - 5.7 were sufficient to approximate the total flux.

[3]Up to a value of $s = 10,000$. The largest s value used in this work is $s = 43.52$.

5.5 Flux dependence on axion and plasma parameters

In this section, we explore how the axion flux depends on the axion mass, plasma wave gamma factor, and plasma frequency. Before illustrating the results graphically, we briefly return to equation (5.5), expressing it in a slightly different manner, such that the dependencies on these parameters are more clearly visible.

$$\langle N_\varphi \rangle = \frac{k_\varphi}{m_\varphi \gamma} \sum_{n=1}^{\infty} \frac{2s}{n(n^2+s^2)^2} \tag{5.5 Revisited}$$

$$\langle N_\varphi \rangle \propto \frac{\gamma^{\frac{13}{2}}}{\omega_p} \sum_{n=1}^{+\infty} \frac{1}{n\left(n^2 + \bar{\beta}\left(\frac{m_\varphi \gamma^{\frac{3}{2}}}{\omega_p}\right)^2\right)^2}, \tag{5.33}$$

where we have used

$$s = \frac{2\sqrt{2}}{\pi} \frac{m_\varphi \gamma^{\frac{3}{2}}}{\omega_p} \frac{c^2}{\hbar}, \tag{5.34}$$

which has the factors of c and $\hbar$ restored, and where $\bar{\beta} = \frac{8c^4}{\pi^2\hbar^2}$.

We can see plainly increasing the axion mass reduces the flux. This is understandable as heavier axions have a higher energy, thus fewer are required to produce a given energy flux - recall that equation (5.5) is derived from the energy flux (5.21). The dependence of the flux on γ and ω_p is slightly more complicated, with the prefactor in (5.33) leading to an increase/reduction, whereas the denominator inside the sum reduces/increases the overall flux, respectively.

For the parameter choice in Figures 5.10 - 5.14, the axion number flux reaches $N_\varphi \approx (10^{24} - 10^{27})\mathrm{m}^{-2}\mathrm{s}^{-1}$, which is large compared to typical laboratory axion sources. However, this reflects a deliberately favourable choice of axion mass and plasma parameters, and does not imply easy detectability: any realistic experiment would require reconversion with probabilities $P_{\varphi\to\gamma} \approx 10^{-17}$ (typical for a LSW set up - see section 2.2.1). Additionally, our calculation assumes an idealised 1D geometry without transverse losses or detector noise. The result should therefore be interpreted as an optimistic upper bound on the axion flux, not as a directly observable photon signal. Furthermore, in Figures 5.10 – 5.14, maximum s refers only to the largest value of the dimensionless parameter s reached in the parameter scan; it is not a physical bound.

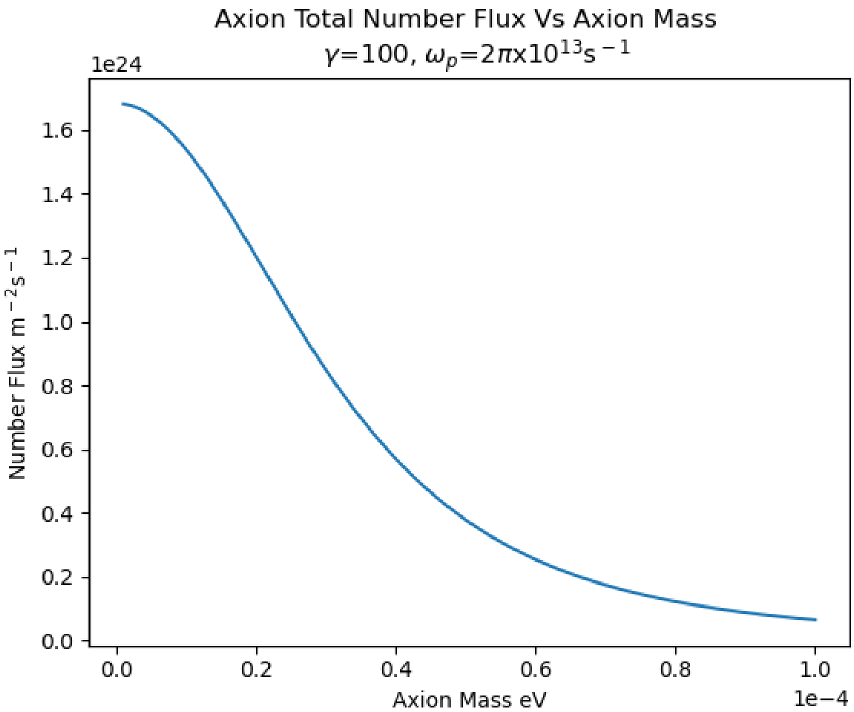

Figure 5.10: The total axion number flux for an increasing axion mass. The maximum value of the dimensionless parameter reached in this scan is $s = 2.2$. Additionally, 100 modes have been summed for each value of the axion mass to give the total flux.

As can be seen in Figure 5.10, larger axion mass reduces the flux. Note that the shape of the graph is similar to that in [77], for the energy flux rather than number flux. This is due to the fact that in [77] to obtain the number flux, the total energy flux is divided by the 'typical' axion energy $(m_\varphi\gamma)$ as opposed to the 'spectral' energy ($\frac{nm_\varphi\gamma}{s}$). In the latter case, the factor of s cancels out the factor of m_φ, which cannot happen in the former case. This highlights the differences between Figure 5.10 of this work and its counter-part in [77], in addition to the similarity in the shape of figure 5.10 with the corresponding figure of the energy flux in [77]. Furthermore, this difference leads to a finite result as $m_\varphi \to 0$ compared with the divergent result obtained in [77].

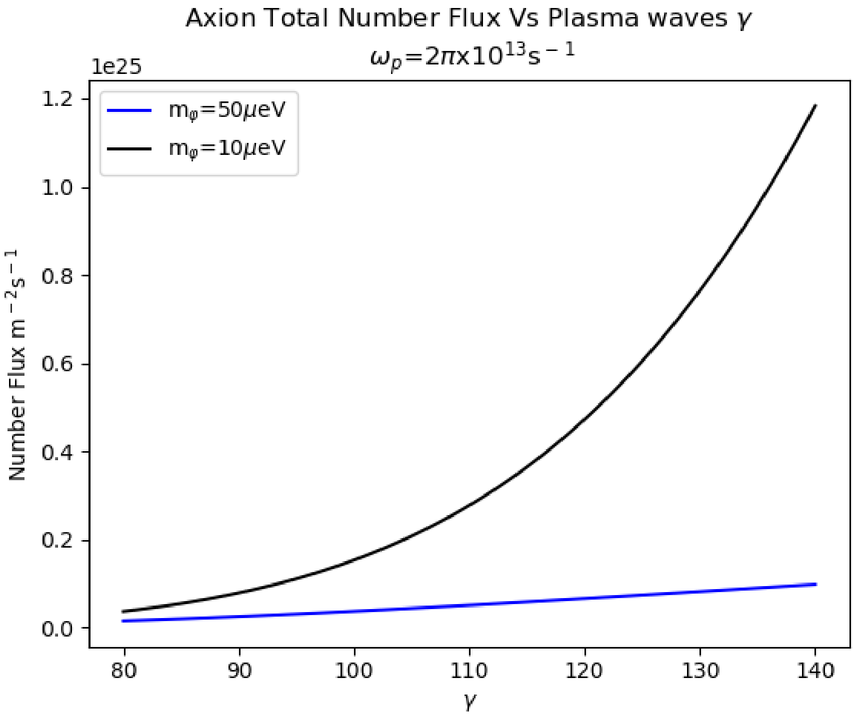

Figure 5.11: Increases in γ leads to a rapid increase in the number flux. The maximum value of the dimensionless parameter reached in this scan is $s = 1.8$ (black curve) and $s = 0.36$ (blue curve). Additionally, 100 modes have been summed for each value to give the total flux.

Comparable with the analysis of [77] we find that the graph of the flux vs gamma is sensitive to the axion mass - Figure 5.11. However, this is not unique to the axion mass as the same sensitivity is present, and potentially more important, in the plasma frequency (given that we can control this) - see Figure 5.12 below.

Instead, this is purely due to the high powers of γ present in both the prefactor and summand of the number flux; see equation (5.33). On inspection of this equation, we see that, for increasing axion/laser parameters, the gamma factor only increases the flux, whereas the axion mass only decreases it. Lastly, varying the plasma frequency can result in an increase or decrease, thus more attention should be placed on it to properly optimise the flux: see Figures 5.12–5.13. One final difference between the flux of this work and that off [77] is that the power of γ is larger in equation (5.33) than the flux of [77]. This is for the same reason, as previously discussed for varying the axion mass. Dividing by the 'spectral' frequency leads to a different γ dependence in the prefactor.

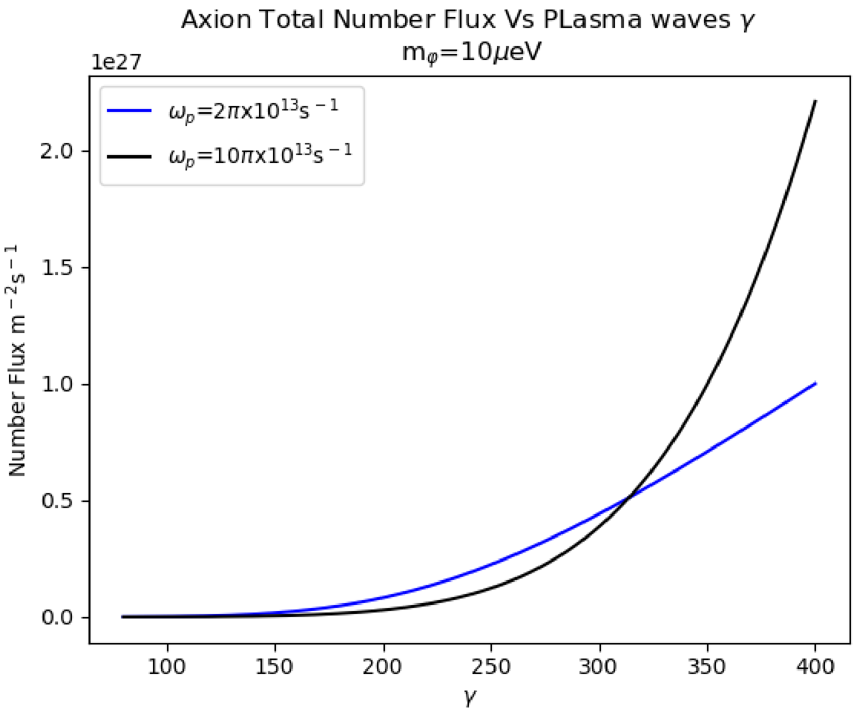

Figure 5.12: The total axion number flux for an increasing γ factor. The maximum value of the dimensionless parameter reached in this scan is $s = 1.74$ (black curve) and $s = 0.35$ (blue curve). Additionally, 100 modes have been summed for each value to give the total flux.

Figures 5.12 and 5.13 show that whether increasing the plasma frequency

(ω_p) raises or lowers the axion flux depends on the value of γ. For small γ, the part of the flux expression outside the modal sum dominates and the flux varies inversely with ω_p thus increasing it reduces the flux. For larger γ, the term involving $\bar{\beta}\left(\frac{m_\varphi \gamma^{\frac{3}{2}}}{\omega_p}\right)^2$ inside the sum becomes dominant. In this regime, increasing ω_p increases the flux. In short, increasing ω_p does not guarantee a larger flux.

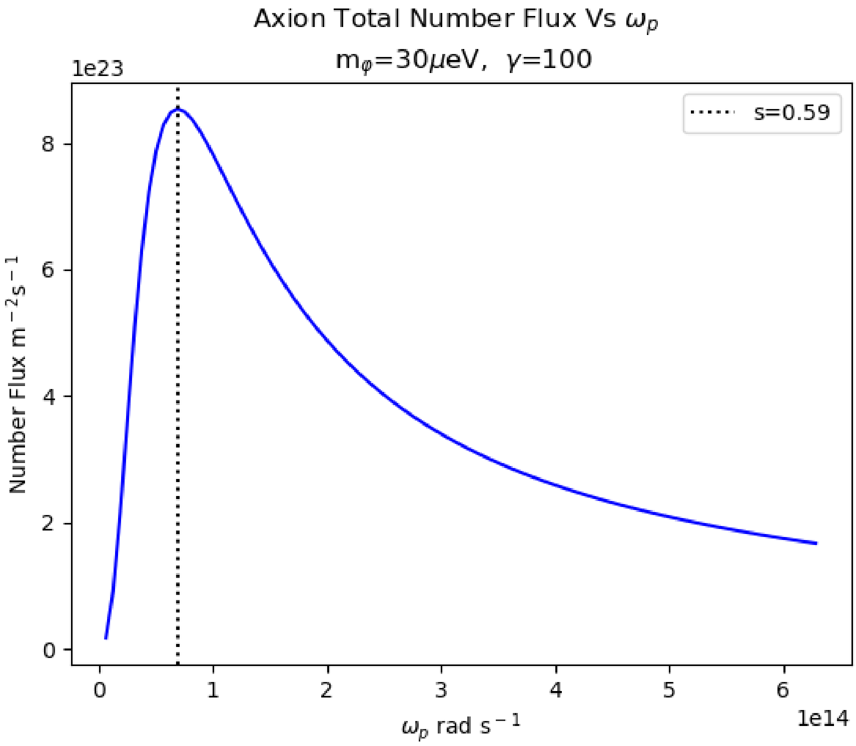

Figure 5.13: Axion flux as a function of plasma frequency. The maximum value of the dimensionless parameter reached in this scan is $s = 4.1$. Additionally, 100 modes have been summed for each value to give the total flux.

Figure 5.13 illustrates that flux can be optimised by varying the plasma frequency. Increasing the plasma frequency increases the flux (the parameter s is inversely proportional to the plasma frequency) until it peaks, after which a further increase in the plasma frequency results in a decrease. The value of s at which the flux is reduced by a third is $s = 0.25$ or 1.19 and for a reduction of 50% is $s = 0.17$ or 1.47. [4] The peak value of the flux (for $s = 0.59$) is $N_{\text{peak}} = 0.69 \times \frac{\kappa_\varphi}{m_\varphi \gamma}$. This provides a simple way of determining the maximum flux for a driven plasma wave and particular axion mass. The electron density required to achieve this is

$$n_{peak} = 2.3 m_\varphi^2 \gamma^3 \frac{m_e \epsilon_0}{e^2} \tag{5.35}$$

$$= 1.20 \times 10^{21} \gamma^3 \left[\frac{m_\varphi}{\text{eV}}\right]^2 \text{cm}^{-3}. \tag{5.36}$$

However, for a set of axion-laser parameters it may not be physically possible to reach the theoretical maximum flux due to the plasma becoming over-dense.

Future advances in laser plasma technologies will likely result in larger γ values being more achievable. It is worth analysing parameter values resulting in large s values ($s > 1000$). From equation (5.33) we see that there is a factor of $\gamma^{\frac{1}{2}}$ (assuming γ is the dominant term) in the number flux. This is illustrated in Figure 5.14.

In this regime ($s \gg 1$), the modal distribution of the flux broadens and the error accrued by the previous work on this topic, [77], is more pronounced, Figure 5.3.

5.6 Comparisons with past and ongoing experiments

We aim to compare numerical results from the non-linear plasma-wave–sourced axions to existing laboratory experiments, namely OSQAR and ALPS II, which were also used as benchmarks in Chapter 4.

For OSQAR [53] we estimate an axion flux of around $N_\varphi = 1.02 \times 10^9$ m^{-2}s^{-1}

[4]Figure 5.4 also illustrated these points.

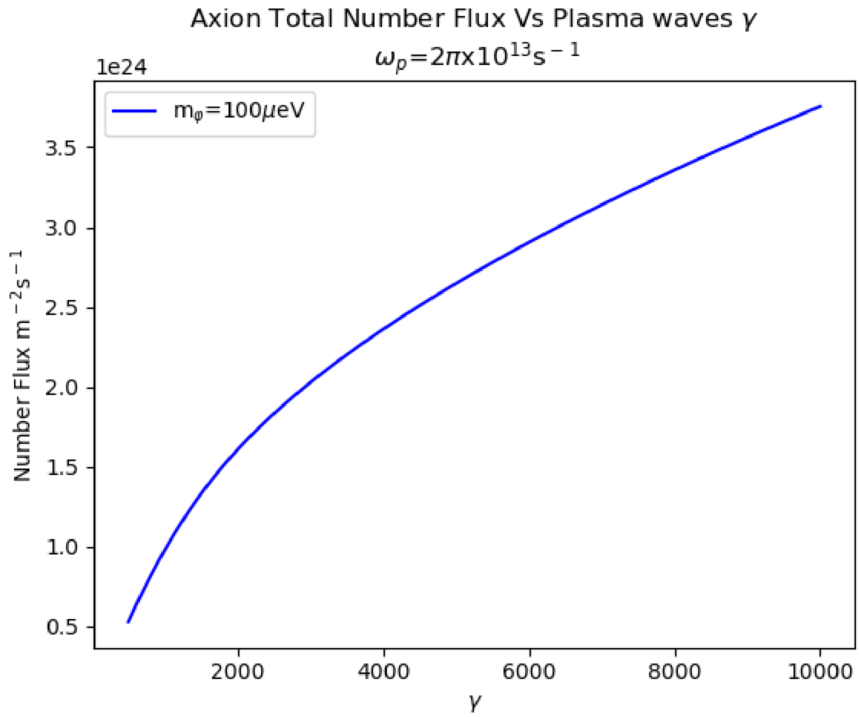

Figure 5.14: The produced number flux vs γ for $\gamma = (500 - 10,000)$. The growth of the curve slows down as γ is increased, resembling that of a graph of $y = \sqrt{x}$.

could be sourced by using the Verdi V18 laser[5] and the magnetic field stated in the paper (L = 14.3 m, B = 9 T). We have assumed an axion electromagnetic coupling constant of $g_{\varphi\gamma} = 0.66{\times}10^{-10}$ GeV^{-1} (within their projected bounds) and an axion mass of $m_\varphi = 1$ μeV, where the photon to axion conversion probability[6] is optimised (equation (2.10)). For comparison, we estimate the ALPS II experiment[7] at DESY [75] has an axion flux of $N_\varphi = 7.35 \times 10^{13}$ m^{-2}s^{-1}[8] assuming an electromagnetic coupling of $g_{\varphi\gamma} = 2 \times 10^{-11}$ GeV^{-1}. The two values of $g_{\varphi\gamma}$ differ because OSQAR and ALPS II target different regions of axion parameter space: OSQAR operates at couplings around $g_{\varphi\gamma} = 10^{-10}$GeV^{-1} , whereas ALPS

[5]The Verdi is a laser system built by Coherent.

[6]We have estimated the photon flux of the Verdi V18 to be $N_{\text{Verdi}} = 2.5 \times 10^{25}$ m^{-2}s^{-1}.

[7]We have estimated the photon flux of the Monolith Mephisto MOPA to be $N_{\text{MOPA}} = 2.4 \times 10^{30}$ m^{-2}s^{-1}.

[8]IF we assume the stronger coupling the resultant flux would be $N_\varphi = 8.0 \times 10^{13}$m^{-2}s^{-1}

II is designed to probe much smaller couplings, down to $g_{\varphi\gamma} = 2 \times 10^{-11}\text{GeV}^{-1}$. I therefore use the value of $g_{\varphi\gamma}$ appropriate to each experiment's published sensitivity.

In the work presented, the axion flux scales inversely with the axion mass and increases with the γ factor , so maximizing γ yields the largest flux. The flux is maximized when $s = 0.59$, which fixes the plasma frequency; however, achieving this may be impractical if the required electron density becomes too large. For an electromagnetic coupling of $g_{\varphi\gamma} = 0.66\times10^{-10}$ GeV^{-1}, a plasma wave Lorentz factor of $\gamma = 10,000$ (equivalent to a wakefield driven by a 5 GeV electron[9]), an applied magnetic field of $B = 35$ T (roughly the largest realistic laboratory superconducting magnet), plasma frequency of $\omega_p = 2\pi \times 10^{14}$ rad s^{-1} ($n_e = 1.24 \times 10^{26}$ m^{-3}) and an axion mass of $m_\varphi = 1$ μeV[10], we calculate an axion flux of $N_\varphi = 6.45 \times 10^{34}$ m^{-2}s^{-1}.

The value $N_\varphi = 6.45 \times 10^{34}\,\text{m}^{-2}\text{s}^{-1}$ obtained for the parameter set above is undeniably large and demonstrates that strongly driven plasma waves can, in principle, act as extremely efficient axion sources. This result merits further investigation, particularly because it arises from a regime in which the plasma wave is both highly relativistic and tuned close to the optimal value $s \approx 0.59$. However, it is important to emphasise that this flux represents the peak instantaneous flux generated during a single oscillation of a one-dimensional plasma wave. The calculation does not include transverse dynamics, geometric losses, finite interaction length, or any averaging over the pulse envelope or repetition rate. As a consequence, the quoted flux should be interpreted as an optimistic upper bound within an idealised one-dimensional model rather than a continuous or time-averaged flux. A realistic experimental configuration would inevitably yield a smaller effective flux, but the magnitude of the peak value neverthe-

[9]Electrons have been accelerated to such energies using laser plasma wakefield accelerators [82, 83]

[10]$s = 2.18$.

less indicates that relativistic plasma waves remain a compelling and potentially powerful axion production mechanism. Moreover, any realistic detection scheme requires reconversion of axions back into photons, and the associated probability $P_{\varphi\to\gamma} \sim g_{\varphi\gamma}^2 B^2 L^2$ is extremely small, so the observable photon flux would be many orders of magnitude lower than the peak axion flux calculated here.

As shown in Figure 5.10, the flux scales poorly with axion mass. If the axion mass is closer to the optical range $m_\varphi = 1$ eV the flux with the same parameters[11] would be $N_\varphi = 3.76 \times 10^{11}\ \mathrm{m^{-2}s^{-1}}$.

5.7 Dilaton

We now study the production of scalar particles (particles coupled to the electromagnetic invariant $(\mathbf{E^2} - \mathbf{B^2})$ instead of pseudoscalar particles (coupled to the invariant $\mathbf{E}\cdot\mathbf{B}$). From its coupling to electromagnetic fields one can show that the corresponding Klein-Gordon equation for scalar particles is:

$$\left(\Box + m_\Phi^2\right)\Phi = \frac{g_{\Phi\gamma}}{2}\left(E^2 - B^2\right), \tag{5.37}$$

where the full derivation for the Lagrangian is presented in Chapter 3. The plasma dynamics outlined and derived in Section C.2 are independent of the axion/dilaton. As was noted in Section 5.2, the weak coupling of these particles enables the plasma equations to be solved independently of the particle and the solutions used as sources in the respective Klein-Gordon equation.

Comparing the dilaton Klein–Gordon equation (5.37) with the axion Klein–Gordon equation (5.11) highlights a structural difference in how the electromagnetic fields contribute to the particle flux. For the dilaton, the flux is maximised by orienting

[11] $s = 2.18 \times 10^6$.

the magnetic field so that its contribution vanishes. Setting $B_0 = 0$ T. This gives

$$\Phi - \frac{\Phi''}{m_\Phi^2\gamma^2} = \frac{g_{\Phi\gamma}m_e^2}{2e^2m_\Phi^2}\left(\xi'\right)^2, \tag{5.38}$$

where we have used equation (5.2). By contrast, the axion flux is maximised with a nonzero magnetic-field configuration. In both cases the flux is sourced by a product of electromagnetic fields. For the dilaton, this is through its quadratic dependence on ξ'. We expand the fields in Fourier series and represent ξ'^2 accordingly before evaluating the flux explicitly.

$$\Phi = \sum_{n=-\infty}^{\infty} \Phi_n e^{\frac{2\pi n\zeta}{\lambda}} \tag{5.39}$$

$$\xi'^2 = \sum_{n=-\infty}^{+\infty} \chi_n e^{\frac{2\pi i n\zeta}{\lambda}}, \tag{5.40}$$

$$\sum_{n=-\infty}^{+\infty} \Phi_n e^{\frac{2\pi i n\zeta}{\lambda}} = \frac{g_{\Phi\gamma}m_e^2\gamma^2\lambda^2}{8\pi^2e^2}\sum_{n=-\infty}^{+\infty}\frac{\chi_n}{(n^2+s^2)}e^{\frac{2\pi i n\zeta}{\lambda}}. \tag{5.41}$$

Our previous results (equations (5.9) and (5.10)) can be used to explicitly calculate ξ'^2

$$\xi = \sum_{n=-\infty}^{+\infty} \xi_n e^{\frac{2\pi i n\zeta}{\lambda}} \tag{5.42}$$

$$= \frac{4\gamma}{3} - \frac{4\gamma}{\pi^2}\sum_{\substack{n=-\infty \\ n\neq 0}}^{+\infty}\frac{1}{n^2}e^{\frac{2\pi i n\zeta}{\lambda}} \tag{5.43}$$

$$\xi' = -\frac{8\gamma i}{\pi\lambda}\sum_{\substack{n=-\infty \\ n\neq 0}}^{+\infty}\frac{1}{n}e^{\frac{2\pi i n\zeta}{\lambda}}. \tag{5.44}$$

We can then express ξ'^2 as a product of two Fourier series, and use the same method as was used to obtain the expression for the axion flux, and manipulate it to produce a new Fourier series with coefficient that is a Fourier series

$$\xi'^2 = -\frac{64\gamma^2}{\pi^2\lambda^2}\left(\sum_{\substack{m=-\infty \\ m\neq 0}}^{+\infty} \frac{e^{\frac{2\pi i m\zeta}{\lambda}}}{m}\right)\left(\sum_{\substack{p=-\infty \\ p\neq 0}}^{+\infty} \frac{e^{\frac{2\pi i p\zeta}{\lambda}}}{p}\right). \tag{5.45}$$

We replace variable m with a new variable n, $n = m + p$

$$\xi'^2 = -\frac{64\gamma^2}{\pi^2\lambda^2}\sum_{n=-\infty}^{+\infty}\left(\sum_{\substack{p=-\infty \\ p\neq\{0,n\}}}^{+\infty} \frac{1}{p(n-p)}\right) e^{\frac{2\pi i n\zeta}{\lambda}}, \tag{5.46}$$

as our outer sum will now be in the newly introduced variable n, both the exclusion conditions must be placed on the inner sum over p, as this variable will effectively be 'summed out' leaving only variables in n. This is now in the same format as equation (5.40), where

$$\chi_n = -\frac{64\gamma^2}{\pi^2\lambda^2}\sum_{\substack{p=-\infty \\ p\neq\{0,n\}}}^{+\infty} \frac{1}{p(n-p)}. \tag{5.47}$$

Returning to (5.41) we have

$$\Phi_n = -\frac{8 g_{\Phi\gamma} m_e^2 \gamma^4}{\pi^4 e^2 (n^2+s^2)}\sum_{\substack{p=-\infty \\ p\neq\{0,n\}}}^{+\infty} \frac{1}{p(n-p)}. \tag{5.48}$$

We now evaluate the sum appearing in (5.48) for the case $n \neq 0$. The summand admits the partial–fraction decomposition such that

$$S_n \equiv \sum_{\substack{p=-\infty \\ p\neq\{0,n\}}}^{+\infty} \frac{1}{p(n-p)} = \frac{1}{n}\sum_{\substack{p=-\infty \\ p\neq\{0,n\}}}^{+\infty}\left(\frac{1}{p}+\frac{1}{n-p}\right). \tag{5.49}$$

Because the individual series $\sum 1/p$ and $\sum 1/(n-p)$ are divergent, the entire expression must be interpreted in the Cauchy principal value sense:

$$\mathrm{PV}\sum_{p=-\infty}^{+\infty} f(p) \equiv \lim_{N\to\infty}\sum_{p=-N}^{N} f(p). \tag{5.50}$$

We define the principle value of the first term as,

$$A \equiv \mathrm{PV}\sum_{\substack{p=-\infty\\ p\neq\{0,n\}}}^{+\infty} \frac{1}{p}. \tag{5.51}$$

Using symmetric limits we have,

$$\sum_{\substack{p=-N\\ p\neq 0}}^{N} \frac{1}{p} = \sum_{p=1}^{N}\left(\frac{1}{p}-\frac{1}{p}\right) = 0, \tag{5.52}$$

therefore, removing the excluded term $p = n$ yields

$$A = -\frac{1}{n}. \tag{5.53}$$

We define the principle value of the second term as

$$B \equiv \mathrm{PV}\sum_{\substack{p=-\infty\\ p\neq\{0,n\}}}^{+\infty} \frac{1}{n-p} = \mathrm{PV}\sum_{\substack{q=-\infty\\ q\neq\{0,n\}}}^{+\infty} \frac{1}{q}. \tag{5.54}$$

By the same symmetric–cancellation argument we find

$$B = -\frac{1}{n}. \tag{5.55}$$

Combining the two principal values yields,

$$S_n = \frac{1}{n}(A+B) = \frac{1}{n}\left(-\frac{1}{n}-\frac{1}{n}\right) = -\frac{2}{n^2}. \tag{5.56}$$

The Fourier coefficient for the dilaton (for $n \neq 0$) is therefore:

$$\Phi_n = \frac{16 g_{\Phi\gamma} m_e^2 \gamma^4}{\pi^4 e^2 n^2 (n^2 + s^2)}. \tag{5.57}$$

Note here the factor of i difference when compared to its axion counter-part φ_n (5.12), indicating a difference in phase between the two cases. Additionally, there is no dependence on the wavelength, which results in a different relationship between the dilaton flux and plasma frequency, compared with the axion case - see Figure 5.21. Lastly, the additional factor of n in the denominator results in a more concentrated flux within the first few modes, compared with the case of a pseudoscalar particle (Figures 5.15 – 5.17 illustrate this).

Returning to equation (5.48) and considering the case where $n = 0$, we have:

$$\Phi_0 = -\frac{8 g_{\Phi\gamma} m_e^2 \gamma^4}{\pi^4 e^2 (n^2 + s^2)} \sum_{\substack{p=-\infty \\ p \neq \{0,n\}}}^{+\infty} \frac{1}{p(n-p)} \Bigg|_{n=0} \tag{5.58}$$

$$= \frac{8 g_{\Phi\gamma} m_e^2 \gamma^4}{\pi^4 e^2 s^2} \sum_{\substack{p=-\infty \\ p \neq 0}}^{+\infty} \frac{1}{p^2}$$

$$= \frac{8 g_{\Phi\gamma} m_e^2 \gamma^4}{3\pi^2 e^2 s^2}, \tag{5.59}$$

where we have used the fact that $\sum_{p=1}^{+\infty} \frac{1}{p^2} = \frac{\pi^2}{6}$.

As the energy flux of the dilaton is proportional to Φ'^2 we first derive the explicit form of the derivative Φ', then square it afterwards

$$\begin{aligned}\Phi' =& \frac{2\pi i}{\lambda}\sum_{n=-\infty}^{+\infty} n\Phi_n e^{\frac{2\pi i n\zeta}{\lambda}} \\ \Phi' =& \frac{32 i g_{\Phi\gamma} m_e^2 \gamma^4}{\pi^3 e^2 \lambda}\sum_{\substack{n=-\infty\\ n\neq 0}}^{+\infty} \frac{1}{n(n^2+s^2)} e^{\frac{2\pi i\zeta}{\lambda}}\end{aligned} \tag{5.60}$$

$$\Phi'^2 = -\frac{1024 g_{\Phi\gamma}^2 m_e^4 \gamma^8}{\pi^6 e^4 \lambda^2}\left(\sum_{\substack{m=-\infty\\ m\neq 0}}^{+\infty} \frac{1}{m(m^2+s^2)} e^{\frac{2\pi i m\zeta}{\lambda}}\right)\left(\sum_{\substack{r=-\infty\\ r\neq 0}}^{+\infty} \frac{1}{r(r^2+s^2)} e^{\frac{2\pi i r\zeta}{\lambda}}\right).. \tag{5.61}$$

We repeat the same procedure as for equation (5.45), introducing a new variable $n = m + r$ so that we can express (5.61) as the instantaneous flux for the dilaton

$$I_\Phi(\zeta) = \kappa_\Phi \sum_{n=-\infty}^{+\infty}\left(\sum_{\substack{m=-\infty\\ m\neq\{0,n\}}}^{+\infty} \frac{1}{m(m-n)(m^2+s^2)((n-m)^2+s^2)}\right) e^{\frac{2\pi i n\zeta}{\lambda}}, \tag{5.62}$$

where $\kappa_\Phi = \frac{1024 g_{\Phi\gamma}^2 m_e^4 \gamma^8}{\pi^6 e^4 \lambda^2}$. We note here that the inner sum is more generally $m(n-m)\Phi_m\Phi_{n-m}$, which is zero for $m = 0$ and thus the result of (5.59) is not required.

We repeat the derivation carried out in equations (5.23, 5.5) to obtain the total flux for the dilaton

$$\begin{aligned}< I_\Phi >=& \kappa_\Phi\left(-\frac{\pi^2}{4s^4}\mathrm{csch}^2(\pi s) - \frac{3\pi}{4s^5}\coth(\pi s) + \frac{\pi^2}{6s^4} + \frac{1}{s^6}\right) & (5.63)\\ < N_\Phi >=& \frac{\kappa_\Phi}{m_\Phi \gamma}\sum_{n=1}^{+\infty} \frac{2s}{n^3(n^2+s^2)^2}, & (5.64)\end{aligned}$$

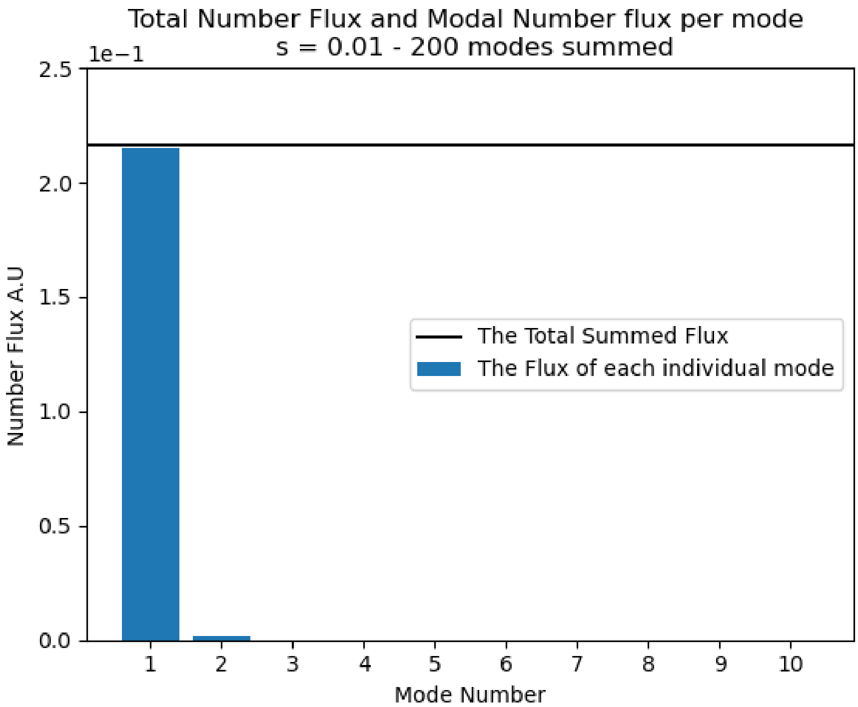

Figure 5.15: When $s = 0.01$ the first mode dominates the flux contribution comprising roughly 99% of the total flux.

where we have explicitly shown the closed form expression for the average energy flux, equation (5.63).

Similar to the axionic case, no closed form expressions exists for the flux because of its resemblance to the Riemann zeta function for odd integers. An additional point to observe between each (5.64) and (5.5) is that the initial modes comprise a far larger share of the total flux in the dilaton case, in addition to the factor n^{-2}. Practically speaking, when $s \gg n$ there is still an n^{-3} drop off in the dilaton flux, thus significantly fewer modes need to be sampled to arrive at a sound approximation for (5.64). Figures 5.15-5.17 illustrate the flux contained in the first 10 modes for three different s values.

Before proceeding to the results for the dilaton flux we highlight one more comparison between the dilaton and axion cases. For the axion, the energy in the oscillation of the plasma wave in combination with the applied magnetic field

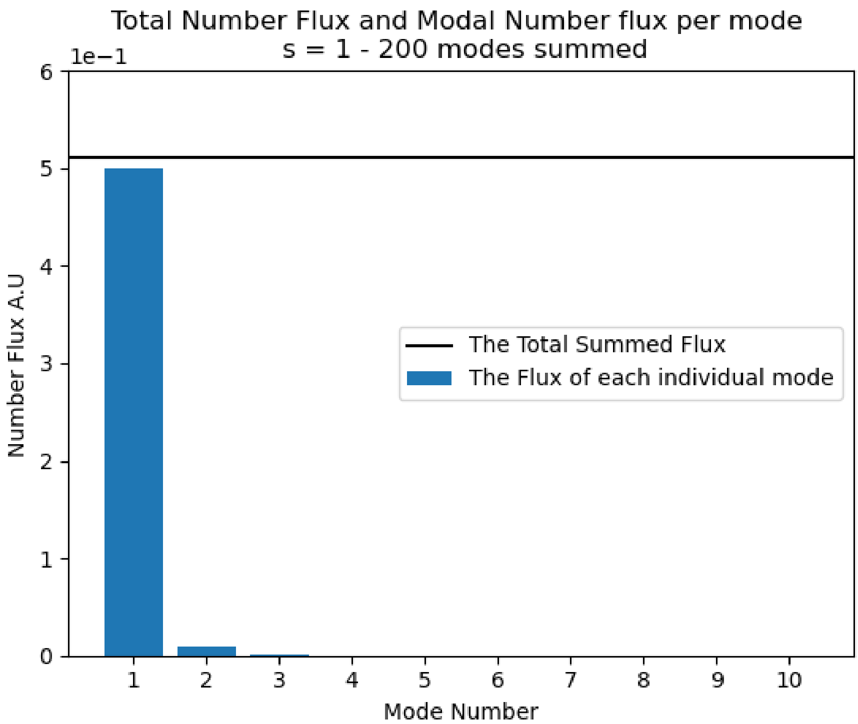

Figure 5.16: For $s = 1$ the flux contribution per mode continues to drop off rapidly as $s < n$. The first mode contributes approximately 97% of the total flux.

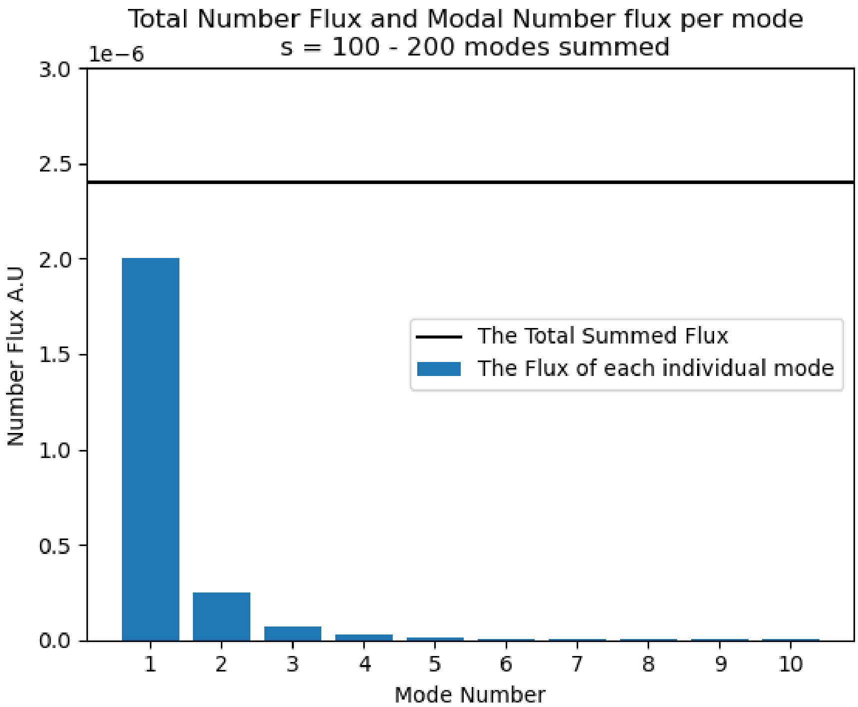

Figure 5.17: Even as s gets larger and is greater than half of the modes the contribution from each consecutive mode still drops off steeply. In this example the first contributes roughly 83% of the total flux.

provided the energy to source the axions, the $\mathbf{E} \cdot \mathbf{B}$ coupling. For the dilaton, however, there are two copies of the electric field, the $\mathbf{E}^2$ coupling. Comparing κ_φ (equation (5.17)) with κ_Φ (equation (5.63)), we find $\kappa_\varphi \to \kappa_\Phi$ for the magnetic field

$$B_0' \equiv \frac{m_e \omega_p}{\pi e} \sqrt{2\gamma}, \tag{5.65}$$

where we have used equation (C.28). Here we denote the magnetic field with a prime to differentiate it from the magnetic field in Section 5.2.1 . Comparing B_0' with the maximum electric field of a non-linear plasma wave, equation (C.25), it is clear that when $\gamma \gg 1$, it corresponds to B_0'. There is an analogue between the constant magnetic field and the maximum electric field with respect to sourcing either axions or dilatons. For a wave with a Lorentz factor of $\gamma = 100$ and plasma frequency $\omega_p = 2\pi \times 10^{13}$ rad s^{-1}, we would need a magnetic field strength of $B_0' = 1,610$ T for the field to equal the contribution of the maximum electric field towards sourcing axions. For experiments, the applied magnetic field strengths are $B_0 < 50$ T.

5.7.1 Approximate solutions by truncating the infinite series

The dilaton flux drops off at a rate of $\frac{1}{n^2}$ faster than the axion flux (5.5) and therefore is even more skewed to having the vast majority of the flux contribution arising from the first few modes. In the Figures 5.15 - 5.17 we graphically show how this distribution is concentrated into the first 10 modes for various s values. Ultimately, as the plots of Section 5.8 and numerical values of Section 5.8.1 all have maximum s values $s < 50$, we choose to truncate our infinite series at mode $n = 100$, in line with the conclusions found in Section 5.4.1.

5.8 Dependency of flux on dilaton and plasma parameters

Similar to the axion case (equation (5.33))), we illustrate the dependencies of the total flux on the dilaton mass, gamma factor and background plasma frequency more clearly

$$< N_\Phi >\propto \gamma^{\frac{17}{2}}\omega_p \sum_{n=1}^{+\infty} \frac{1}{n^3\left(n^2+\bar{\beta}\left(\frac{m_\Phi \gamma^{\frac{3}{2}}}{\omega_p}\right)^2\right)^2}. \tag{5.66}$$

As with the axion case, we have a finite flux for the dilaton in the limit $m_\Phi \to 0$, which can be seen in Figure 5.18. The dilaton flux differs from the axion flux by an extra λ^{-2} dependence because the dilaton couples to $\mathbf{E}^2$ rather than to $\mathbf{E}\cdot\mathbf{B}$, producing an additional factor of λ^{-1} in the field and hence λ^{-2} in the flux. This manifests itself in the dilaton flux, which scales almost linearly with the background plasma frequency (see Figure 5.19). Furthermore, one can clearly see that the dilaton scales more strongly with the gamma factor than the axion does.

The dilaton flux increases linearly with the background plasma frequency. An increase in the background density narrows the spacing between the density spike, which reduces the wavelength. The dilaton coupling to the square of the electric field, expressed as the derivative of ξ (equation (5.7)) introduces a proportional relationship between the dilaton flux and the plasma frequency.

Figure 5.21 shows that the flux only has a positive relation to the plasma frequency, and therefore cannot be used to fine tune the flux as is possible for the axion. However, due to the scaling of the flux with plasma frequency, a larger frequency is always desired - Figure 5.21.

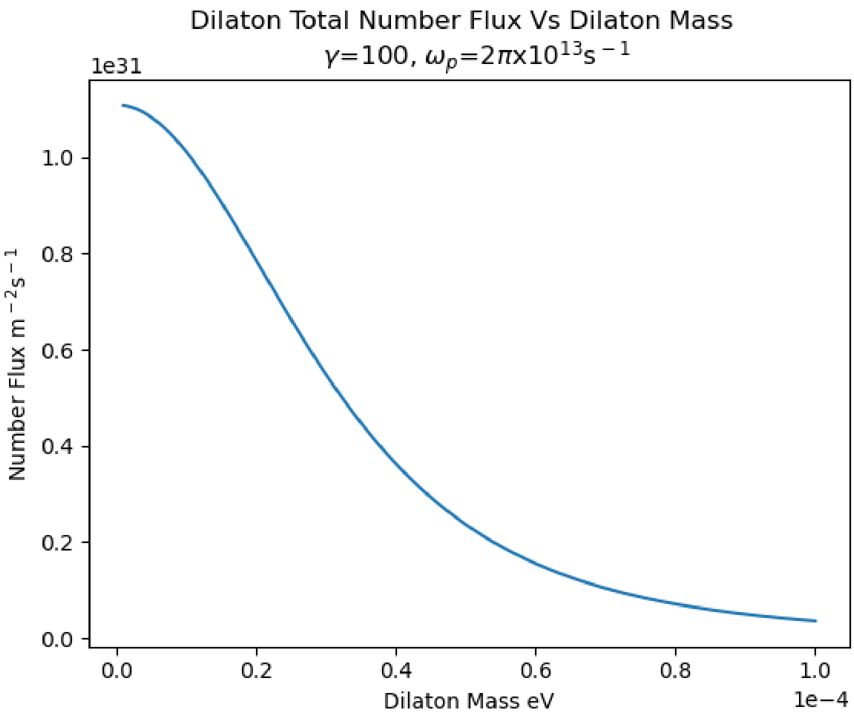

Figure 5.18: Variation in the dilaton's number flux with dilaton mass. The maximum value of the dimensionless parameter reached in this scan is $s = 2.18$.

5.8.1 Numerical dilaton flux estimates for idealised experiments

The search for dilaton particles is not as widespread as for axions. Rather than comparing fluxes of existing experiments with the expected flux of this work we instead calculate the dilaton flux using idealized experimental parameters. We confine ourselves to a mass coupling parameter space that has not yet been excluded by the bounds placed on dilatons from OSQAR [53], $m_\Phi < 200\mu\text{eV}$ for $g_{\Phi\gamma} < 3.2 \times 10^{-8}\text{GeV}^{-1}$.

We calculate the dilaton flux using equation (5.64) for 100 modes summed to be $< N_\Phi >= 8.43 \times 10^{46}\ \text{m}^{-2}\text{s}^{-1}$, where the following parameters have been used: $m_\Phi = 20\mu$ eV, $g_{\Phi\gamma} = 1 \times 10^{-8}$ GeV^{-1}, $\omega_p = 2\pi \times 10^{14}$ rad s^{-1}, $\gamma = 1000$, 43.52. This larger value arises because the dilaton flux grows with higher powers of the

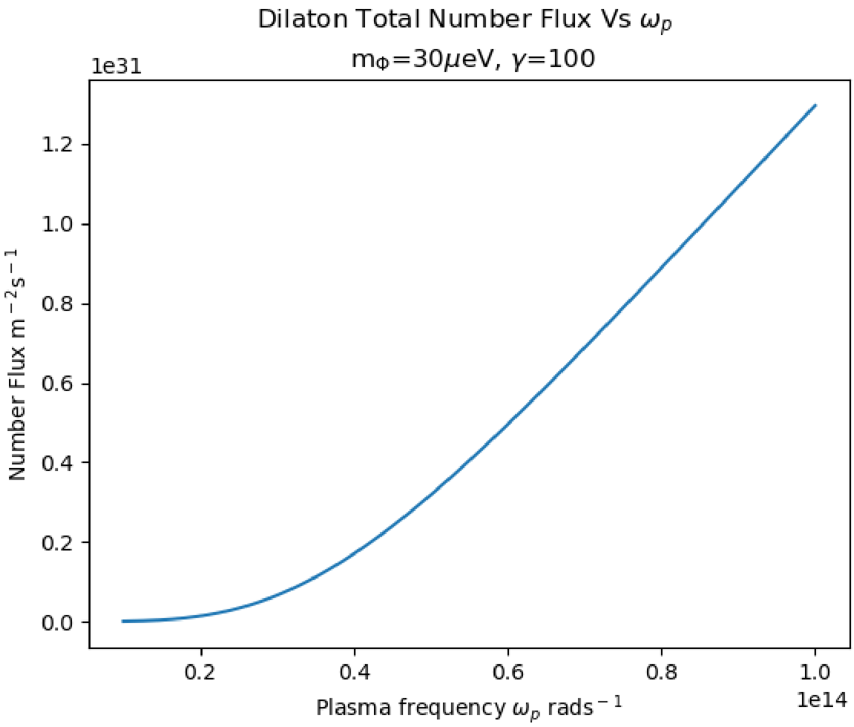

Figure 5.19: The total dilaton number flux for increasing plasma frequency. The maximum value of the dimensionless parameter reached in this scan is $s = 4.1$

plasma-wave amplitude and Lorentz factor than the axion flux.

5.9 Chapter conclusion

Plasmas are promising laboratory sources for axion and dilaton production because they can sustain very large electric fields and offer a tuneable dispersion. In this chapter we derived the spectral distribution of the produced flux for axions and dilatons sourced by a strongly driven, longitudinally magnetised 1-D plasma wave. We have shown that the flux is substantial for laboratory experiments with a predicted axion flux on the order of $N_\varphi \sim 10^{34}$ m^{-2}s^{-1} (taking $g_{\varphi\gamma} = 0.66 \times 10^{-10}$ GeV^{-1}) for experimentally realistic, optimised parameter choices. Our analysis showed that the flux is concentrated in the first few modes and the flux is peaked for $s = 0.59$, $s = \frac{2\sqrt{2}}{\pi}\frac{m_\varphi \gamma^{\frac{3}{2}}}{\omega_p}$, and can be fine-tuned by ad-

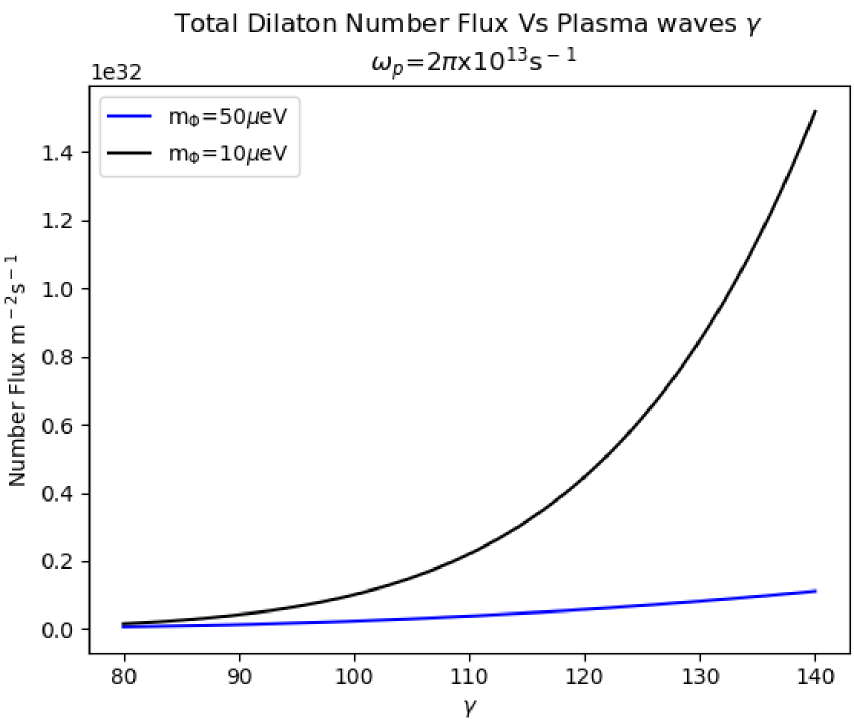

Figure 5.20: The total dilaton flux for an increasing γ. Plots for two different dilaton masses are shown. The maximum value of the dimensionless parameter reached in this scan is $s = 1.80$ (black curve) and $s = 0.36$ (blue curve).

justing the plasma frequency. Compared with the work of Burton and Noble [77], our derivation includes the full spectral information and has a different dependence of the flux on plasma and axion parameters. The approach presented here removes approximations made in [77] and gives an exact spectral prediction that can be applied to the design of an experiment.

Although this method of production depends on the repetition rate of the system[12] (we have calculated the flux per oscillation) the significant flux that can be achieved merits further analysis, especially given the likely advances in laser plasma technologies.

Future work should focus on reducing the modelling approximations in the

[12]For a laser driven plasma, the laser repetition rate and the time for the plasma to be replenished will affect the actual flux.

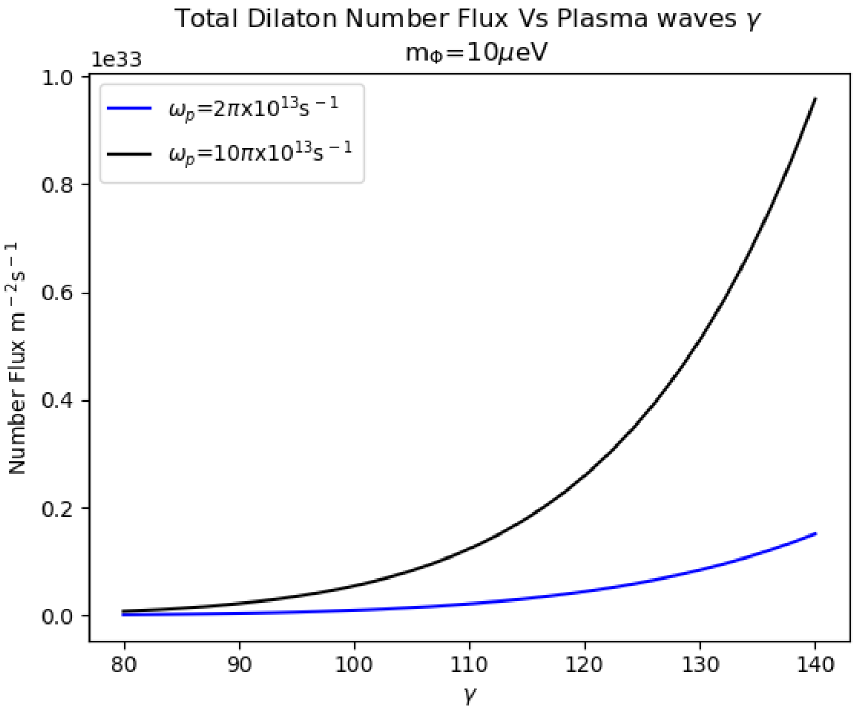

Figure 5.21: The total dilaton flux for an increasing plasma frequency. Plots for two different frequencies are shown. The maximum value of the dimensionless parameter reached in this scan is $s = 0.36$ (black curve) and $s = 0.07$ (blue curve).

predicted flux for realistic experimental parameters. This can be achieved by extending our model to 2-D and performing particle-in-cell (PIC) simulations that include a finite temperature for the plasma.

Chapter 6

Axion Fermionic Coupling

6.1 Axion fermionic coupling

In this chapter we turn our attention to axion–fermion coupling, introduced in Sections 2.2 and 3. The topic has attracted less interest than axion–photon coupling. As with photonic couplings, many bounds on the fermionic coupling follow from astrophysical arguments based on stellar cooling (axion emission opens additional dark energy-loss channels that would noticeably alter stellar evolution if the coupling were too large). In red-giant stars the axion–photon coupling is suppressed, so axion emission is dominated by fermionic processes. Therefore, observations of red-giant cooling can be used to derive upper limits on the axion–fermion coupling. From these considerations one finds $g_{\varphi e} < 1.3 \times 10^{-13}$ [47][1]. Additionally, bounds have been derived from white dwarfs, globular clusters, magnetars and other star formations [47, 84]. These limits are obtained by adding an axion cooling term to standard stellar-evolution models and requiring that the modified models remain consistent with observed luminosities, lifetimes or cool-

[1] Here we use the symbol e to represent the coupling to the electron. Later in this work we will use the symbol Ψ indicating the coupling to a Dirac field. Additionally, one may notice that this coupling is dimensionless, which arises because the Dirac field conventionally has dimensions of $\left[L^{-\frac{3}{2}}\right]$ to balance the free Dirac Lagrangian.

ing rates; the allowed mismatch between model and observation then translates into an upper bound on the coupling.

It is important to test these bounds in laboratory settings, where astrophysical model dependencies such as stellar evolution are less significant. Free-electron lasers (FELs) and plasma wakefield accelerators are attractive experimental platforms because they combine large electromagnetic field strengths, tunable photon energies, and well-characterized, controllable conditions. FELs have attracted widespread use owing to their large photon numbers per pulse and wavelength tunability [85]; however, the role of the axion fermionic coupling in FEL environments is under-explored. Beam and laser-driven wakefield accelerators are similarly promising: integrating non-invasive diagnostics into existing experimental setups could allow searches for axion production without disrupting the primary experiment, avoiding the need for a purpose built facility. The previous chapter studied axion production by strongly driven plasma waves; because wakefields are driven by particle beams or lasers, it is important to assess whether the driver particles themselves could produce axions via different couplings and how that would affect experimental signatures.

To this end, we present a study detailing axion production from a high-energy electron. In the first section of this work we solve the Dirac equation for an electron in a constant magnetic field. The procedure we employ is similar to the work found in [86]. In Section 6.4 we study the axion Klein-Gordon equation with a pseudoscalar contraction of the Dirac field as its source, solving it via a Greens function. In Sections 6.5 and 6.6 we investigate solving for the transverse and longitudinal parts of the axion field. In Section 6.6.4 we calculate the explicit form of the energy flux, and we analyse its dependence on the axion mass and electron energy in Section 6.7. Lastly, in Section 6.8, we repeat this analysis for the dilaton, the scalar equivalent of the axion.

6.2 The Dirac field of an electron in a constant magnetic field

In this section we derive the Dirac field of a single electron in a constant magnetic field. In later sections we will consider an electron bunch by modelling it on the solution of a single electron and then scaling up the result to a bunch of a given charge.

The Dirac equation for a particle with charge e and mass m_e can be written as

$$(i\gamma^{\mu}\partial_{\mu} + e\gamma^{\mu}A_{\mu} - m_e)\,\psi = 0, \tag{6.1}$$

where ψ is the Dirac field, $A^{\mu} = (A_0, \mathbf{A})$ the electromagnetic potential, and γ^{μ} the gamma matrices[2] in the Dirac representation.

As this work involves a constant magnetic field in the direction of propagation of the electron, we can make an immediate simplification. We describe the magnetic field as $\boldsymbol{B} = \hat{\mathbf{z}}B_0$, $\boldsymbol{A} = (0, xB_0, 0)$[3]. As the potential is a function of x we can express the Dirac field as a plane wave in all coordinates except x, multiplied by a spinor that depends on x. Additionally, we decompose our Dirac field into two 2-component spinors

$$\psi = e^{i\left(-\omega t + p_y y + p_{||} z\right)} \begin{pmatrix} \Theta(x) \\ \chi(x) \end{pmatrix}, \tag{6.2}$$

where we have re-labelled the z component to indicate that is is parallel to the electron propagation.

[2]See appendix Section D.1 for an explicit form of the gamma matrices.

[3]There are several options for this, such as $\mathbf{A} = (-yB_0, 0, 0)$, or a combination of A_x and A_y.

Due to the assumptions on the geometry we can expand the Dirac equation into two coupled equations

$$(\omega - m_e)\,\Theta = \big(i\sigma_1 d_x - p_y\sigma_2 - p_{||}\sigma_3 - eA_y\sigma_2\big)\,\chi \tag{6.3}$$

$$(\omega + m_e)\,\chi = \big(i\sigma_1 d_x - p_y\sigma_2 - p_{||}\sigma_3 - eA_y\sigma_2\big)\,\Theta. \tag{6.4}$$

The Pauli matrices are represented by σ_k, $k = 1, 2, 3$ and in the Dirac basis the gamma matrices can be expressed as a matrix with Pauli matrices as its elements

$$\gamma^k = \begin{pmatrix} 0 & \sigma^k \\ -\sigma^k & 0 \end{pmatrix} \tag{6.5}$$

and γ^0 is

$$\gamma^0 = \begin{pmatrix} 1 & 0 & 0 & 0 \\ 0 & 1 & 0 & 0 \\ 0 & 0 & -1 & 0 \\ 0 & 0 & 0 & -1 \end{pmatrix}. \tag{6.6}$$

We can eliminate χ to obtain a second-order equation in Θ

$$\left(\omega^2 - m_e^2\right)\Theta = \left[-d_x^2 + p_y^2 + p_{||}^2 + e^2 B_0^2 x^2 + 2eB_0 p_y x + eB_0\sigma_3\right]\Theta. \tag{6.7}$$

One can solve equation (6.7) by recasting it in the form of a quantum harmonic oscillator equation

$$\frac{d^2\Theta(\bar{x})}{d\bar{x}^2} + \left(\frac{\Omega^2}{eB_0} - \bar{x}^2\right)\Theta(\bar{x}) = 0, \tag{6.8}$$

where

$$\bar{x} =\sqrt{eB_0}\left(x + \frac{p_y}{eB_0}\right) \tag{6.9}$$

$$\Omega^2 =\omega^2 - m^2 - p_{||}^2 - eB_0 s \tag{6.10}$$

$$s = \pm 1. \tag{6.11}$$

See Appendix Section D.2 for a full derivation.

The QHO equation has solutions given by Hermite polynomials

$$\Theta_N(\bar{x}) = H_N(\bar{x})e^{-\frac{\bar{x}^2}{2}}, \tag{6.12}$$

where Θ_N is a Gaussian Hermite polynomial and H_N is a Hermite polynomial. The order of the Hermite polynomial then refers to the transverse mode of Θ_N. These modes are a result of the magnetic field causing a gyration motion of the electrons as they propagate. The field Θ_N will have quantized (Landau) energy levels given by

$$\omega^2 = m_e^2 + p_{||}^2 + eB_0 s + eB_0\left(2N+1\right). \tag{6.13}$$

This originates from the Hermite equation (6.8), which only has solutions provided $\Omega^2 = eB_0(2N+1)$. We note that Θ is a two-component spinor, with spin up/down given by $s = \pm 1$. One can see that there is a degeneracy in equation (6.13). Labelling consecutive states as $N = n-1$ with $s = 1$ and $N = n$ with $s = -1$, the degeneracy manifests itself more obviously and we can express equation (6.13) in a more compact form

$$\text{n}^{th}\text{ state}\quad \omega_n^2 = m_e^2 + p_{||}^2 + 2neB_0. \tag{6.14}$$

In the ground state, the degeneracy is broken because of the presence of the magnetic field, and therefore only the spin down state exists in the ground state. The two independent solutions for Θ corresponding to the spin up and down states are

$$\Theta_{n+} = \begin{pmatrix} \tilde{\Theta}_{n-1} \\ 0 \end{pmatrix}, \quad \Theta_{n-} = \begin{pmatrix} 0 \\ \tilde{\Theta}_{n} \end{pmatrix} \tag{6.15}$$

with the Dirac field expressed as

$$\psi_n = e^{i\theta_n} \begin{pmatrix} \Theta \\ \chi \end{pmatrix}, \tag{6.16}$$

where $\theta_n = \left(-\omega_n t + p_y y + p_{||} z\right)$ and $\tilde{\Theta}_{-1} \equiv 0$.

The conjugate Fourier variables, $p_y, p_{||}$ are, in principle, continuous variables. In calculating currents, we take the Dirac field to be a superposition of different $p_{||}$. However, for simplicity we keep p_y fixed.

To derive the full positive energy solutions for ψ, the two lower components must be determined. From equation (6.4) we have

$$\chi = \frac{1}{(\omega_n + m_e)} \begin{pmatrix} -p_z & i\sqrt{eB_0}\left(\partial_{\bar{x}} + \bar{x}\right) \\ i\sqrt{eB_0}\left(\partial_{\bar{x}} - \bar{x}\right) & p_z \end{pmatrix} \Theta, \tag{6.17}$$

where we have used (6.9).

For Gaussian Hermite polynomials, of the form given by equation (6.12), the following recursion relations are satisfied

$$\Theta_n' = \sqrt{\frac{n}{2}}\Theta_{n-1} - \sqrt{\frac{n+1}{2}}\Theta_{n+1} \tag{6.18}$$

$$x\Theta_n = \sqrt{\frac{n}{2}}\Theta_{n-1} + \sqrt{\frac{n+1}{2}}\Theta_{n+1}. \tag{6.19}$$

Applying these recursion relations to equation (6.17) for the spin up and down solution, one can show that the positive energy solutions to the Dirac equation are

$$U_{n+} \equiv \begin{pmatrix} \tilde{\Theta}_{n-1}(\bar{x}) \\ 0 \\ -\frac{p_{||}}{(\omega_n+m_e)}\tilde{\Theta}_{n-1}(\bar{x}) \\ -i\frac{\sqrt{2neB_0}}{(\omega_n+m_e)}\tilde{\Theta}_n(\bar{x}). \end{pmatrix} e^{i\theta_n}, \quad U_{n-} \equiv \begin{pmatrix} 0 \\ \tilde{\Theta}_n(\bar{x}) \\ i\frac{\sqrt{2neB_0}}{(\omega_n+m_e)}\tilde{\Theta}_{n-1}(\bar{x}) \\ \frac{p_{||}}{(\omega_n+m_e)}\tilde{\Theta}_n(\bar{x}). \end{pmatrix} e^{i\theta_n}. \tag{6.20}$$

6.3 The source of the axion field

The axion Klein-Gordon equation with a fermionic source was shown in Chapter 3 but we list it again here as a reminder

$$\left(\Box + m_\varphi^2\right)\varphi = -ig_{\varphi\Psi}\bar{\psi}\gamma^5\psi, \tag{6.21}$$

where γ^5 is defined in equation (D.3) in Appendix section D.

The pseudoscalar and scalar contractions for the Dirac field $\psi_{mn\pm} = \alpha(m)U_{m+} + \beta(n)U_{n-}$ are

$$\bar{\psi}_{mn\pm}\gamma^5\psi_{mn\pm} = i\sqrt{eB_0}\left(\alpha^*\beta e^{i\theta_{nm}} + \beta^*\alpha e^{i\theta_{mn}}\right)\left(\frac{\sqrt{2n}\tilde{\Theta}_{n-1}\tilde{\Theta}_{m-1}}{(\omega_n+m_e)} - \frac{\sqrt{2m}\tilde{\Theta}_n\tilde{\Theta}_m}{(\omega_m+m_e)}\right), \tag{6.22}$$

$$\begin{aligned}\bar{\psi}_{mn\pm}\psi_{mn\pm} =&\beta^2\tilde{\Theta}_n^2\left(1+\frac{p_{||n}^2}{\left(\omega_n+m_e\right)^2}\right)+\alpha^2\tilde{\Theta}_{m-1}^2\left(1+\frac{p_{||m}^2}{\left(\omega_m+m_e\right)^2}\right)\\ &+\alpha^2\tilde{\Theta}_m^2\frac{2meB_0}{\left(\omega_m+m_e\right)^2}+\beta^2\tilde{\Theta}_{n-1}^2\frac{2neB_0}{\left(\omega_n+m_e\right)^2}\\ &+\frac{i\sqrt{eB_0}\left(\alpha^*\beta-\alpha\beta^*\right)}{\left(\omega_m+m_e\right)\left(\omega_n+m_e\right)}\left(p_{||n}\sqrt{2m}\tilde{\Theta}_n\tilde{\Theta}_m e^{i\theta_{nm}}-p_{||m}\sqrt{2n}\tilde{\Theta}_{n-1}\tilde{\Theta}_{m-1}e^{i\theta_{mn}}\right),\end{aligned} \tag{6.23}$$

where $e^{i\theta_{nm}} = e^{i(\theta_n-\theta_m)}$. In later sections we will simplify and make further assumptions to these contractions. Despite this, in our later calculations of these terms (see equations (6.59) and (6.61)) one can still see the underlying structure present in these more general calculations.

The terms α and β in the Dirac fields are the amplitude of the states that depend on the mode number and can be related to the total charge[4]. The Dirac field for the electron is modelled as a superposition of two spin states as the contraction results in quadratic terms. In this way, superpositions involving more states can be derived from the general solution involving two spin states. In an analogous way, the contractions involve Gaussian Hermite polynomials that can be modelled as Gaussian monomials, with the solutions combined appropriately to yield the full solution given by the full Gaussian Hermite polynomial source.

6.4 Analysing the axion-Klein-Gordon equation

We solve the axion field for an arbitrary single mode and sum together the relevant modes to obtain the solution for the full field. We revisit the axion equation[5] of motion from Section 3 for a fermionic source,

[4]The total charge is defined as $Q = e\int\bar{\Psi}\gamma^0\Psi$, where we have a volume integral and e is the unit charge.

[5]In this section we discuss everything in terms of the axion. However, it is equally applicable to the dilaton. One must ensure to change the mass $m_\varphi \to m_\Phi$ accordingly.

$$\left(\partial_\mu \partial^\mu + m_\varphi^2\right)\varphi = -i g_{\varphi\psi} \bar{\psi}\gamma^5\psi. \tag{6.24}$$

Instead of solving for the full source shown above, we solve for a source comprising a Gaussian monomial that depends on the transverse coordinate $\bar{x}$. We add together several solutions for different monomial powers to obtain the full solution. The axion source is given by squared Gaussian Hermite polynomials. Our differential equation becomes

$$\left(\nabla_{\bar{x}}^2 + \omega'^2\right)\varphi_p(\bar{x}) = \mathcal{J}(\bar{x})_p \tag{6.25}$$

$$\mathcal{J}(\bar{x})_p = \frac{\bar{x}^p e^{-\bar{x}^2}}{eB_0}, \tag{6.26}$$

where we use the coordinate $\bar{x}$ and where

$$\omega'^2 = \frac{\Delta\omega^2 - \Delta p_{||}^2 - m_\varphi^2}{eB_0}. \tag{6.27}$$

The Δ's in (6.27) originate from the fact that the plane wave dependency in coordinates (y, z and t) comes from a phase difference, as can be seen from equation (6.22).

Instead of solving equation (6.25) directly, we solve an equivalent differential equation for a Green's function $G(\bar{x}, \bar{x}')$, which, when integrated over the source, will yield the axion field

$$\left(\nabla_{\bar{x}}^2 + \omega'^2\right) G(\bar{x}, \bar{x}') = \delta\left(\bar{x} - \bar{x}'\right) \tag{6.28}$$

$$\varphi_p(\bar{x}) = \int_{-\infty}^{\infty} d\bar{x}' G(\bar{x}, \bar{x}')\mathcal{J}_p(\bar{x}'). \tag{6.29}$$

Note that the source is now in the primed coordinate as this will be integrated leaving just the un-primed coordinate in the axion field (an axion mode).

The Green's function is not defined uniquely without the use of boundary/initial conditions, of which we require two for a second-order equation. Explicitly, taking our phase difference to be θ_{nm} we have

$$\omega' = \sqrt{\frac{(\omega_m - \omega_n)^2 - (p_n - p_m)^2 - m_\varphi^2}{eB_0}}. \tag{6.30}$$

When explicitly calculating the Dirac field contraction that sources the axion field in Section 6.6.1, we will assume the electron momentum has a gaussian-like distribution, tightly peaked around $p = \mathcal{E}_0$. As we have two contributions to the momentum in the above equation, we equate one momentum to the peaked value and one to the peaked value plus one standard deviation $p_m = \mathcal{E}_0, \quad p_n = \mathcal{E}_0 + \delta$. As the momentum is tightly peaked we can expand the frequency of one component $(\omega_n(p_n))$ about the peak value

$$\omega_n(p_n) = \sqrt{m_e^2 + p_n^2 + 2neB_0} \tag{6.31}$$

$$\omega_n(\mathcal{E}_0 + \delta) = \omega(\mathcal{E}_0) + \omega'(\mathcal{E}_0)\delta \tag{6.32}$$

$$= \sqrt{m_e^2 + \mathcal{E}_0^2 + 2neB_0} + \frac{\mathcal{E}_0 \delta}{\sqrt{m_e^2 + \mathcal{E}_0^2 + 2neB_0}} \tag{6.33}$$

$$\text{hence} \quad \omega' = \sqrt{\frac{-\frac{\delta^2(m_e^2 + 2neB_0)}{\left(m_e^2 + \mathcal{E}_0^2 + 2neB_0\right)} - m_\varphi^2}{eB_0}}. \tag{6.34}$$

We have the square root of negative values and can conclude that $\omega' = i\bar{\omega}$, where

$$\bar{\omega} = \sqrt{\frac{\left(m_\varphi^2 + \delta^2\right)\left(m_e^2 + 2neB_0\right) + m_\varphi^2 \mathcal{E}_0^2}{eB_0\left(m_e^2 + \mathcal{E}_0^2 + 2neB_0\right)}}. \tag{6.35}$$

Depending on the values of the parameters involved, $\bar{\omega}$ can have three distinct dependencies:

$$\bar{\omega} = \sqrt{\frac{\delta^2 m_e^2}{eB_0\mathcal{E}_0^2}} \qquad m_\varphi^2\mathcal{E}_0^2 \ll \delta^2 m_e^2 \tag{6.36}$$

$$\bar{\omega} = \sqrt{\frac{\delta^2 m_e^2 + m_\varphi^2\mathcal{E}_0^2}{eB_0\mathcal{E}_0^2}} \qquad m_\varphi^2\mathcal{E}_0^2 \approx \delta^2 m_e^2 \tag{6.37}$$

$$\bar{\omega} = \sqrt{\frac{m_\varphi^2}{eB_0}} \qquad m_\varphi^2\mathcal{E}_0^2 \gg \delta^2 m_e^2 \tag{6.38}$$

We will touch on this later in Section 6.7 when we calculate numerical results for the produced axion flux.

6.5 Calculating the axion modes using the Greens function

We now return to solving the Greens function.

$$\left(\nabla_{\bar{x}}^2 - \bar{\omega}^2\right) G(\bar{x}, \bar{x}') = \delta\left(\bar{x} - \bar{x}'\right) \tag{6.28 Revisited}$$

$$\varphi_p(\bar{x}) = \int_{-\infty}^{\infty} d\bar{x}' G(\bar{x}, \bar{x}')\mathcal{J}_p(\bar{x}') \tag{6.29 Revisited}$$

The general solution of the Green's function (6.28) away from the peak of the delta function has the following forms

$$G(\bar{x}, \bar{x}') = \begin{cases} G_L(\bar{x}, \bar{x}') = A(\bar{x}')e^{\bar{\omega}\bar{x}} + B(\bar{x}')e^{-\bar{\omega}\bar{x}} & \bar{x} < \bar{x}' \\ G_R(\bar{x}, \bar{x}') = C(\bar{x}')e^{\bar{\omega}\bar{x}} + D(\bar{x}')e^{-\bar{\omega}\bar{x}} & \bar{x} > \bar{x}' \end{cases} . \tag{6.39}$$

We can eliminate B and C by insisting that $G(\bar{x}, \bar{x}') \to 0$ as $\bar{x} \to \pm\infty$[6] and subsequently express A and D in terms of each other by insisting that the Green's

[6]This similarly means that the axion field tends to zero at these points.

function is continuous at $\bar{x} = \bar{x}'$. Applying these, the Green's function can be shown to be

$$G(\bar{x}, \bar{x}') = \begin{cases} G_L(\bar{x}, \bar{x}') = -\frac{e^{\bar{\omega}(\bar{x}-\bar{x}')}}{2\bar{\omega}} & \bar{x} < \bar{x}' \\ G_R(\bar{x}, \bar{x}') = -\frac{e^{\bar{\omega}(\bar{x}'-\bar{x})}}{2\bar{\omega}} & \bar{x} > \bar{x}' \end{cases} . \tag{6.40}$$

A more detailed derivation is given in Appendix Section D.3.

We return now to equation (6.29) and use our definition of the Green's function above to express the p^{th} axion mode as

$$\varphi_p(\bar{x}) = -\frac{1}{2\bar{\omega}} \left[\int_{-\infty}^{\bar{x}} e^{\bar{\omega}(\bar{x}'-\bar{x})} \bar{x}'^p e^{-\bar{x}'^2} \quad d\bar{x}' + \int_{\bar{x}}^{\infty} e^{\bar{\omega}(\bar{x}-\bar{x}')} \bar{x}'^p e^{-\bar{x}'^2} \quad d\bar{x}' \right]. \tag{6.41}$$

The presence of exponential terms in equation (6.41) means that integrating by parts will lead to recursive results. We show that both integrals present in equation (6.41) can be expressed in terms of the same recursion relation. By extension, this allows the transverse axion mode of order p to be expressed using a single recursion relation. Once we have demonstrated this, we will explicitly calculate the seeds of this recursion such that each subsequent term can be explicitly calculated. Ultimately, we will determine the first four axion modes that allows the total axion field to be calculated analytically, assuming an upper mode limit with respect to the Hermite polynomials of $n = 2$.

We label the integrals in equation (6.41) as

$$I_p(\bar{x}) = \int_{-\infty}^{\bar{x}} e^{\bar{\omega}\bar{x}'} \bar{x}'^p e^{-\bar{x}'^2} \quad d\bar{x}' \tag{6.42}$$

$$L_p(\bar{x}) = \int_{\bar{x}}^{\infty} e^{-\bar{\omega}\bar{x}'} \bar{x}'^p e^{-\bar{x}'^2} \quad d\bar{x}', \tag{6.43}$$

where the integrands are denoted as $I_p(\bar{x}, \bar{x}')$, $L_p(\bar{x}, \bar{x}')$ respectively. Note that we have not included the factor $e^{\pm\bar{\omega}\bar{x}}$, which is constant with respect to the integral. This will be restored at the end.

Integrating $I_p(\bar{x})$ we can derive a recursion relation for it

$$I_p(\bar{x}) = \int_{-\infty}^{\bar{x}} e^{\bar{\omega}\bar{x}'}\bar{x}'^p e^{-\bar{x}'^2} \quad d\bar{x}' \tag{6.42 Revisited}$$

$$= \frac{e^{\bar{\omega}\bar{x}}\bar{x}^p e^{-\bar{x}^2}}{\bar{\omega}} - \frac{1}{\bar{\omega}}\int_{-\infty}^{\bar{x}} d\bar{x}' \left[p\bar{x}'^{p-1}e^{-\bar{x}'^2}e^{\bar{\omega}\bar{x}'} - 2\bar{x}'^{p+1}e^{-\bar{x}'^2}e^{\bar{\omega}\bar{x}'}\right] \tag{6.44}$$

$$= \frac{e^{\bar{\omega}\bar{x}}\bar{x}^p e^{-\bar{x}^2}}{\bar{\omega}} - \frac{p}{\bar{\omega}}I_{p-1} + \frac{2}{\bar{\omega}}I_{p+1}. \tag{6.45}$$

Applying the transformation $\bar{x}' \to -\bar{x}'$ to $L_p(\bar{x})$, we obtain the following,

$$L_p(\bar{x}) = (-1)^p \underbrace{\int_{-\infty}^{\bar{x}} e^{\bar{\omega}\bar{x}'}e^{-\bar{x}'^2}\bar{x}'^p d\bar{x}'}_{\text{This is exactly } I_p(\bar{x})} - (-1)^p \int_{-\bar{x}}^{\bar{x}} e^{\bar{\omega}\bar{x}'}e^{-\bar{x}'^2}\bar{x}'^p d\bar{x}', \tag{6.46}$$

which can be expressed as $I_p(\bar{x})$ minus a new integral.

Examining this new integral (right hand term above) we can see its integrand is exactly $I_p(\bar{x}, \bar{x}')$ and its integration limits are exactly the difference in the limits of $I_p(\bar{x})$ and $I_p(-\bar{x})$, therefore

$$\int_{-\bar{x}}^{\bar{x}} e^{\bar{\omega}\bar{x}'}e^{-\bar{x}'^2}\bar{x}'^p d\bar{x}' = I_p(\bar{x}) - I_p(-\bar{x}). \tag{6.47}$$

After implementing all of these steps substituting equations (6.47), (6.46) and (6.45) back into equation (6.41), we obtain an equation for the axion mode of order p expressed purely in terms of the integral I_p[7]

$$\varphi_p(\bar{x}) = -\frac{1}{2\bar{\omega}}\left[e^{-\bar{\omega}\bar{x}}I_p(\bar{x}) + (-1)^p e^{\bar{\omega}\bar{x}}I_p(-\bar{x})\right]. \tag{6.48}$$

[7]Unfortunately a recursion relation purely in terms of φ_p could not be found.

To fully utilize this equation, we must first determine the explicit form of I_0 and I_1 such that we can exploit the recursive nature of equation (6.45). To integrate equation (6.42) for $p = 0, 1$ we compute the variable change, $t = \bar{x}' - \frac{\bar{\omega}}{2}$ such that we can obtain a Gaussian term in the integrand, allowing integration by parts

$$\int_{-\infty}^{x} e^{\bar{\omega}\bar{x}'}\bar{x}'^{p}e^{-\bar{x}'^{2}} \quad d\bar{x}' = e^{\frac{\bar{\omega}^2}{4}} \int_{-\infty}^{\bar{x}-\frac{\bar{\omega}}{2}} e^{-t^2}\left(t + \frac{\bar{\omega}}{2}\right)^{p} dt. \tag{6.49}$$

We utilize the following integral definition

$$\int_{x}^{\infty} e^{-t^2} dt = \frac{\sqrt{\pi}}{2}\left(1 - \operatorname{erf}(x)\right), \tag{6.50}$$

which, when combined with the standard Gaussian integral over the range $(-\infty, \infty)$, can be used to determine any Gaussian integral over some subspace of $(-\infty, \infty)$. Here, erf is the error function.

The first value in the series, I_0, follows directly from the above equations,

$$I_0 = \frac{\sqrt{\pi}}{2}\left(1 + \operatorname{erf}\left(\bar{x} - \frac{\bar{\omega}}{2}\right)\right) e^{\frac{\bar{\omega}^2}{4}}. \tag{6.51}$$

For $p = 1$ we have,

$$I_1(\bar{x}) = e^{\frac{\omega^2}{4}} \int_{-\infty}^{\bar{x}-\frac{\bar{\omega}}{2}} e^{-t^2}\left(t + \frac{\bar{\omega}}{2}\right) dt \tag{6.52}$$

$$I_1(\bar{x}) = e^{\frac{\omega^2}{4}} \left[\left|\frac{\sqrt{\pi}}{2}\left(t + \frac{\bar{\omega}}{2}\right)\left(1 + \operatorname{erf}(t)\right)\right|_{-\infty}^{\bar{x}-\frac{\bar{\omega}}{2}} - \frac{\sqrt{\pi}}{2}\int_{-\infty}^{\bar{x}-\frac{\bar{\omega}}{2}} \left(1 + \operatorname{erf}(t)\right) dt\right], \tag{6.53}$$

$$I_1 = I_0\frac{\bar{\omega}}{2} - \frac{e^{-\bar{x}(\bar{x}-\bar{\omega})}}{2}. \tag{6.54}$$

In the Appendix Section D.5 we use the recursive nature of equation (6.42) to evaluate the first four transverse modes for the axion field, using equation (6.48).

6.6 Calculating the axion field and axion flux

We can now progress to calculating the full solution of the axion field sourced by an electron propagating parallel to a magnetic field. We return to the pseudoscalar and scalar contractions (6.22 and 6.23), this time modelling them with a gaussian-like spread in the longitudinal momentum direction.

6.6.1 Determining the pseudoscalar and scalar contractions

In this subsection, we calculate the pseudoscalar and scalar contraction from the following Dirac field

$$\Psi = \alpha(n)\int_{-\infty}^{\infty} dp A(p)\psi \tag{6.55}$$

$$\psi = (U_{n+} + U_{n-}) \tag{6.56}$$

$$= \begin{pmatrix} \tilde{\Theta}_{n-1} \\ \tilde{\Theta}_{n} \\ \tilde{\Theta}_{n-1}\left(\frac{i\sqrt{2neB_0}-p}{\omega_n+m_e}\right) \\ \tilde{\Theta}_{n}\left(\frac{p-i\sqrt{2neB_0}}{\omega_n+m_e}\right) \end{pmatrix} e^{i(pz-\omega_n t)}, \tag{6.57}$$

where $U_{n\pm}$ are defined in equation (6.20), $\alpha(n)$ is the amplitude of the field and $A(p)$ is a modulation that we apply in the longitudinal direction.

We now represent the Dirac field with an upper case Ψ to distinguish it from the unmodulated Dirac field. Note that the amplitude α has dimensions $\left[E^{-1}T^{1}L^{-\frac{3}{2}}\right]$, such that the field has dimensions $[\Psi] = \left[L^{-\frac{3}{2}}\right]$. This ensures the Dirac Lagrangian has the correct dimensionality ($[\mathcal{L}_{\text{Dirac}}] = [EL^{-3}]$).

Given the Dirac field (6.55) we can make the following contractions.

The pseudoscalar contraction of Ψ, where $\Psi = (u_1, u_2, u_3, u_4)^T$, is

$$\bar{\Psi}\gamma^5\Psi = -u_3^* u_1 - u_4^* u_2 + u_1^* u_3 + u_2^* u_4 \tag{6.58}$$

$$\bar{\Psi}\gamma^5\Psi = |\alpha|^2 \left(\tilde{\Theta}_{n-1}^2 - \tilde{\Theta}_n^2\right) \int_{-\infty}^{\infty} dp dp' A(p) A(p') e^{i\theta_{pp'}} \left(\frac{i\sqrt{2neB_0} - p}{(\omega_p + m_e)} + \frac{i\sqrt{2neB_0} + p'}{(\omega_p' + m_e)}\right), \tag{6.59}$$

where γ^5 is defined in Appendix section D.1, equation (D.3). As the integrals are over momentum, the notation of p and p' has been used to keep track of where each instance of p originated (Ψ or $\bar{\Psi}$). The phase is defined as $\theta_{pp'} = z(p - p') + t(\omega_{p'} - \omega_p)$.

A crucial point in this derivation is noting that the Hermite polynomials in equation (6.59) are outside the momentum integral. This can be done, as we have demonstrated, in Section 6.4, that the parameter $\bar{\omega}$ is independent of any momentum variable when in the regime where equation (6.38) holds. Outside of this regime, equations (6.36 and 6.37), we assume this is a good approximation due to the electron's narrow energy spread.

Similarly, the scalar contraction (for Ψ defined as above) takes the form

$$\bar{\Psi}\Psi = u_1^* u_1 + u_2^* u_2 - u_3^* u_3 - u_4^* u_4 \tag{6.60}$$

$$\bar{\Psi}\Psi = |\alpha|^2 \left(\tilde{\Theta}_n^2 + \tilde{\Theta}_{n-1}^2\right) \int_{-\infty}^{\infty} dp dp' A(p) A(p') e^{i\theta_{pp'}} \left[\frac{i\sqrt{2neB_0}(p' - p)}{(\omega_p + m_e)(\omega_{p'} + m_e)} - \frac{2neB_0}{(\omega_p + m_e)(\omega_{p'} + m_e)}\right]. \tag{6.61}$$

In calculating the axion field we obtain an expression involving $|\alpha|^2$, where α shown in equation (6.55) as an amplitude of the states. This can be determined by deriving an expression for the charge of the electron bunch. The total charge is given by the volume integral over the charge density ρ, which itself is proportional to the zeroth component of the conserved current formed via contracting the Dirac field – see equations (D.7) and (D.8) in the Appendix.

6.6.2 The charge density

A conserved current can be constructed from the Dirac field (see Appendix Section D.1). Of this, the zeroth component j^0 is the charge density, which is the quantity that, experimentally, we have control over and thus can pin down the parameter α that appears in the axion field.

Using the contraction $\bar{\Psi}\gamma^0\Psi$ we can express the charge density as a double integral over the longitudinal momentum as follows,

$$\rho = e\bar{\Psi}\gamma^0\Psi \tag{6.62}$$

$$= e|\alpha|^2 \left(\tilde{\Theta}_n^2 + \tilde{\Theta}_{n-1}^2\right) \int_{-\infty}^{\infty} dp dp' A(p) A(p') e^{i\theta_{pp'}} \left[2 + \frac{i\sqrt{2neB_0}(p'-p)}{(\omega_p + m_e)(\omega_{p'} + m_e)} - \frac{2neB_0}{(\omega_p + m_e)(\omega_{p'} + m_e)}\right]. \tag{6.63}$$

We define our modulation as

$$A(p) = pe^{-\sigma_b^2(p-\mathcal{E}_0)^2}, \tag{6.64}$$

which is selected for mathematical convenience whilst still allowing for control over the momentum spread. A plot of the modulation is shown in the Appendix Section D.4. We want to model an electron bunch using our solution (for a single electron) of the Dirac field. As the Dirac field is linear we can scale up the result for the single electron by the number of electrons. The assumption of an electron 'bunch' allows us to make use of the bunch duration, which we label as σ in the applied modulation, to describe an electron bunch with a narrow energy spread. This allows us to simplify $\omega_p \approx p$.

With the definition of the modulation we can express terms within the integral as derivatives of Gaussian functions. These derivatives can then be commuted with the integral:

$$
\begin{aligned}
\rho = e|\alpha|^2 \left(\tilde{\Theta}_{n-1}^2 + \tilde{\Theta}_n^2\right) \int_{-\infty}^{\infty} dp\, dp' \Bigg[& 2p\, e^{-\sigma_b^2(p-\epsilon_0)^2} e^{ip(z-t)}\, p'\, e^{-\sigma_b^2(p'-\epsilon_0)^2} e^{-ip'(z-t)} \\
& + i\sqrt{2neB_0}\Big(p'\, e^{-\sigma_b^2(p'-\epsilon_0)^2} e^{-ip'(z-t)}\, e^{-\sigma_b^2(p-\epsilon_0)^2} e^{ip(z-t)} \\
& - p\, e^{-\sigma_b^2(p-\epsilon)^2} e^{ip(z-t)}\, e^{-\sigma_b^2(p'-\epsilon_0)^2} e^{-ip'(z-t)}\Big) \\
& - 2neB_0\, e^{-\sigma_b^2(p'-\epsilon_0)^2} e^{-ip'(z-t)}\, e^{-\sigma_b^2(p-\epsilon_0)^2} e^{ip(z-t)} \Bigg]
\end{aligned} \tag{6.65}
$$

$$
\begin{aligned}
= e|\alpha|^2 \left(\tilde{\Theta}_{n-1}^2 + \tilde{\Theta}_n^2\right) \int_{-\infty}^{\infty} dp\, dp' \Bigg[& -2i\, \partial_z \left(e^{-\sigma_b^2(p-\epsilon_0)^2} e^{ip(z-t)}\right)\, i\, \partial_z \left(e^{-\sigma_b^2(p'-\epsilon_0)^2} e^{-ip'(z-t)}\right) \\
& + i\sqrt{2neB_0}\Big(i\, \partial_z \left(e^{-\sigma_b^2(p'-\epsilon_0)^2} e^{-ip'(z-t)}\right)\, e^{-\sigma_b^2(p-\epsilon_0)^2} e^{ip(z-t)} \\
& + i\, \partial_z \left(e^{-\sigma_b^2(p-\epsilon_0)^2} e^{ip(z-t)}\right)\, e^{-\sigma_b^2(p'-\epsilon_0)^2} e^{-ip'(z-t)}\Big) \\
& - 2neB_0\, e^{-\sigma_b^2(p'-\epsilon_0)^2} e^{-ip'(z-t)}\, e^{-\sigma_b^2(p-\epsilon_0)^2} e^{ip(z-t)} \Bigg]
\end{aligned} \tag{6.66}
$$

$$
\begin{aligned}
= e|\alpha|^2 \left(\tilde{\Theta}_{n-1}^2 + \tilde{\Theta}_n^2\right) \frac{\pi}{\sigma_b^2} \Bigg[& 2\, \partial_z \left(e^{i\epsilon_0(z-t)} e^{-\frac{(z-t)^2}{4\sigma_b^2}}\right)\, \partial_z \left(e^{-i\epsilon_0(z-t)} e^{-\frac{(z-t)^2}{4\sigma_b^2}}\right) \\
& + i\sqrt{2neB_0}\Big(i\, \partial_z \left(e^{-i\epsilon_0(z-t)} e^{-\frac{(z-t)^2}{4\sigma_b^2}}\right)\, e^{i\epsilon_0(z-t)} e^{-\frac{(z-t)^2}{4\sigma_b^2}} \\
& + i\, \partial_z \left(e^{i\epsilon_0(z-t)} e^{-\frac{(z-t)^2}{4\sigma_b^2}}\right)\, e^{-i\epsilon_0(z-t)} e^{-\frac{(z-t)^2}{4\sigma_b^2}}\Big) \\
& - 2neB_0\, e^{-\frac{(z-t)^2}{2\sigma_b^2}} \Bigg],
\end{aligned} \tag{6.67}
$$

$$
\rho = e\alpha^2 \frac{\pi}{\sigma_b^2} \left(\tilde{\Theta}_{n-1}^2 + \tilde{\Theta}_n^2\right) e^{-\frac{(z-t)^2}{2\sigma_b^2}} \left(2\mathcal{E}_0^2 - 2neB_0 + \sqrt{2neB_0}\frac{(z-t)}{\sigma_b^2} + \frac{(z-t)^2}{2\sigma_b^4}\right). \tag{6.68}
$$

At this stage we must specify the Hermite polynomial modes in order to proceed. Generalized expressions for the product of Hermite polynomials in terms of new Hermite polynomials do exist. However, they are complicated and unwieldy. We choose to study the lowest mode (excluding the ground state) $n = 1$, such that

$$\rho^{(1)} = e\alpha^2 \frac{\pi}{\sigma_b^2} \left(4\bar{x}^2 + 1\right) e^{-\bar{x}^2} e^{-\frac{(z-t)^2}{2\sigma_b^2}} \left(2\mathcal{E}_0^2 + 2eB_0 - \sqrt{2eB_0}\frac{(z-t)}{\sigma_b^2} + \frac{(z-t)^2}{2\sigma_b^4}\right). \tag{6.69}$$

To determine the parameter α, we must first state what the total charge in the electron beam will be. We can then take the volume integral over ρ, equating it with the charge to determine α. For typical experiments, a charge of the order of 1 nC is reasonable – this value will only act to scale the result, thus determining α for a different charge is straightforward. We begin by making a coordinate change. We should clarify that this is an approximation to allow us to derive an analytical expression for the charge density. We change to cylindrical coordinates by assuming that, as we have planar symmetry in the **y** axis (there is constant momentum here), we can consider a circle in the **x-y** plane given by radius $\bar{x}$ (we centre our origin at $\bar{x} = 0$). If we did not do this, and integrated over the **y** axis we would get an infinite term due to the symmetric momentum in **y**. The volume integral can be expressed as $dV = rdrd\theta dz = \frac{\bar{x}}{eB_0} d\bar{x} d\theta dz$, in cylindrical coordinates.

The volume integral of equation (6.69) then yields,

$$\int_V \rho^{(1)} dV = \int_0^\infty \int_0^{2\pi} \int_{-\infty}^\infty \frac{\bar{x}}{eB_0} \rho^{(1)} \quad d\bar{x} d\theta dz \tag{6.70}$$

$$= \frac{5\alpha^2\pi^2}{B_0\sigma_b^2} \int_{-\infty}^\infty dz e^{-\frac{(z-t)^2}{2\sigma_b^2}} \left(2\mathcal{E}_0^2 - 2eB_0 + \sqrt{2eB_0}\frac{(z-t)}{\sigma_b^2} + \frac{(z-t)^2}{2\sigma_b^4}\right) \tag{6.71}$$

$$= \frac{10\alpha^2\pi^2}{B_0} \sqrt{\frac{2\pi}{\sigma_b^2}} \left(\mathcal{E}_0^2 - eB_0 + \frac{1}{4\sigma_b^2}\right) = Q^{(1)}. \tag{6.72}$$

$$Q^{(1)} = 10\frac{\alpha^2\pi^2}{B_0}\sqrt{\frac{2\pi}{\sigma_b^2}}\left(\mathcal{E}_0^2 - eB_0 + \frac{1}{2\sigma_b^2}\right). \tag{6.73}$$

If we assume the following rough experimental values: electron energy $\mathcal{E}_0 \approx 1$ GeV, applied magnetic field $B_0 = 10$ T and an electron beam duration[8] $\sigma_b = 1$ fs, then the electron's average energy is by far the dominant factor inside the bracket in the above equation. Simplifying and rearranging for α we have

$$\alpha_1 = \sqrt{\frac{QB_0\sigma_b}{10\pi^2\sqrt{2\pi}\mathcal{E}_0^2}}, \tag{6.74}$$

where σ_b is the duration of the electron beam and $\mathcal{E}_0$ the average energy of the electrons.

For the Hermite polynomial of order $n = 2$ the result is

$$\alpha_2 = \sqrt{\frac{QB_0\sigma_b}{48\pi^2\sqrt{2\pi}\mathcal{E}_0^2}}. \tag{6.75}$$

6.6.3 The axion field

We can now return to the contraction shown in equation (6.59), fully calculating it to determine the source of the axion field. The momentum integrals that come from the contractions can be computed in exactly the same way as was shown in the preceding subsection, that is, expressing the factors of p and p' in the integrand as derivatives (where appropriate) and commuting them with the integral. This yields,

[8] Here we are referring to the standard deviation of the duration.

$$
\begin{aligned}
\bar{\Psi}\gamma^5\Psi =& \alpha^2 \left(\tilde{\Theta}_{n-1}^2 - \tilde{\Theta}_n^2\right) i\sqrt{2neB_0} \int_{-\infty}^{\infty} dpdp' \\
&\cdot \left[i\partial_z \left(e^{-\sigma_b^2 (p'-\mathcal{E}_0)^2} e^{-ip'(z-t)} \right) e^{-\sigma_b^2 (p-\mathcal{E}_0)^2} e^{ip(z-t)} \right. \\
&\left. - i\partial_z \left(e^{-\sigma_b^2 (p-\mathcal{E}_0)^2} e^{ip(z-t)} \right) e^{-\sigma_b^2 (p'-\mathcal{E}_0)^2} e^{-ip'(z-t)} \right] \qquad (6.76) \\
=& |\alpha_n|^2 \frac{2\pi i \mathcal{E}_0 \sqrt{2neB_0}}{\sigma_b^2} e^{-\frac{(z-t)^2}{2\sigma_b^2}} \left(\tilde{\Theta}_{n-1}^2 - \tilde{\Theta}_n^2\right). \qquad (6.77)
\end{aligned}
$$

We can see that the above result is zero for $n = 0$, as expected, because the degeneracy of the electron states is broken in the ground state due to the magnetic field. The contraction is zero as the Dirac field would represent an electron that is purely in a spin down state. This is also true for the scalar contraction.

The full equation for the axion field can now be expressed as

$$
\begin{aligned}
\varphi_n =& \frac{2\pi g_{\varphi\psi} \sqrt{2n} \alpha_n^2 \mathcal{E}_0}{\sqrt{eB_0} \sigma_b^2} e^{-\frac{(z-t)^2}{2\sigma_b^2}} \\
&\cdot \int_{-\infty}^{\infty} d\bar{x}' G(\bar{x}, \bar{x}') \left(\tilde{\Theta}_n^2 - \tilde{\Theta}_{n-1}^2\right). \qquad (6.78)
\end{aligned}
$$

Finally, to solve the transverse integral, we can utilise the results of Section 6.5, where we worked out the general solution for the axion modes – equation (6.48). Unfortunately, we cannot show an explicit general solution for the axion field, and need to specify the mode number of the electrons that source the axions. We will analytically study the lowest two non-trivial modes. In the preceding subsection we have shown the form α takes given this choice of mode. Below, we show the relevant axion modes that are needed to comprise the transverse part of the full field

$$\left(\tilde{\Theta}_n^2 - \tilde{\Theta}_{n-1}^2\right) = \begin{cases} (4\bar{x}^2 - 1)\, e^{-\bar{x}^2} & n = 1 \\ (16\bar{x}^4 - 20\bar{x}^2 + 4)\, e^{-\bar{x}^2} & n = 2 \end{cases}. \tag{6.79}$$

For $n = 1$ we can substitute in the results of $4\varphi_{(2)} - \varphi_{(0)}$ for the subscript numbers corresponding to the axion mode $\varphi_{(p)}$[9], which was defined in Section 6.5 equation (6.48):

$$\begin{aligned}\varphi_1 =& \frac{g_{\varphi\Psi}}{5\pi\sqrt{\pi}} \frac{QB_0}{\sqrt{eB_0}\mathcal{E}_0\sigma_b} e^{-\frac{(z-t)^2}{2\sigma_b^2}} \\ &\times \left[\frac{\sqrt{\pi}}{\bar{\omega}}\left(\frac{\bar{\omega}^2}{4} + \frac{1}{4}\right)\left[\mathrm{erf}(+)e^{\bar{\omega}\bar{x}} - \mathrm{erf}(-)e^{-\bar{\omega}\bar{x}} - 2\cosh(\bar{\omega}\bar{x})\right] e^{\frac{\bar{\omega}^2}{4}} + e^{-\bar{x}^2}\right],\end{aligned} \tag{6.80}$$

where we have used (6.73) and defined

$$\mathrm{erf}(+) =\mathrm{erf}\left(\bar{x} + \frac{\bar{\omega}}{2}\right) \tag{6.81}$$
$$\mathrm{erf}(-) =\mathrm{erf}\left(\bar{x} - \frac{\bar{\omega}}{2}\right). \tag{6.82}$$

For $n = 2$ the solution for the axion field is

$$\begin{aligned}\varphi_2 =& \frac{g_{\varphi\Psi}}{12\pi\sqrt{2\pi}} \frac{QB_0}{\sqrt{eB_0}\mathcal{E}_0\sigma_b} e^{-\frac{(z-t)^2}{2\sigma_b^2}} \\ &\times \left[\frac{\sqrt{\pi}}{\bar{\omega}}\left(\frac{\bar{\omega}^4}{4} + \frac{7\bar{\omega}^2}{4} + \frac{3}{2}\right)\left[\mathrm{erf}(+)e^{\bar{\omega}\bar{x}} - \mathrm{erf}(-)e^{-\bar{\omega}\bar{x}} - 2\cosh(\bar{\omega}\bar{x})\right] e^{\frac{\bar{\omega}^2}{4}} \right. \\ &\left. + \frac{e^{-\bar{x}^2}}{2}\left(8\bar{x}^2 + 2\bar{\omega}^2 + 15\right)\right].\end{aligned} \tag{6.83}$$

[9] We here denote the axion mode number in parentheses, to distinguish from the axion sourced by electrons in a given energy state.

6.6.4 The axion flux

The axion flux is given by the energy momentum tensor T^{0i} and can be shown (??) to be

$$\mathcal{P} = -\partial_t \varphi \nabla \varphi. \tag{6.84}$$

The axion flux in the longitudinal direction is

$$\begin{aligned}\mathcal{P}_1 =& \frac{g_{\varphi\Psi}^2 \hbar^2 Q^2 B_0^2}{25\pi^3 e B_0 \mathcal{E}_0^2 \sigma_b^6}(z-t)^2 e^{-\frac{(z-t)^2}{\sigma_b^2}} \\ &\times \left[\frac{\sqrt{\pi}}{\bar{\omega}}\left(\frac{\bar{\omega}^2}{4}+\frac{1}{4}\right)\left[\operatorname{erf}(+)e^{\bar{\omega}\bar{x}} - \operatorname{erf}(-)e^{-\bar{\omega}\bar{x}} - 2\cosh(\bar{\omega}\bar{x})\right] e^{\frac{\bar{\omega}^2}{4}} + e^{-\bar{x}^2}\right]^2\end{aligned} \tag{6.85}$$

$$\begin{aligned}\mathcal{P}_2 =& \frac{g_{\varphi\Psi}^2 \hbar^2 Q^2 B_0^2}{288\pi^3 e B_0 \mathcal{E}_0^2 \sigma_b^6}(z-t)^2 e^{-\frac{(z-t)^2}{\sigma_b^2}} \\ &\times \left[\frac{\sqrt{\pi}}{\bar{\omega}}\left(\frac{\bar{\omega}^4}{4}+\frac{7\bar{\omega}^2}{4}+\frac{3}{2}\right)\left[\operatorname{erf}(+)e^{\bar{\omega}\bar{x}} - \operatorname{erf}(-)e^{-\bar{\omega}\bar{x}} - 2\cosh(\bar{\omega}\bar{x})\right] e^{\frac{\bar{\omega}^2}{4}}\right. \\ &\left. \quad + \frac{e^{-\bar{x}^2}}{2}\left(8\bar{x}^2 + 2\bar{\omega}^2 + 15\right)\right]^2.\end{aligned} \tag{6.86}$$

6.7 Analysing the axion flux

The transverse spread of the flux, given by the square brackets in equations (6.85), (6.86), is strongly dependent on the value of $\bar{\omega}$. In this section we will investigate the relationship between the flux and $\bar{\omega}$ for a range of mode numbers. To do this, we use the relationship below, which is obtained from equation (6.78), where we have explicitly shown the modal dependency of $\alpha(n)$. The other factors that do not depend on the transverse position or mode number only act to scale the result and are ignored in much of the analysis of this section, hence we write

$$\mathcal{P}_{(n)} \propto \left[\frac{\sqrt{n} \int_{-\infty}^{\infty} d\bar{x}' G(\bar{x}, \bar{x}') \left(\tilde{\Theta}_n^2 - \tilde{\Theta}_{n-1}^2 \right)}{\int_0^{\infty} d\bar{x} \bar{x} \left(\tilde{\Theta}_n^2 + \tilde{\Theta}_{n-1}^2 \right)} \right]^2 . \tag{6.87}$$

.

In Figures 6.1 - 6.4 we show the flux variation with transverse position, illustrating distinct dependence on the magnitude of $\bar{\omega}$. All the graphs referenced are plotted against the dimensionless parameter $\bar{x}$ defined in equation (6.9). For our choice of magnetic field $B_0 = 35$ T, we have the relation $x = \bar{x} \times 4.34$ nm.

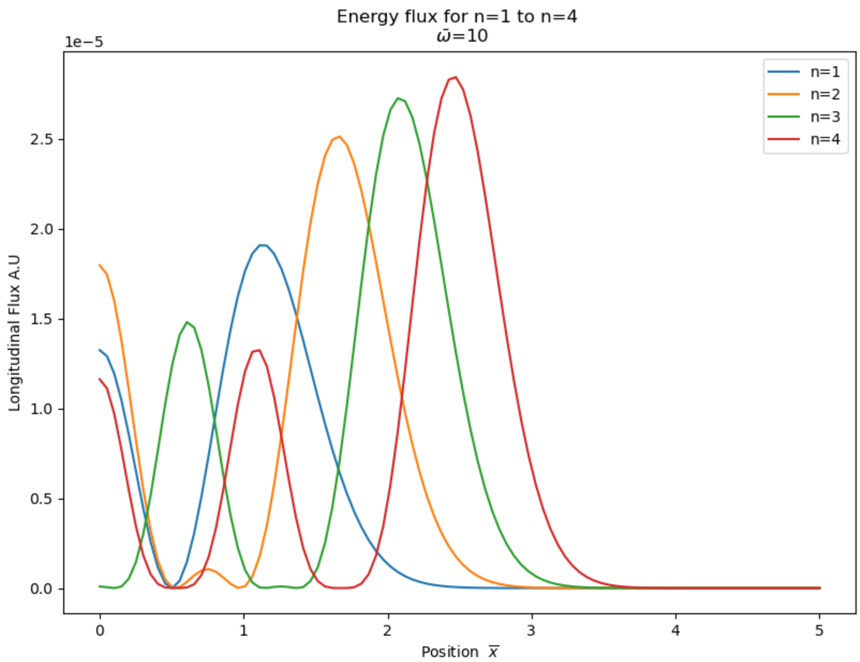

Figure 6.1: Transverse variation of the flux for modes $n = 1$–4 for $\bar{\omega} = 10$. The peak position of the flux is at $\bar{x} = 1.13$, $\bar{x} = 1.65$, $\bar{x} = 2.08$, $\bar{x} = 2.45$, respectively.

When $\bar{\omega} \geq 1$ the transverse extent of the flux becomes oscillatory with the position of the peak flux being off axis. The peak position of the flux is further off axis as the mode number increases. For the number of modes sampled, the largest peak flux did not come from the highest mode, instead coming from one

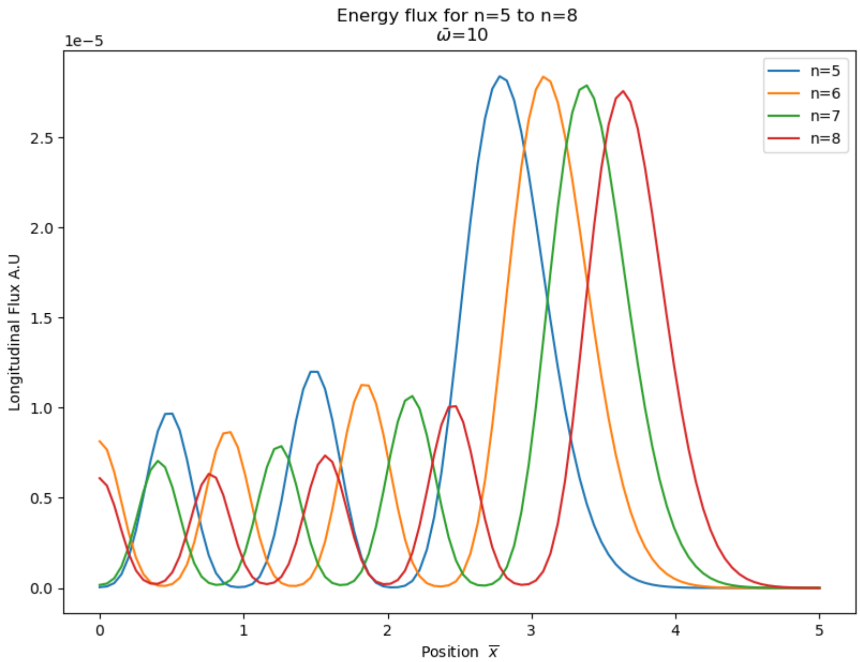

Figure 6.2: Transverse variation of the flux for modes $n = 5–8$ for $\bar{\omega} = 10$. The peak position of the flux is at $\bar{x} = 2.78$, $\bar{x} = 3.10$, $\bar{x} = 3.37$, $\bar{x} = 3.63$, respectively.

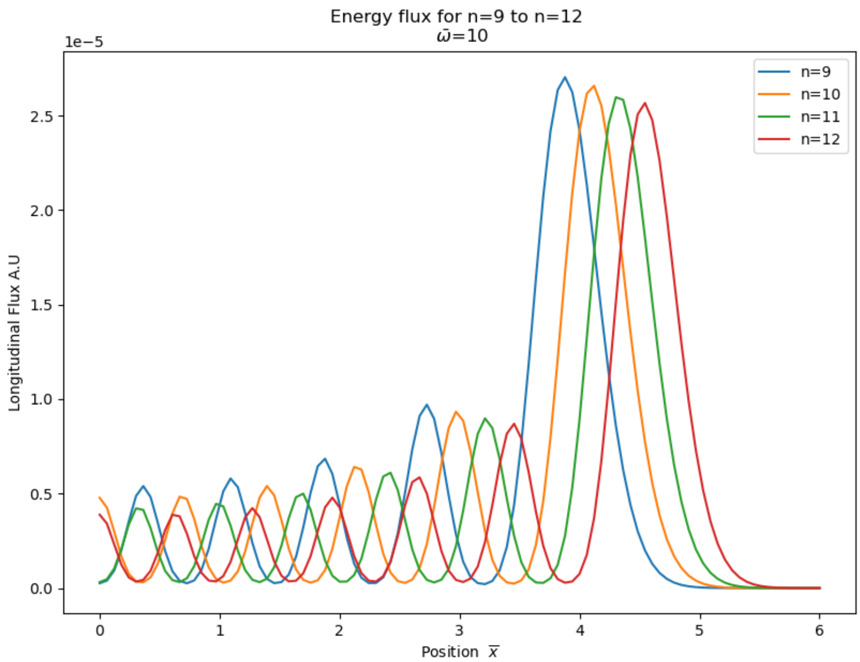

Figure 6.3: Transverse variation of the flux for modes $n = 9–12$ for $\bar{\omega} = 10$. The peak position of the flux is at $\bar{x} = 3.88$, $\bar{x} = 4.11$, $\bar{x} = 4.33$, $\bar{x} = 4.54$, respectively.

of the initial modes - for $1 \leq \bar{\omega} \leq 30$ this occurred between the fourth and sixth modes.

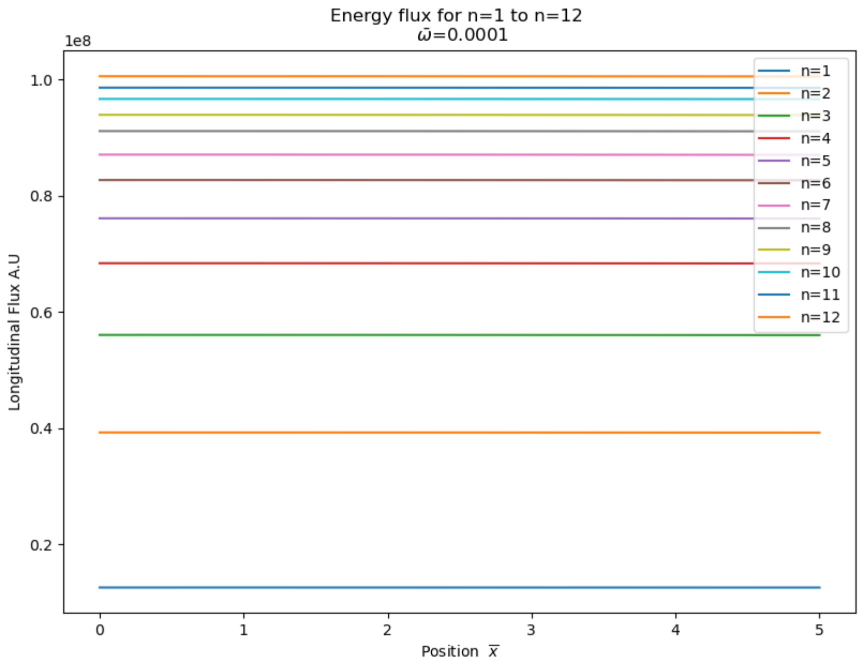

Figure 6.4: Transverse variation of the flux for modes $n = 1$–12 for $\bar{\omega} = 0.0001$. The peak values of the flux are closer to the origin and are located at $\bar{x} = 1.01$, $\bar{x} = 0.00$, $\bar{x} = 0.30$, $\bar{x} = 0.00$, $\bar{x} = 0.20$, $\bar{x} = 0.00$, $\bar{x} = 0.10$, $\bar{x} = 0.00$, $\bar{x} = 0.10$, $\bar{x} = 0.00$, respectively.

For $\bar{\omega} < 1$ the flux varies very little with transverse position, only slightly decreasing in value. For smaller values of $\bar{\omega}$ this rate is decreased. The peak position is, in general, a lot closer to the origin than when $\bar{\omega} \geq 1$, and is at the origin for even modes. We can further see that as the mode number increases so too does the flux but at a sub-linear rate.

For the parameter values of our theoretical set up, the three distinct $\bar{\omega}$ relations derived in Section 6.4 are

$$\bar{\omega} = \sqrt{\frac{\delta^2 m_e^2}{eB_0\mathcal{E}_0^2}} \qquad m_\varphi^2\mathcal{E}_0^2 \ll \delta^2 m_e^2 \tag{6.36 Revisited}$$

$$\bar{\omega} = \sqrt{\frac{\delta^2 m_e^2 + m_\varphi^2\mathcal{E}_0^2}{eB_0\mathcal{E}_0^2}} \qquad m_\varphi^2\mathcal{E}_0^2 \approx \delta^2 m_e^2 \tag{6.37 Revisited}$$

$$\bar{\omega} = \sqrt{\frac{m_\varphi^2}{eB_0}} \qquad m_\varphi^2\mathcal{E}_0^2 \gg \delta^2 m_e^2. \tag{6.38 Revisited}$$

For an electron bunch duration of 1 fs we have an energy spread of $\delta = 0.66$ eV. Due to the way in which we have chosen to model the system, by solving the Dirac field for a single electron and then increasing the charge to approximate an electron bunch[10], we have an artificially small energy spread. Typically, an electron bunch energy spread of (0.1-1)% would be considered good, which would put δ on the order of MeV. However, as the Dirac equation is linear, if we assume the electrons are acting coherently, we can scale the result of one electron to model the result of an electron bunch of charge Q. The resultant flux would then be proportional to Q^2 (as can be seen in equations (6.85, 6.86)). We could instead scale the flux that results from a single electron, which would be equivalent to the flux scaling linearly with the number of electrons, which would reflect the electrons acting incoherently.

To give an idea of the magnitude of $\bar{\omega}$ for a given electron energy spread, we have listed each of the forms of $\bar{\omega}$ in Tables 6.1 and 6.2 along with the corresponding axion mass. In both tables the other variables are constant and specified as $B_0 = 35$ T and $\mathcal{E}_0 = 1$ GeV.

We also point out that, in experiments using high-quality relativistic electron beams, a beam divergence on the order of 0.1 mrad is very good, but still realistic. However, in the work presented here, for the parameters used, the first few

[10]By introducing the electron 'bunch' we are able to make use of the bunch duration when constructing our modulation that we applied to the Dirac field.

Table 6.1: The dominant terms $\bar{\omega}$ depends on, and the corresponding axion mass for an electron energy spread of $\delta = 0.66$ eV

m_φ (eV)	$\bar{\omega}$	$\bar{\omega}$ form
$< 1 \times 10^{-5}$	7.42×10^{-6}	$\sqrt{\frac{\delta^2 m_e^2}{eB_0 \mathcal{E}_0^2}}$
$3 \times 10^{-5} - 3 \times 10^{-3}$	$(7.45 - 66.30) \times 10^{-6}$	$\sqrt{\frac{\delta^2 m_e^2 + m_\varphi^2 \mathcal{E}_0^2}{eB_0 \epsilon_0^2}}$
$> 5 \times 10^{-3}$	$> 1 \times 10^{-4}$	$\sqrt{\frac{m_\varphi^2}{eB_0}}$

Table 6.2: The dominant terms $\bar{\omega}$ depends on, and the corresponding axion mass for an electron energy spread of $\delta = 1$ MeV

m_φ (eV)	$\bar{\omega}$	$\bar{\omega}$ form
< 50	11.25	$\sqrt{\frac{\delta^2 m_e^2}{eB_0 \mathcal{E}_0^2}}$
$51 - 5100$	$11.30 - 113$	$\sqrt{\frac{\delta^2 m_e^2 + m_\varphi^2 \mathcal{E}_0^2}{eB_0 \epsilon_0^2}}$
> 5100	> 113	$\sqrt{\frac{m_\varphi^2}{eB_0}}$

modes equate to having a beam divergence on the order of 10^{-4} mrad which is not realistic for current laser facilities. A beam divergence of 0.1 mrad corresponds to a mode number of roughly $n = 2 \times 10^6$. We can approximate the value of the peak flux for higher order modes by modelling a fit to the peaks of the flux against mode number. However, given that the mode numbers we have calculated are significantly lower than realistic beam divergences, we cannot extrapolate to meaningful results with any confidence. Finally, there are two distinct relationships that can be observed in the peak axion flux vs mode number that occur for roughly $\bar{\omega} < 1$ and $\bar{\omega} > 1$. These are illustrated in Figures 6.5 and 6.6.

In one regime ($\bar{\omega} < 1$), the peak energy flux increases with mode number, but the increments become progressively smaller, indicating a growth that slows as n increases. In the other regime ($\bar{\omega} > 1$) the largest peak flux across the modes occurs for a low value of n, after which the peak flux of higher modes continues to decrease with mode number.

The transverse extent of the flux (the square bracket in equations (6.85) and

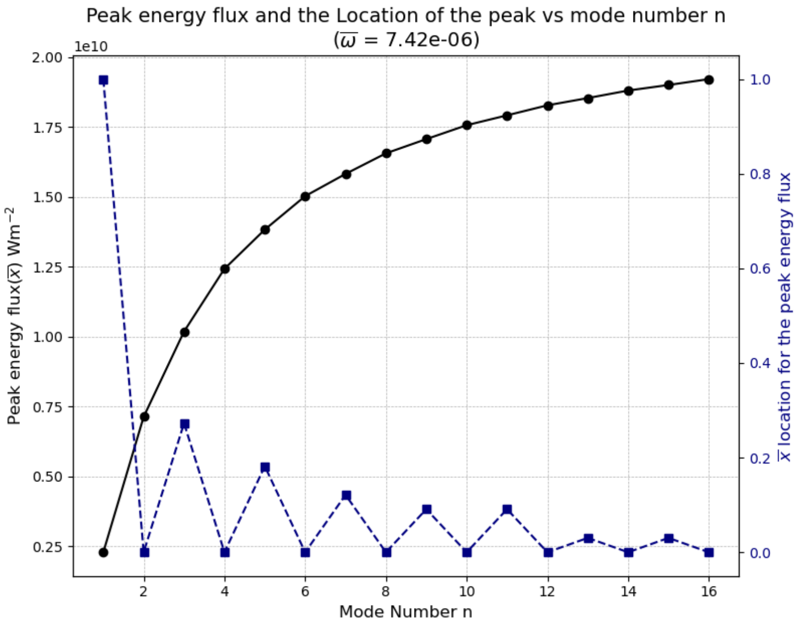

Figure 6.5: Peak flux versus mode number for $\bar{\omega} = 7.42 \times 10^{-6}$. The peak flux increases with mode number but at a decreased rate. The peak flux is near $\bar{x} = 0$ with it alternating between $\bar{x} = 0$ and $\bar{x} \leq 1$ for the modes sampled.

(6.86)) is complicated and makes calculating the energy flux of larger mode number over a finite $\bar{x}$ range difficult. In the regime where $\bar{x} < 1$ the peak flux is close to or at $\bar{x} = 0$. It also corresponds to the lightest axions (see Tables 6.1, 6.2) which tend to receive the most attention in the literature. The flux can be simplified significantly by assuming $\bar{x} = 0$ (in the case of $n = 2$ the square brackets of equation (6.86) simplifies to $\frac{9\pi}{\bar{\omega}^2}$) and the energy flux can be calculated for larger values of n, see Table 6.3, where we have set $B_0 = 35$ T, $\mathcal{E}_0 = 1$ GeV and $g_{\varphi\Psi} = 1.3 \times 10^{-13}$.

Additionally, in this regime we can derive an analytical expression for the energy flux. For $n = 2$ we have

$$\mathcal{P}_2(\bar{x} = 0) = \frac{g_{\varphi\psi}^2}{32\pi^2} \frac{\hbar^3}{m_e^2 c^2} \frac{Q^2 B_0^2}{\delta^2 \sigma_b^6} (z-t)^2 e^{-\frac{(z-t)^2}{\sigma_b^2}}, \tag{6.88}$$

where we have used equation (6.86). In this case $\bar{\omega}$ is given by equation (6.36)

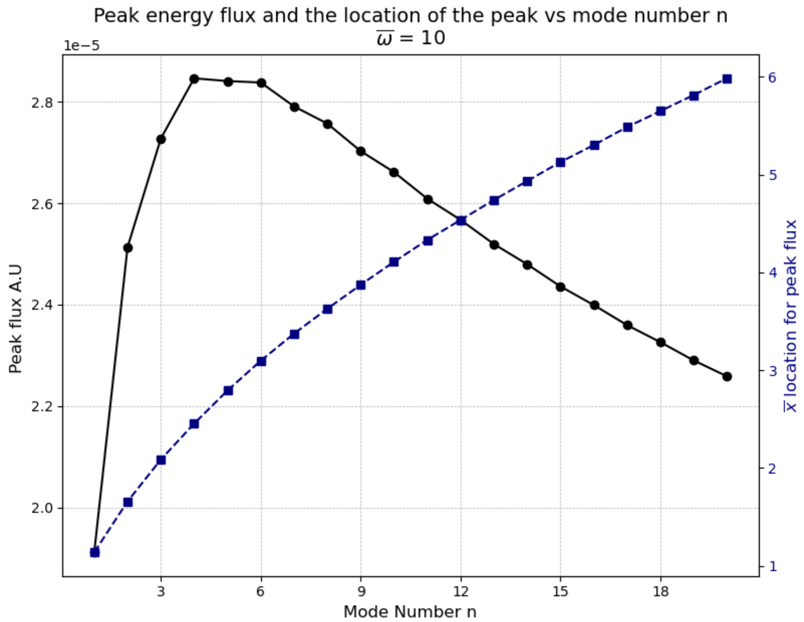

Figure 6.6: Peak flux versus mode number for $\bar{\omega} = 10$. The peak flux is largest in one of the initial modes after which it decreases with mode number. The transverse position of the peak flux increases with mode number.

Table 6.3: Energy flux for $\bar{\omega} = 7.42 \times 10^{-6}$ measured at $\bar{x} = 0$.

mode number (n)	**energy flux ($\mathrm{W\,m^{-2}}$)**
1	2.9579×10^{-5}
5	1.7925×10^{-4}
10	2.2767×10^{-4}
15	2.4633×10^{-4}
20	2.5671×10^{-4}
26	2.6425×10^{-4}
27	2.6442×10^{-4}
28	2.6672×10^{-4}

and the flux is independent of the peak electron energy, depending only on the electron bunch duration (or equivalently, the energy spread). To obtain the peak flux we set $(z - t) = \sigma_b$:

$$\left[\frac{\mathcal{P}_2}{\mathrm{Wm}^{-2}}\right] = 4.47 \times 10^{-8} g_{13}^2 \left[\frac{Q}{\mathrm{nC}}\right]^2 \left[\frac{B_0}{\mathrm{T}}\right]^2 \left[\frac{\sigma_b}{\mathrm{fs}}\right]^{-2}, \tag{6.89}$$

where $g_{\varphi\Psi} = g_{13} \times 10^{-13}$ and $\delta = \hbar/\sigma_b$. To obtain the number flux precisely would require knowledge of the spectral information, by Fourier transforming, dividing by ω, and transforming back again. This is a point we intend to return to in future work. As the relation between energy and number flux depends only on the longitudinal profile, all of the above discussion regarding the transverse dependence will apply equally to the number flux.

6.8 Dilaton

The other BSM particle we study in this chapter is the dilaton, the scalar cousin of the axion. As with the preceding two chapters, the procedure for the dilaton is much the same as for the axion, and therefore we will only show the key equations, highlighting the differences with the axionic case.

6.8.1 The dilaton field

As we have a Klein-Gordon equation for the dilaton's equation of motion, we can utilise our results from Section 6.5 with regard to solving using a Green's function. We can then write the dilaton equation as a product of longitudinal integrals (momentum integrals 6.61) and transverse integrals (integral of the Green's function, see Section 6.5)

$$\Phi = \frac{g_{\Phi\Psi}}{eB_0} \int_{-\infty}^{\infty} \left[d\bar{x}' G(\bar{x}, \bar{x}') \left(\int_{-\infty}^{\infty} dp dp' |\alpha^2| A(p) A(p') \bar{\psi}\psi \right) \right]. \tag{6.90}$$

Solving equation (6.90) follows the same method used for the axion. We therefore omit the intermediate steps and show the solution

$$\Phi_n(\bar{x}) = \frac{\sqrt{2n}\pi\alpha_n^2 g_{\Phi\Psi}}{\sqrt{eB_0}\sigma_b^2} e^{-\frac{(z-t)^2}{2\sigma_b^2}} \left(\frac{(z-t)}{\sigma_b^2} - \sqrt{2neB_0} \right) \int_{-\infty}^{\infty} d\bar{x}' G(\bar{x}, \bar{x}') \left(\tilde{\Theta}_n^2 + \tilde{\Theta}_{n-1}^2 \right), \tag{6.91}$$

with the first two modes being

$$\begin{aligned}\Phi_1(\bar{x}) =& \frac{g_{\Phi\Psi} Q B_0}{10\pi\sqrt{\pi}\sqrt{eB_0}\sigma_b \mathcal{E}_0^2} e^{-\frac{(z-t)^2}{2\sigma_b^2}} \left(\frac{(z-t)}{\sigma_b^2} - \sqrt{2eB_0} \right) \\ & \times \left[\frac{\sqrt{\pi}}{\bar{\omega}} \left(\frac{\bar{\omega}^2}{4} + \frac{3}{4} \right) \left[\mathrm{erf}(+) e^{\bar{\omega}\bar{x}} - \mathrm{erf}(-) e^{-\bar{\omega}\bar{x}} - 2\cosh(\bar{\omega}\bar{x}) \right] e^{\frac{\bar{\omega}^2}{4}} + e^{-\bar{x}^2} \right]\end{aligned} \tag{6.92}$$

$$\begin{aligned}\Phi_2(\bar{x}) =& \frac{g_{\Phi\Psi} Q B_0}{24\pi\sqrt{2\pi}\sqrt{eB_0}\sigma_b \mathcal{E}_0^2} e^{-\frac{(z-t)^2}{2\sigma_b^2}} \left(\frac{(z-t)}{\sigma_b^2} - \sqrt{4eB_0} \right) \\ & \times \left[\frac{\sqrt{\pi}}{\bar{\omega}} \left(\frac{\bar{\omega}^4}{4} + \frac{9\bar{\omega}^2}{4} + \frac{5}{2} \right) \left[\mathrm{erf}(+) e^{\bar{\omega}\bar{x}} - \mathrm{erf}(-) e^{-\bar{\omega}\bar{x}} - 2\cosh(\bar{\omega}\bar{x}) \right] e^{\frac{\bar{\omega}^2}{4}} \right. \\ & \qquad \left. + \frac{e^{-\bar{x}^2}}{2} \left(8\bar{x}^2 + 2\bar{\omega}^2 + 17 \right) \right].\end{aligned} \tag{6.93}$$

Compared with the axion (equation (6.78)), the dilaton expression contains two bracketed terms giving $\sqrt{n}$ and n contributions. However, at the peak magnitude of the flux ($(z-t) = \sigma_b$) the $\sqrt{n}$ term is eliminated and the n term dominates, giving an overall n^2 scaling to the flux. Additionally, the transverse integral now sums squared Hermite polynomials instead of taking their difference, so the set of transverse modes that combine to form the dilaton field differs from the axionic case. Also, the scalar contraction depends on peak electron energy only through α, while the pseudoscalar contraction has an extra direct energy-proportional term (see equation (6.77)) causing the scalar flux to decrease more strongly with electron energy.

For Hermite mode number $n = 1, 2$ we have the following longitudinal flux

$$\mathcal{P}_1 = \frac{g_{\Phi\Psi}^2 Q^2 B_0^2}{100\pi^3 e B_0 \sigma_b^6 \mathcal{E}_0^4} e^{-\frac{(z-t)^2}{\sigma_b^2}} \left(1 - \frac{(z-t)^2}{\sigma_b^2} + \sqrt{2eB_0}(z-t)\right)^2 \\ \times \left[\frac{\sqrt{\pi}}{\bar{\omega}}\left(\frac{\bar{\omega}^2}{4} + \frac{3}{4}\right)\left[\mathrm{erf}(+)e^{\bar{\omega}\bar{x}} - \mathrm{erf}(-)e^{-\bar{\omega}\bar{x}} - 2\cosh(\bar{\omega}\bar{x})\right] e^{\frac{\bar{\omega}^2}{4}} + e^{-\bar{x}^2}\right]^2 \tag{6.94}$$

$$\mathcal{P}_2 = \frac{g_{\Phi\Psi}^2 Q^2 B_0^2}{1152\pi^3 e B_0 \sigma_b^6 \mathcal{E}_0^4} e^{-\frac{(z-t)^2}{\sigma_b^2}} \left(1 - \frac{(z-t)^2}{\sigma_b^2} + \sqrt{4eB_0}(z-t)\right)^2 \\ \times \left[\frac{\sqrt{\pi}}{\bar{\omega}}\left(\frac{\bar{\omega}^4}{4} + \frac{9\bar{\omega}^2}{4} + \frac{5}{2}\right)\left[\mathrm{erf}(+)e^{\bar{\omega}\bar{x}} - \mathrm{erf}(-)e^{-\bar{\omega}\bar{x}} - 2\cosh(\bar{\omega}\bar{x})\right] e^{\frac{\bar{\omega}^2}{4}} \right. \\ \left. + \frac{e^{-\bar{x}^2}}{2}\left(8\bar{x}^2 + 2\bar{\omega}^2 + 17\right)\right]^2. \tag{6.95}$$

As with the axion, we study how the longitudinal flux depends on $\bar{\omega}$ across mode number n. To maximise the flux we fix $(z - t) = \sigma_b$; this choice removes the $\sqrt{n}$ contribution, simplifying the expression. The relationship we investigate is given by

$$\mathcal{P}_{(n)} \propto \left[\frac{n\int_{-\infty}^{\infty} d\bar{x}' G(\bar{x}, \bar{x}')\left(\tilde{\Theta}_n^2 + \tilde{\Theta}_{n-1}^2\right)}{\int_0^{\infty} d\bar{x}\bar{x}\left(\tilde{\Theta}_n^2 + \tilde{\Theta}_{n-1}^2\right)}\right]^2. \tag{6.96}$$

The same general trends can be seen when looking at the transverse variation of the flux for individual modes. Figures 6.7–6.9 show that the flux is oscillatory, with the peak flux being off axis when $\bar{\omega} > 1$. The position of the peak flux increases with mode number as in the axion case. Figure 6.10 shows that the flux tapers off more gradually with transverse position with the peak position being at $\bar{x} = 0$, when $\bar{\omega} < 1$.

The key difference between the dilaton flux and the axion flux for $\bar{\omega} > 1$ is that the dilaton peak flux per mode increases with mode number, whereas the axion peak flux eventually decreases with n. When $\bar{\omega} < 1$, the dilaton peak energy flux

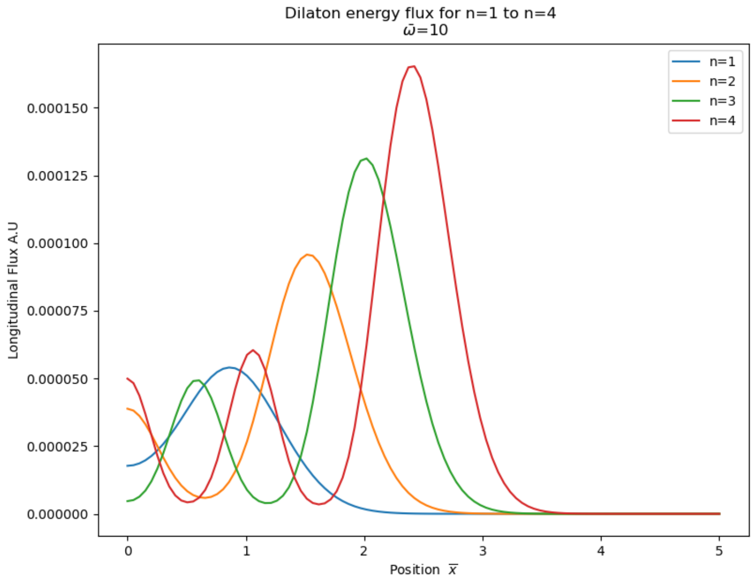

Figure 6.7: Transverse variation of the flux for modes $n = 1$–4. The peak flux is at a position of $\bar{x} = 0.86$, $\bar{x} = 1.53$, $\bar{x} = 2.00$, $\bar{x} = 2.40$ respectively.

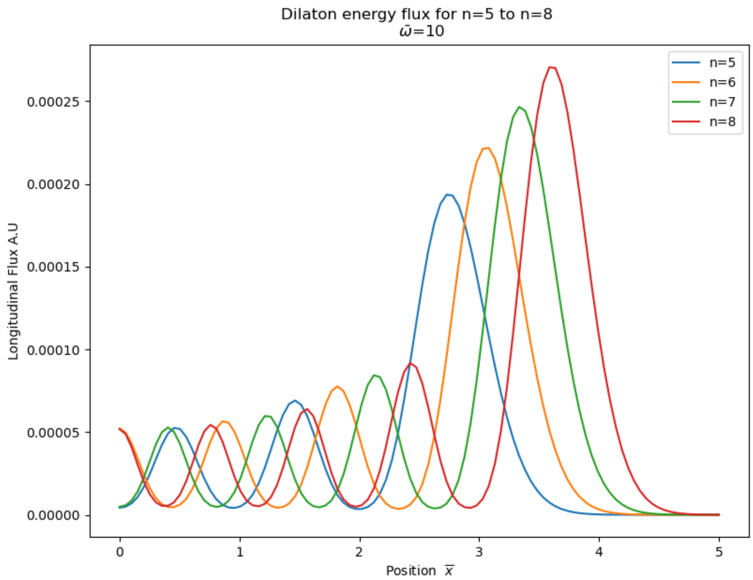

Figure 6.8: Transverse variation of the flux for modes $n = 5$–8. The peak flux is at a position of $\bar{x} = 2.74$, $\bar{x} = 3.06$, $\bar{x} = 3.34$, $\bar{x} = 3.61$ respectively.

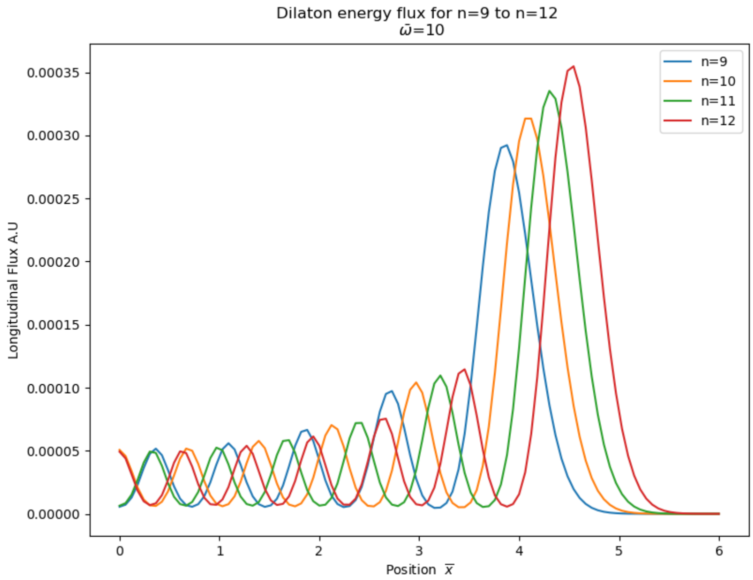

Figure 6.9: Transverse variation of the flux for modes $n = 9$–12. The peak flux is at a position of $\bar{x} = 3.86$, $\bar{x} = 4.09$, $\bar{x} = 4.32$, $\bar{x} = 4.53$ respectively.

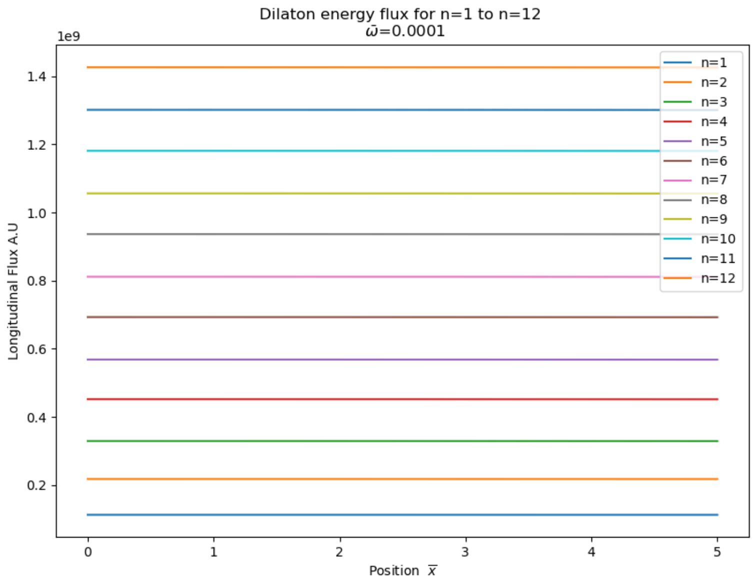

Figure 6.10: Transverse variation of the flux for modes $n = 1$–12 for $\bar{\omega} = 0.0001$. The peak values of the flux are all located at $\bar{x} = 0$.

grows roughly proportional to n, while the axion peak flux grows sub-linearly with n. These trends are shown more clearly in Figures 6.11 and 6.12, which plot the peak energy flux per mode as a function of mode number.

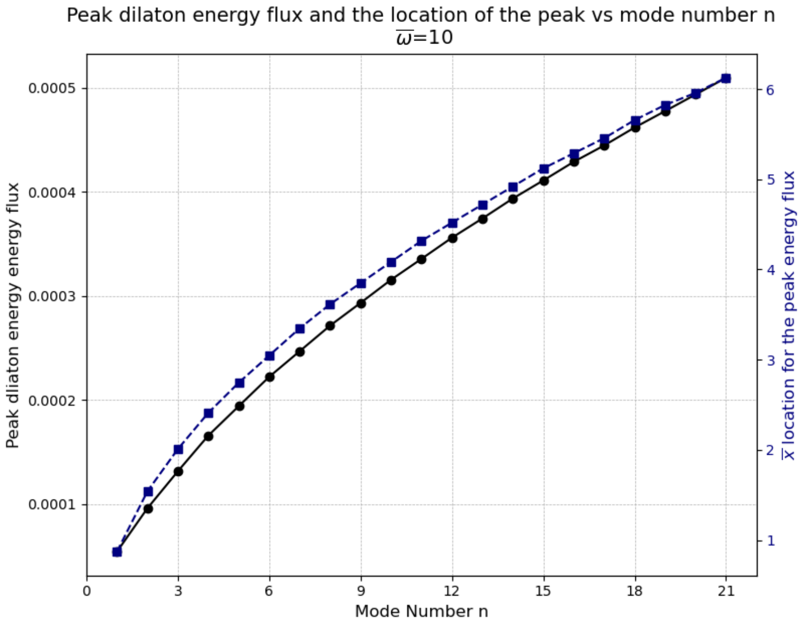

Figure 6.11: The change in the peak flux with mode number for $\bar{\omega} = 10$. The peak flux and location of the peak increase with mode number.

For the modes that we have studied, it appears that the peak dilaton flux always increases with the mode number, regardless of the magnitude of $\bar{\omega}$, which contrasts with the axionic case. There are still similarities to the axion in that the location of the peak flux when $\bar{\omega} < 1$ is closer to $\bar{x} = 0$, and when $\bar{\omega} > 1$ the location is proportional to the mode number. In Figure 6.13 we apply a linear fit to data from Figure 6.12. In Figure 6.14 we apply a square root fit to a subset of that data from Figure 6.11.

For $\bar{\omega} < 1$ the peak energy flux increases approximately linearly with mode number. A linear fit produces an approximately constant slope across the fitted range that can be extrapolated. By contrast, the axion exhibited sub-linear growth and extrapolation of this data would be highly sensitive to the chosen

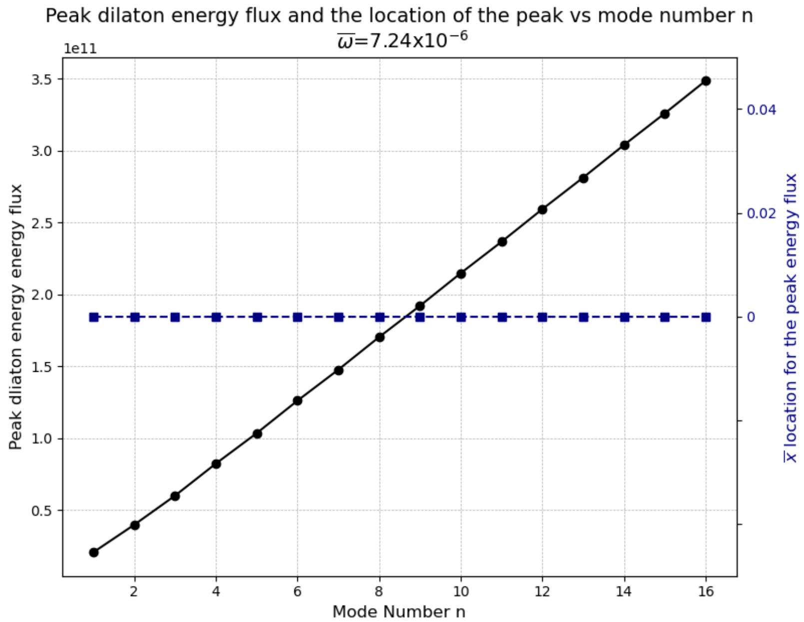

Figure 6.12: The change in the peak flux with mode number for $\bar{\omega} = 7.42 \times 10^{-6}$. The peak flux grows linearly with mode number, with the location of the peak being always being at $\bar{x} = 0$.

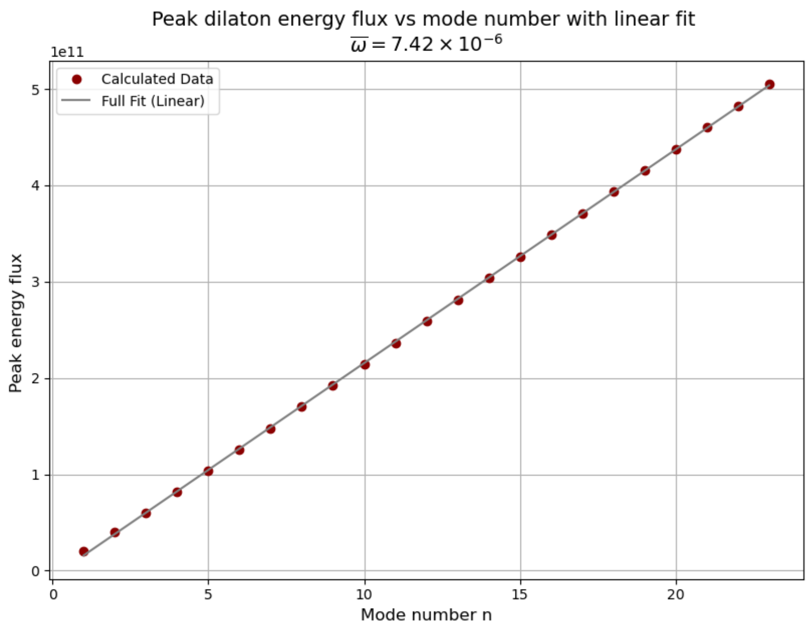

Figure 6.13: The peak dilaton flux vs mode number. A fit of the form $f(n) = an + b$ has been applied to the whole data set. The R^2 of the fit is 0.9999.

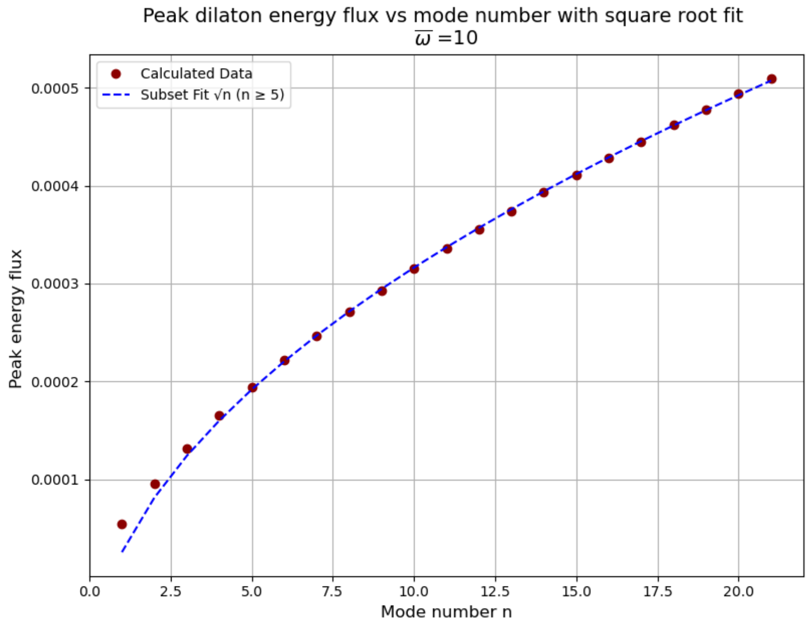

Figure 6.14: The peak dilaton flux vs mode number. A fit of the form $f(n) = a\sqrt{n} + b$ has been applied to a subset of the data beginning with $n = 5$. The R^2 of the fit is 0.9934.

fit. Such sensitivity would lead to significant uncertainties in the extrapolated results.

In Table 6.4 we extrapolate the data in Figure 6.13 to mode numbers that correspond to realistic electron beam divergences of 0.1 mrad and 1 mrad.

6.9 Chapter conclusions

Here we explored fermionic coupling as a production channel for axions and dilatons by analysing the propagation of a charged electron in a uniform magnetic field. The transverse structure of the source results in Hermite-polynomial solutions, with the polynomial order equated with the electron's Landau level. The axion/dilaton energy flux is best parametrised by the dimensionless quantity $\bar{\omega}$, defined as $\bar{\omega} = \sqrt{\frac{(m_\varphi^2+\delta^2)m_e^2+m_\varphi^2\mathcal{E}_0^2}{eB_0\mathcal{E}_0}}$ where m_φ is the axion mass, δ is the electron 'bunch' energy spread and $\mathcal{E}_0$ the electron energy. For the parameter range stud-

Table 6.4: Extrapolated peak dilaton flux, $\bar{\omega} = 7.42 \times 10^{-6}$

Mode Number (n)	**Linear Full Fit**
10.0	2.1534×10^{11}
15.0	3.2608×10^{11}
20.0	4.3681×10^{11}
25.0	5.4754×10^{11}
30.0	6.5827×10^{11}
35.0	7.6900×10^{11}
40.0	8.7973×10^{11}
100.0	2.2085×10^{12}
1000.0	2.2140×10^{13}
10000.0	2.2146×10^{14}
2400000.0	5.3151×10^{16}
238000000.0	5.2708×10^{18}

ied, axion production is suppressed with increasing mode number when $\bar{\omega} > 1$, whereas for $\bar{\omega} \leq 0.1$ the peak flux increases sub-linearly. In contrast, the dilaton flux increases with mode number across the full range of $\bar{\omega}$. We modelled this increase using both linear and square-root fits. The improved scaling with mode number for dilaton production yields a larger energy flux than for axions for equal masses and couplings.

The axion energy flux (we will symbolically denote this as E_φ here whilst we compare with previous chapters results) determined in this chapter for $\bar{\omega} = 7.42 \times 10^{-6}$ is $E_\varphi = 1.47 \times 10^{-4}$ Wm^{-2}, which is within an order of magnitude of the result from Chapter 4 and is much smaller than the driven-plasma-wave result from Chapter 5 ($E_\varphi = 2.39 \times 10^{-3}$ Wm^{-2} and $E_\varphi = 6.45 \times 10^{13}$ Wm^{-2}, respectively). The extrapolated dilaton flux ($n = 2.4 \times 10^6$) is $E_\Phi = 685.12$ Wm^{-2}. We did not compute the number flux in this chapter. However, the analytic structure and relations derived for the energy flux apply equally to number flux when the spectral details are determined.

Future work should prioritise three tasks. First, to derive the axion and dilaton number flux by Fourier transform, dividing by the frequency, and inverse transforming, so that direct comparisons can be made with other production mechanisms. Second, to generalise the single-electron solution to a realistic electron bunch model. This would allow better quantification of the parameter $\bar{\omega}$, in relation to which axion mass ranges lead to distinct behaviours in the resultant axion flux vs position, or Landau level of the electron (for realistic electron bunch energy spreads). Third, to compute the flux at larger mode numbers directly, rather than relying on extrapolation to confirm the trends in the peak flux found.

Chapter 7

Summary

Axion-like particles (ALPs) are of broad interest. They may resolve the strong CP problem, are viable dark-matter candidates, appear in many extensions of the Standard Model, and could account for a range of astrophysical phenomena. Although no confirmed detection has been made, increasingly stringent bounds have been placed on axion masses and on their electromagnetic and fermionic couplings. These bounds are often model dependent or rely on cosmological assumptions about the early universe. Laboratory experiments avoid many of those assumptions and therefore play a crucial role in axion searches. In this work we explore three laboratory production mechanisms for ALPs: two that exploit electromagnetic couplings and one that uses the fermionic coupling.

In Chapter 4 we explored axion production utilizing high intensity laser pulses. The modification of Maxwell's equations from the axion results in a coupling between the laser fields. The 'pump' laser drives this interaction where the 'probe' laser field is modified in the presence of the background pump laser field and oscillates between axion-like and photon-like characteristics. The polarisations and propagation directions of the two laser pulses are chosen to maximise this process. The resultant axion flux is proportional to the intensities of the two laser fields. A high photon count from the lasers results in a significant axion flux, compared with existing light shining through wall experiments (such as OSQAR and ALPS-II), without requiring resonant enhancement. The axion mass that can be probed comfortably exceeds 1 eV, by using high harmonics of the background laser field, without negatively affecting the flux. The drawback of this production method is that it requires the pump laser field to have constant amplitude throughout the interaction, which, when combined with the use of pulsed lasers limits the interaction length. Typical axion-photon oscillations have a long period, compared with the laser pulse durations, which results in the axion flux never reaching its peak. Furthermore, the flux is not continuous as it is in other experiments. However, the increase in the axion flux can balance this. To further develop this work, we intend to model different laser profiles to more accurately represent the setup in addition to relaxing the assumption of a constant (during the interaction) pump laser.

In Chapter 5 we explored the use of a nonlinear plasma wave as a source of ALPs, expanding upon the work of [77]. We derived the axion number flux by accounting for the axion energy per mode before averaging, producing an expression parametrised by $s = \frac{m_\varphi \lambda \gamma}{2\pi}$, where m_φ is the axion mass, and λ and γ are the wavelength and the Lorentz factor of the plasma wave, respectively. For $s \approx 1$ the two flux expressions (our work and that of [77]) agree to within an order of magnitude but deviate outside of this regime. We find that the flux peaks for $s = 0.59$, and changes in the plasma frequency can be used to fine-tune this. The flux is concentrated in the first mode (at least 90% when $s \leq 1$), but for larger s values it is more spread out and the flux drops off with mode number as $\frac{1}{n}$ rather than $\frac{1}{n^5}$. This method of production favours lower axion masses and can result in significant axion flux: for axion parameters $g = 0.66 \times 10^{-10}$ GeV^{-1}, $m_\varphi = 1\mu$ eV and plasma parameters, $\omega_p = 2\pi \times 10^{14}$ rad s^{-1}, $\gamma = 10,000$, a flux on the order of $N_\varphi \sim 10^{34}$ m^{-2}s^{-1} can be achieved with an applied field of $B_0 = 35$ T. This is a considerable flux compared with other laboratory methods, and in future work we will investigate how to best integrate this production method with axion detection (via reconverting into photons).

In the final chapter 6 we explored axion production using fermionic coupling. The axion source was assumed to be a relativistic electron propagating parallel to a magnetic field. The electron gyration due to the magnetic field is described by Hermite polynomials, the order of which is related to the divergence of the electron beam. The flux is parametrised by $\bar{\omega}$, which depends on the electron energy, electron energy spread, axion mass and magnetic field strength. The specific flux scaling with $\bar{\omega}$ is non-trivial but favours low values $\bar{\omega} \ll 1$. In this parameter space the flux tends to peak on axis, gradually decreasing transversely. This is in contrast to the parameter range $\bar{\omega} > 1$, where the flux is oscillatory and peaks off axis before decreasing rapidly with transverse position. We find that the peak flux when $\bar{\omega} < 1$ increases with mode number but sub-linearly. When $\bar{\omega} > 1$ we find that after the initial few modes the flux decreases with mode number. The variation of the peak flux with mode number is different for dilaton production. In this case, the peak flux always scales with mode number, to some degree, and shows no sign of saturation. To improve upon this work we intend to re-examine our derivation of the Dirac field, to better model an electron beam. This will enable us to more confidently relate different $\bar{\omega}$ parameter regions to axion mass regions, including the energy spread of an electron bunch. This, in conjunction with a more detailed analysis to explore higher order modes, could more accurately determine whether or not this is a viable scenario for axion production.

Appendix A

Appendix

A.1 Derivation of the equations of motion

There are two Euler-Lagrange equations which can be formed from the Lagrangian

$$\mathcal{L}_{\varphi,EM} = -\frac{1}{4}F^{\mu\nu}F_{\mu\nu} - A_\mu J_e^\mu + \frac{\partial_\mu\varphi\partial^\mu\varphi}{2} - \frac{m_\varphi^2\varphi^2}{2} - \frac{g_{\varphi\gamma}}{4}\varphi\tilde{F}^{\mu\nu}F_{\mu\nu}, \tag{3.8 Revisited}$$

$$\frac{\partial\mathcal{L}}{\partial A_\rho} - \partial_\mu\left(\frac{\partial\mathcal{L}}{\partial(\partial_\mu A_\rho)}\right) = 0 \tag{3.11 Revisited}$$

$$\frac{\partial\mathcal{L}}{\partial\varphi} - \partial_\mu\left(\frac{\partial\mathcal{L}}{\partial(\partial_\mu\varphi)}\right) = 0. \tag{3.12 Revisited}$$

Starting with (3.11) the first term is proportional to the sources

$$\frac{\partial\mathcal{L}}{\partial A_\mu} = -J^\mu. \tag{A.1}$$

The second term in (3.11) involves the variation of the electromagnetic tensor and its dual with respect to the derivative of the gauge potential. The derivation of each is similar thus below we only explicitly show the derivation involving the dual electromagnetic tensor,

$$\begin{aligned}
\frac{\partial(\tilde{F}^{\alpha\beta}F_{\alpha\beta})}{\partial(\partial_\mu A_\rho)} =& \frac{\partial}{\partial(\partial_\mu A_\rho)}\frac{\epsilon^{\alpha\beta\gamma\kappa}}{2}\left(\partial_\gamma A_\kappa\partial_\alpha A_\beta + \partial_\kappa A_\gamma\partial_\beta A_\alpha - \partial_\kappa A_\gamma\partial_\alpha A_\beta - \partial_\gamma A_\kappa\partial_\beta A_\alpha\right)\\
=&\frac{\epsilon^{\alpha\beta\gamma\kappa}}{2}\delta^\mu_\alpha\delta^\rho_\beta(\partial_\gamma A_\kappa - \partial_\kappa A_\gamma) + \delta^\mu_\beta\delta^\rho_\alpha(\partial_\kappa A_\gamma - \partial_\gamma A_\kappa)\\
&+ \delta^\mu_\kappa\delta^\rho_\gamma(\partial_\beta A_\alpha - \partial_\alpha A_\beta) + \delta^\mu_\gamma\delta^\rho_\kappa(\partial_\alpha A_\beta - \partial_\beta A_\alpha)\\
=&\tilde{F}^{\mu\rho} - \tilde{F}^{\rho\mu} + \frac{F_{\alpha\beta}}{2}(\epsilon^{\alpha\beta\mu\rho} - \epsilon^{\alpha\beta\mu\rho})\\
=&2\tilde{F}^{\mu\rho} - 2\tilde{F}^{\rho\mu}\\
=&4\tilde{F}^{\mu\rho}.
\end{aligned} \tag{A.2}$$

Therefore, the second term in equation (3.11) yields

$$\partial_\mu\left(\frac{\partial\mathcal{L}}{\partial(\partial_\mu A_\rho)}\right) = -\,\partial_\mu\left(g_{\varphi\gamma}\varphi\tilde{F}^{\mu\rho} + F^{\mu\rho}\right) \tag{A.3}$$

with the full Euler Lagrange equation being,

$$\frac{\partial\mathcal{L}}{\partial A_\rho} - \partial_\mu\left(\frac{\partial\mathcal{L}}{\partial(\partial_\mu A_\rho)}\right) = 0 \tag{A.4}$$

$$\partial_\mu F^{\mu\rho} + g_{\varphi\gamma}\left(\partial_\mu\varphi\right)\tilde{F}^{\mu\rho} = J^\mu \tag{A.5}$$

where $\partial_\mu\tilde{F}^{\mu\rho} = 0$ from the Bianchi identity and corresponds to the homogeneous Maxwell's equations.

We now move on to equation (3.12)

$$\frac{\partial\mathcal{L}}{\partial\varphi} = -m_\varphi^2\varphi - \frac{g_{\varphi\gamma}}{4}\tilde{F}^{\mu\rho}F_{\mu\rho} \tag{A.6}$$

$$\begin{aligned}\frac{\partial\mathcal{L}}{\partial(\partial_\mu\varphi)} &= \frac{1}{2}\frac{\partial(\partial_\alpha\varphi\partial^\alpha\varphi)}{\partial(\partial_\mu\varphi)} \\ &= \frac{1}{2}\partial^\alpha\varphi\frac{\partial(\partial_\alpha\varphi)}{\partial(\partial_\mu\varphi)} + \frac{1}{2}\partial_\alpha\varphi g^{\alpha\beta}\frac{\partial(\partial_\beta\varphi)}{\partial(\partial_\mu\varphi)} \\ &= \partial^\mu\varphi\end{aligned} \tag{A.7}$$

$$\partial_\mu\left(\frac{\partial\mathcal{L}}{\partial(\partial_\mu\varphi)}\right) = \partial_\mu\partial^\mu\varphi. \tag{A.8}$$

Combining the results from both of our Euler-Lagrange equations leads to the following equations of motion

$$\frac{\partial\mathcal{L}}{\partial A_\rho} - \partial_\mu\frac{\partial\mathcal{L}}{\partial(\partial_\mu A_\rho)} = -J^\rho + \partial_\mu\left(F^{\mu\rho} + g_{\varphi\gamma}\varphi\tilde{F}^{\mu\rho}\right) \tag{A.9}$$

$$J^\rho = \partial_\mu\left(F^{\mu\rho} + g_{\varphi\gamma}\varphi\tilde{F}^{\mu\rho}\right) \tag{A.10}$$

$$\frac{\partial\mathcal{L}}{\partial\varphi} - \partial_\mu\frac{\partial\mathcal{L}}{\partial(\partial_\mu\varphi)} = -\left(\partial_\mu\partial^\mu + m_\varphi^2\right)\varphi - \frac{g_{\varphi\gamma}}{4}\tilde{F}^{\mu\rho}F_{\mu\rho} \tag{A.11}$$

$$\left(\partial_\mu\partial^\mu + m_\varphi^2\right) = -\frac{g_{\varphi\gamma}}{4}\tilde{F}^{\mu\rho}F_{\mu\rho}. \tag{A.12}$$

Appendix B

Appendix

B.1 Axion-Photon oscillations in a static magnetic field

The axion-Maxwell equations can be linearized and expressed by way of a matrix equation as follows

$$\begin{pmatrix} \left(\omega^2 - k^2 - m_\varphi^2\right) & -g_{\varphi\gamma} B_0 \omega \\ -g_{\varphi\gamma} B_0 \omega & \left(\omega^2 - k^2\right) \end{pmatrix} \begin{pmatrix} \varphi \\ iA \end{pmatrix} = 0. \tag{B.1}$$

Two unique solutions exist to this equation in which the fields are non-zero, we refer to these as the propagating states. These states propagate with a wave number squared as follows

$$k_{1,2}^2 = \frac{2\omega^2 - m_\varphi^2 \pm \sqrt{m_\varphi^4 + \Omega^2}}{2} \tag{B.2}$$

where we have defined the following term

$$\Omega^2 = 4 g_{\varphi\gamma}^2 B_0^2 \omega^2. \tag{B.3}$$

Our matrix equation can then be inverted, such that the flavour states are expressed as a superposition of the propagating states

$$\begin{pmatrix} -\left(\frac{m_\varphi^2+\sqrt{m_\varphi^4+\Omega^2}}{2}\right) & -g_{\varphi\gamma}B_0\omega \\ -g_{\varphi\gamma}B_0\omega & \frac{m_\varphi^2+\sqrt{m_\varphi^4+\Omega^2}}{2} \end{pmatrix} \begin{pmatrix} \varphi \\ A \end{pmatrix} = \begin{pmatrix} P_1 \\ P_2 \end{pmatrix} \tag{B.4}$$

where $P_{1,2}$ are the propagating states. These have phases $k_{1,2}z - \omega t$ respectively.

We consider the boundary conditions such that we start with purely a laser beam prior to propagation into the background magnetic field

$$\varphi(0,0) = 0 \tag{B.5}$$

$$\mathbf{A}(0,0) = A. \tag{B.6}$$

This allows us to express our propagating states in terms of the laser wave vector A

$$P_1 = -\left(ig_{\varphi\gamma}B_0\omega\right)A \tag{B.7}$$

$$P_2 = i\left(\frac{m_\varphi^2+\sqrt{m_\varphi^4+\Omega^4}}{2}\right)A, \tag{B.8}$$

which in turn allows us to express the axion field, at general positions, in terms of the laser and an oscillation coming from the phase difference between the propagating states

$$\varphi = ig_{\varphi\gamma}B_0\omega A\left(\frac{m_\varphi^2+\sqrt{m_\varphi^4+\Omega^2}}{m_\varphi^4+\Omega^2+m_\varphi^2\sqrt{m_\varphi^4+\Omega^2}}\right)\left(e^{i\Theta_1}-e^{i\Theta_2}\right). \tag{B.9}$$

The axion field squared and consequently produced number flux can then be shown to be the following

$$|\mathcal{R}e\{\varphi\}|^2 = \frac{\Omega^4 |A|^2}{4\left(m_\varphi^4 + \Omega^4\right)} \left[1 - \cos(\delta\Theta)\right] \tag{B.10}$$

$$N_\varphi = N_A \frac{\Omega^4 k}{2\omega\left(m_\varphi^4 + \Omega^4\right)} \left[1 - \cos(\delta\Theta)\right]. \tag{B.11}$$

Explicitly, the phase difference is shown below where we have used the binomial expansion to approximate the solution

$$\frac{\delta\Theta}{z} = k_1 - k_2 \tag{B.12}$$

$$\frac{\delta\Theta}{z} = \sqrt{\frac{2\omega^2 - m_\varphi^2 - \sqrt{m_\varphi^4 + \Omega^4}}{2}} - \sqrt{\frac{2\omega^2 - m_\varphi^2 + \sqrt{m_\varphi^4 + \Omega^4}}{2}} \tag{B.13}$$

$$\frac{\delta\Theta}{z} = \sqrt{\frac{2\omega^2 - m_\varphi^2}{2}} \left[\sqrt{1-x} - \sqrt{1+x}\right] \tag{B.14}$$

$$\frac{\delta\Theta}{z} \approx \frac{1}{\sqrt{2}} \sqrt{\frac{m_\varphi^4 + \Omega^4}{2\omega^2 - m_\varphi^2}} \tag{B.15}$$

$$\text{where} \quad x = \frac{\sqrt{m_\varphi^4 + \Omega^4}}{\left(2\omega^2 - m_\varphi^2\right)}. \tag{B.16}$$

The produced flux in the small angle limit, $\delta\Theta \ll 1$ is

$$N_\varphi = N_A \frac{\omega}{k} \left(\frac{g_{\varphi\gamma} B z}{2}\right)^2 \tag{B.17}$$

where, in this limit the modified wavenumber is

$$k \approx \sqrt{\frac{2\omega^2 - m_\varphi^2}{2}}. \tag{B.18}$$

This is exactly the commonly quoted result in the literature (2.10).

B.1.1 Deriving the evolution equations

Here we demonstrate a fuller calculation of the evolution equations. We explicitly show the derivation for the evolution equations of both laser fields **A** and **a**. We note that if the resonance conditions and vacuum free space conditions are applied from the onset, the derivation simplifies considerably. We begin with equation (4.15) and substitute in equations (4.18 – 4.20). The left hand term yields

$$\begin{aligned}\Box\mathbf{A}_T = \frac{1}{2}\Bigg[\hat{y}\left(\overbrace{A_{,tt} - A_{,zz}}^{\text{from SVEA=0}} - 2i\omega_A A_{,t} - 2ik_A A_{,z} + \overbrace{\left(k_A^2 - \omega_A^2\right)}^{\text{from free space=0}}\right)e^{i\theta_A} + CC \\ \hat{x}\left(\overbrace{a_{,tt} - a_{,zz}}^{\text{from SVEA=0}} - 2i\omega_a a_{,t} - 2ik_a a_{,z} + \overbrace{\left(k_a^2 - \omega_a^2\right)}^{\text{from free space=0}}\right)e^{i\theta_A} + CC\Bigg].\end{aligned} \tag{B.19}$$

The first term on the right-hand side of equation (4.15) gives,

$$\begin{aligned}\nabla\hat{\varphi}\times\mathbf{A}_{T,t} = \frac{1}{2}\hat{z}\left[\left(\varphi_{,z} + ik_\varphi\varphi\right)e^{i\theta_\varphi}\right]\times\frac{1}{2}\Big[\hat{y}\left(-i\omega_A A + A_{,t}\right)e^{i\theta_A} + CC+ \\ \hat{x}\left(-i\omega_a a + a_{,t}\right)e^{i\theta_a} + CC\Big].\end{aligned} \tag{B.20}$$

Similarly, the second term on the right-hand side of the equation (4.15) gives,

$$\begin{aligned}\hat{\varphi}_{,t}\nabla\times\mathbf{A}_T = \left[\left(-i\omega_\varphi\varphi_{,t} + \varphi_{,t}\right)e^{i\theta_\varphi} + CC\right]\times\frac{1}{2}\Big[\hat{z}\times\hat{y}\big(\left(-i\omega_A A_{,z} + A_{,z}\right)e^{i\theta_A} + CC\big) \\ \hat{z}\times\hat{x}\big(\left(i\omega_a a + a_{,z}\right)e^{i\theta_a} + CC\big)\end{aligned} \tag{B.21}$$

. Putting all of these together and keeping only the resonant terms will result in the evolution equations for both the laser fields. From out resonance condition $\omega_\varphi = \omega_A + \omega_a$ we can see that, for the evolution of the background laser field we must take the products of the field $\hat{\varphi}$ with the conjugate on the probe laser field

$\mathbf{a}^*$, and likewise, to obtain the evolution equation for the probe laser field take the products $\hat{\varphi}$ and $\mathbf{A}^*$.

For the evolution of the background laser field we have,

$$\Box\mathbf{A} = g_{\varphi\gamma}\left[\left(\nabla\hat{\varphi}\times\mathbf{a}^*_{,t}\right) - \hat{\varphi}_{,t}\nabla\times\mathbf{a}^*\right] \tag{B.22}$$

$$\begin{aligned}\hat{\mathbf{y}}\left(\omega_A A_, t + k_A A_{,z}\right) =& \hat{\mathbf{y}}\frac{g_{\varphi\gamma}i}{4}\left[-\varphi a^* k_\varphi \omega_a + i\left(k_\varphi \varphi a^*_{,t} + \omega_a a^* \varphi_{,z}\right) + \varphi_{,z} a^*_{,t}\right] \\ &+ \hat{\mathbf{y}}\frac{g_{\varphi\gamma}i}{4}\left[\varphi a^* \omega_a \omega_\varphi + i\left(\omega_\varphi \varphi a^*_{,z} + \omega_a a^* \varphi_{,t}\right) - \varphi_{,t} a^*_{,z}\right]].\end{aligned} \tag{B.23}$$

For the probe field we have

$$\Box\mathbf{a} = g_{\varphi\gamma}\left[\left(\nabla\hat{\varphi}\times\mathbf{A}^*_{,t}\right) - \hat{\varphi}_{,t}\nabla\times\mathbf{A}^*\right] \tag{B.24}$$

$$\begin{aligned}\hat{\mathbf{x}}\left(\omega_a a_, t + k_a a_{,z}\right) =& -\hat{\mathbf{x}}\frac{g_{\varphi\gamma}i}{4}\left[-\varphi A^* k_\varphi \omega_A + i\left(k_\varphi \varphi A^*_{,t} + \omega_A A^* \varphi_{,z}\right) + \varphi_{,z} A^*_{,t}\right] \\ &- \hat{\mathbf{x}}\frac{g_{\varphi\gamma}i}{4}\left[-\varphi A^* \omega_A \omega_\varphi + i\left(\omega_\varphi \varphi A^*_{,z} - \omega_A A^* \varphi_{,t}\right) - \varphi_{,t} A^*_{,z}\right]\end{aligned} \tag{B.25}$$

Appendix C

Appendix

C.1 Momentum and potentials

We can use the Lorentz force equation (C.1) to derive an expression between the electron's momentum ($\mathbf{p}$) and the vector 3 potential ($\mathbf{A}$).

$$\frac{d\boldsymbol{p}}{dt} = -e\left(E + v \times B\right) \tag{C.1}$$

where $\frac{d}{dt} = \partial_t\left(\right) + v \cdot \left(\nabla\right)$.

$$\begin{aligned}
\frac{d\boldsymbol{p}}{dt} =& -e\left(-\nabla\Phi - \partial_t\mathbf{A} + \nabla_A\left(v \cdot \mathbf{A}\right) - \left(v \cdot \nabla\right)\mathbf{A}\right) && \text{(C.2)}\\
=& e\frac{dA}{dt} + \cancel{-e\left(\nabla_A\left(v \cdot \mathbf{A}\right) - \nabla\Phi\right)} && \text{(C.3)}\\
\mathbf{p} =& e\mathbf{A} && \text{(C.4)}
\end{aligned}$$

where in the last line we have chosen a suitable gauge to let the bracket of the right go to zero. If we consider the electromagnetic 4 potential $A^\mu = (\Phi, \mathbf{A})$ and the electron 4 momentum $p^\mu = (\mathcal{E}, \boldsymbol{p})$, we can obtain a relation between the electric potential and electron's energy, $\mathcal{E} = e\Phi$.

C.2 Derivation of the plasma wave oscillator equation

To derive an expression for the axion wave where the axion is sourced from the maximum electric field of the plasma wave we start with the inhomogeneous Maxwell's equations. We use them to derive the non-linear electron density and oscillator equation.

The inhomogeneous Maxwell's equations for our set up, namely a 1-D problem in which solutions depend only on ζ, where $\zeta = x - \beta t$, are

$$\nabla \cdot \boldsymbol{E} = e(n_0 - n_e) \tag{C.5}$$

$$-\mathcal{E}'' + \beta p'' = e^2(n_0 - n_e) \tag{C.6}$$

$$\nabla \times \boldsymbol{B} = \partial_t \boldsymbol{E} - e n_e v \tag{C.7}$$

$$-\beta\mathcal{E}'' + \beta^2 p'' = - e^2 n_e v, \tag{C.8}$$

where we have made use of a relation relating the electron energy $\mathcal{E}$ to the scalar potential Φ ($\mathcal{E} = e\Phi$) as well as the vector potential A to the electrons momentum p ($p = eA$) - equation (C.4) derived above. Additionally, we have used the notation F' to represent the derivative of F with respect to ζ.

Substituting equation (C.8) into (C.6) yields the electron density

$$n_e = \frac{\beta n_0}{\beta - v_x}, \tag{C.9}$$

where β is the phase velocity of the plasma wave and v_x is the electron velocity in the x direction.

The analysis requires us to be below the wave breaking limit and as such we must have $v_x < \beta$. For $v_x > \beta$ our model breaks down as the density becomes negative. As the electrons approach the wave velocity, their density drastically increases.

The variable in which the oscillator equation will be derived, ξ is defined as $\xi = \Gamma - \beta U$ where $\Gamma = (1-v^2)^{-\frac{1}{2}}$ is the Lorentz factor for the electrons and $U = \Gamma v$ is the momentum of the electrons normalized over mass. This is a dimensionless parameter and can be seen to be related to the electron energy in the wave frame (this is clear from multiplying them by $\gamma = (1-\beta^2)^{-\frac{1}{2}}$ and noting that they take the form of Lorentz boosts - note that this is needed to match equation (5.2) to the equivalent form found in [77]). Another dimensionless parameter (that will aid in the derivation) which is related to the electrons momentum in the wave frame is defined as $\Lambda = \beta\Gamma - U$. We want to be able to express some combination of these in terms of the gamma factor γ such that, by rearranging, our equations will be in terms of the electrons' energy (ξ) and the wave's γ. We can achieve this by looking at the difference in the squares of ξ and Λ,

$$\xi^2 - \Lambda^2 = \Gamma^2 + \beta^2 U^2 - \beta^2\Gamma^2 - U^2 \tag{C.10}$$

$$\xi^2 - \Lambda^2 = \frac{(\Gamma^2 - U^2)}{\gamma^2} \tag{C.11}$$

$$\xi^2 - \Lambda^2 = \gamma^{-2} \tag{C.12}$$

where in the last line we have use the fact that $U = \Gamma v$ and $\Gamma = (1-v^2)^{-\frac{1}{2}}$

We therefore have:

$$\Lambda = \pm\sqrt{\xi^2 - \gamma^{-2}}. \tag{C.13}$$

We would like a way to express the charge density ρ in terms of ξ and γ also. If we notice that the charge density is proportional to $\frac{U}{\beta\Gamma - U}$ we can then use

(C.13) to express each Γ and U in terms of ξ and γ

$$\xi - \beta\Lambda = \Gamma - \beta U - \beta^2\Gamma + \beta U = \Gamma\gamma^{-2} \tag{C.14}$$
$$\Gamma = \gamma^2\left(\xi - \beta\sqrt{\xi^2 - \gamma^{-2}}\right), \tag{C.15}$$
$$\beta\xi - \Lambda = \beta\Gamma - \beta^2 U + \beta\Gamma + U = U\gamma^{-2} \tag{C.16}$$
$$U = \gamma^2\left(\beta\xi - \sqrt{\xi^2 - \gamma^{-2}}\right), \tag{C.17}$$
$$\frac{U}{\beta\Gamma - U} = \frac{\gamma^2\left(\beta\xi - \sqrt{\xi^2 - \gamma^{-2}}\right)}{\sqrt{\xi^2 - \gamma^{-2}}} \tag{C.18}$$
$$= \gamma^2\left(\frac{\beta\xi}{\sqrt{\xi^2 - \gamma^{-2}}} - 1\right). \tag{C.19}$$

Using the above calculations one can now express the inhomogeneous Maxwell's equation ($\nabla \cdot E = \rho$) as:

$$\xi'' = \omega_p^2\gamma^2\left(\frac{\beta\xi}{\sqrt{\xi^2 - \gamma^{-2}}} - 1\right), \tag{C.20}$$

which from multiplying through by ξ' and integrating, more clearly illustrates it as an oscillator equation. First we note the following two relations:

$$\frac{1}{2}\left(\xi'^2\right)' = \xi''\xi' \tag{C.21}$$
$$\left(\sqrt{\xi^2 - \gamma^{-2}}\right)' = \frac{\xi\xi'}{\sqrt{\xi^2 - \gamma^{-2}}}. \tag{C.22}$$

Therefore after integrating we have

$$\frac{1}{2}\left(\xi'\right)^2 + \omega_p^2\gamma^2\left(\xi - \beta\sqrt{\xi^2 - \gamma^{-2}}\right) = C. \tag{C.23}$$

We want C to correspond to the largest amplitude oscillation. For this the square root must be minimized, therefore $\xi = \gamma^{-1}$, when $\xi' = 0$, hence $C = \omega_p^2\gamma$.

In order to determine the maximum electric field, we must first calculate the value of ξ at which this occurs. Equation (C.20) can be though of as an equation for the restoring force of the oscillation. Consequently the value of ξ for which equation (C.20) is equal to zero corresponds to the maximum electric field ($\xi = 1$). Equation (5.2) can then be substituted into equation (5.1) and solved to calculated the maximum electric field

$$\frac{1}{2}\frac{e^2}{m_e^2}E_{max}^2 = \omega_p^2\gamma - \omega^2\gamma^2\left(1 - \beta\sqrt{1-\gamma^{-2}}\right) \tag{C.24}$$

$$E_{max} = \frac{\omega_p m_e}{e}\sqrt{2(\gamma-1)}. \tag{C.25}$$

This is referred to as the cold relativistic wave-breaking field [81] and is the maximum electric field achievable for a one-dimensional cold plasma.

C.2.1 The wavelength of the oscillation

Due to the periodic nature of the plasma waves' electric field, ξ and similarly the axion will also have the same periodicity, and can both be described using Fourier series

$$\xi = \sum_n \xi_n \exp\left(2\pi i n \frac{\zeta}{\lambda}\right) \tag{5.7 Revisited}$$

The wavelength of the oscillation will be double the length between the extremes of the oscillator equation - these occur at $\xi = \gamma^{-1}$ and $\xi = \gamma(1+\beta^2)$. The oscillator equation can be solved for $\zeta(\xi)$ and we can integrate between these two points. However, as we are envisioning scenarios in which $\gamma \gg 1$ it is convenient to use scaled variables in the integration in order to solve it

$$\zeta(\xi) = \int_{\gamma^{-2}}^{\bar{\xi}} \frac{1}{\sqrt{2\gamma}\omega_p} \frac{\gamma}{\sqrt{\left(\gamma^{-2} - \bar{\chi} + \sqrt{1-\gamma^{-2}}\sqrt{\bar{\chi}^2 - \gamma^{-4}}\right)}} d\bar{\chi}. \tag{C.26}$$

We have introduced the scaled dummy variable $\bar{\chi} = \gamma^{-1}\chi$ to allow us to integrate more easily and we have additionally used the scaled variable $\bar{\xi} = \gamma^{-1}\xi$.

Before integrating we can simplify by neglecting terms of $\mathcal{O}(\gamma^{-4})$ and power expand out the terms in the square root

$$\zeta(\xi) = \sqrt{\frac{\gamma}{2}} \frac{1}{\omega_p} \int_{\gamma^{-2}}^{\bar{\xi}} \frac{1}{\sqrt{1 - \frac{\bar{\chi}}{2}}} d\bar{\chi}. \tag{C.27}$$

Taking the wavelength to be twice ζ when evaluated between the limits, the wavelength is

$$\lambda = \frac{4\sqrt{2\gamma}}{\omega_p} \tag{C.28}$$

where we have let $\beta \to 1$.

We can use this to calculate the coefficient of the Fourier series (equation (5.7))

$$\xi_n = \frac{1}{\lambda} \int_0^{\lambda} \xi(\zeta) e^{-\frac{2\pi i n \zeta}{\lambda}} d\zeta. \tag{C.29}$$

Evaluating the integral yields

$$\xi_{n|n\neq 0} = -\frac{4\gamma}{\pi^2 n^2} \tag{5.9 revisited}$$

$$\xi_0 = \frac{4}{3}\gamma. \tag{5.10 revisited}$$

C.3 The axion Fourier series

Selecting for solutions which are in phase with $\zeta = x - \beta t$, the axion Klein-Gordon equation can be re-expressed in order to find the axion field's (equation (C.32)) Fourier coefficient (equation (C.34))

$$\left(\Box + m_\varphi^2\right)\varphi = -g_{\varphi\gamma} E \cdot B. \tag{C.30}$$

$$\varphi = \frac{g_{\varphi\gamma} m_e B_0}{e m_\varphi^2}\xi' + \frac{1}{\gamma^2 m_\varphi^2}\varphi'' \tag{C.31}$$

where $\Box \to -\frac{1}{\gamma^2}\frac{\partial^2}{\partial\zeta^2}$ as $\gamma = \left(1-\beta^2\right)^{-\frac{1}{2}}$

$$\varphi = \sum_n \varphi_n \exp\left(2\pi i n \frac{\zeta}{\lambda}\right) \tag{C.32}$$

We can then use equation C.31 with the above to determine the axions coefficient:

$$\varphi_n\left(\frac{m_\varphi^2\gamma^2\lambda^2 + 4\pi^2 n^2}{m_\varphi^2\gamma^2\lambda^2}\right) = \frac{g_{\varphi\gamma} B m_e}{\lambda e m_\varphi^2} 2\pi i n \xi_n \tag{C.33}$$

$$\varphi_n = \frac{g_{\varphi\gamma} B m_e \gamma^2 \lambda}{e(4\pi^2 n^2 + m_\varphi^2\gamma^2\lambda^2)} 2\pi i n \xi_n. \tag{C.34}$$

Appendix D

Appendix

D.1 Gamma, Pauli matrices and conserved currents

In the Dirac representation the gamma matrices are as follows:

$$\gamma^0 = \begin{pmatrix} 1 & 0 & 0 & 0 \\ 0 & 1 & 0 & 0 \\ 0 & 0 & -1 & 0 \\ 0 & 0 & 0 & -1 \end{pmatrix},$$

$$\gamma^1 = \begin{pmatrix} 0 & 0 & 0 & 1 \\ 0 & 0 & 1 & 0 \\ 0 & -1 & 0 & 0 \\ -1 & 0 & 0 & 0 \end{pmatrix}, \quad \gamma^2 = \begin{pmatrix} 0 & 0 & 0 & -i \\ 0 & 0 & i & 0 \\ 0 & i & 0 & 0 \\ -i & 0 & 0 & 0 \end{pmatrix}, \quad \gamma^3 = \begin{pmatrix} 0 & 0 & 1 & 0 \\ 0 & 0 & 0 & -1 \\ -1 & 0 & 0 & 0 \\ 0 & 1 & 0 & 0 \end{pmatrix}. \tag{D.1}$$

They can be seen to be represented by 2×2 null matrices in the diagonals and 2×2 Pauli matrices in the off diagonals.

$$\sigma^1 = \begin{pmatrix} 0 & 1 \\ 1 & 0 \end{pmatrix}, \quad \sigma^2 = \begin{pmatrix} 0 & -i \\ i & 0 \end{pmatrix}, \quad \sigma^3 = \begin{pmatrix} 1 & 0 \\ 0 & -1 \end{pmatrix}. \tag{D.2}$$

A further gamma matrix can be defined by

$$\gamma^5 = i\gamma^0\gamma^1\gamma^2\gamma^3 \tag{D.3}$$

$$\gamma^5 = \begin{pmatrix} 0 & \mathbb{I} \\ \mathbb{I} & 0 \end{pmatrix}, \qquad \gamma^0\gamma^5 = \begin{pmatrix} 0 & \mathbb{I} \\ -\mathbb{I} & 0 \end{pmatrix}. \tag{D.4}$$

Given a Dirac field $\psi = (u_1, u_2, u_3, u_4)^T$, a conserved current can be formed from the contraction

$$j^\mu = \bar{\psi}\gamma^\mu\psi \tag{D.5}$$

where $\bar{\psi} = \psi^\dagger\gamma^0$.

Explicitly these components read as

$$j^\mu = \begin{pmatrix} u_1^*u_1 + u_2^*u_2 + u_3^*u_3 + u_4^*u_4 \\ u_4^*u_1 + u_3^*u_2 + u_2^*u_3 + u_1^*u_4 \\ iu_4^*u_1 - iu_3^*u_2 + iu_2^*u_3 - iu_1^*u_4 \\ u_3^*u_1 - u_4^*u_2 + u_1^*u_3 - u_2^*u_4 \end{pmatrix}. \tag{D.6}$$

The charge density and consequently the total charge are related to the zeroth component of j^μ

$$\rho = \quad e\bar{\psi}\gamma^0\psi \tag{D.7}$$

$$Q = \int_V \rho dV. \tag{D.8}$$

D.2 Expanding out the Dirac equation

Expanding out the Dirac equation (6.1) where (6.2) is understood yields two differential equations,

$$(\omega - m_e)\,\Theta = (i\sigma_1 d_x - p_y\sigma_2 - p_z\sigma_3 - eA_y\sigma_2)\,\chi \tag{D.9}$$

$$(\omega + m_e)\,\chi = (i\sigma_1 d_x - p_y\sigma_2 - p_z\sigma_3 - eA_y\sigma_2)\,\Theta \tag{D.10}$$

where we have utilized the Dirac representation for the gamma matrices shown in Section D.1 above.

Eliminating the second of these equations yields a second order differential equation for the positive energy solutions, Θ, which in full reads as,

$$\left(\omega^2 - m_e^2\right)\Theta = (i\sigma_1 d_x - p_y\sigma_2 - p_z\sigma_3 - eA_y\sigma_2)\,(i\sigma_1 d_x - p_y\sigma_2 - p_z\sigma_3 - eA_y\sigma_2)\,\Theta \tag{D.11}$$

$$\left(\omega^2 - m_e^2\right)\Theta = \left(-d_x^2 + p_y^2 + p_z^2 + e^2B_0^2x^2 + 2eB_0xP_y + eB_0\sigma_3\right) \tag{D.12}$$

where in the last line we have used the fact that the asymmetry in the Pauli matrices will cancel most cross terms except from when the derivative in the $\hat{x}$ direction acts on the vector potential component, A_y, as we have $A_y = xB_0$ as our choice for the geometry of the potential.

One can then rearrange such that Θ is the subject of the equation and use the newly defined variable, $\bar{x}$ - equation (6.9), to obtain an equation in the form of the quantum harmonic oscillation such as was done in deriving equation (6.8).

$$\frac{d^2\Theta(\bar{x})}{d\bar{x}^2} + \left(\frac{\Omega^2}{eB_0} - \bar{x}^2\right)\Theta(\bar{x}) = 0 \tag{6.8 Revisited}$$

D.3 Deriving the Greens function

The general solution of the Greens function (6.28) away from the peak of the delta function has the following solutions

$$G(\bar{x}, \bar{x}') = \begin{cases} G_L(\bar{x}, \bar{x}') = A(\bar{x}')e^{\bar{\omega}\bar{x}} + B(\bar{x}')e^{-\bar{\omega}\bar{x}} & \bar{x} < \bar{x}' \\ G_R(\bar{x}, \bar{x}') = C(\bar{x}')e^{\bar{\omega}\bar{x}} + D(\bar{x}')e^{-\bar{\omega}\bar{x}} & \bar{x} > \bar{x}'. \end{cases} \tag{D.13}$$

Our first boundary condition is that at the extremes $\bar{x} \to \pm\infty$ each the left and right hand side of the Greens function goes to zero. This reads as follows,

$$\begin{aligned} G_L(\bar{x}, \bar{x}') =& A(\bar{x}')e^{\bar{\omega}\bar{x}} + B(\bar{x}')e^{-\bar{\omega}\bar{x}} & \text{(D.14)} \\ G_L(-\infty, \bar{x}') =& 0 \qquad \implies B(\bar{x}') = 0 & \text{(D.15)} \end{aligned}$$

$$\begin{aligned} G_R(\bar{x}, \bar{x}') =& C(\bar{x}')e^{\bar{\omega}\bar{x}} + D(\bar{x}')e^{-\bar{\omega}\bar{x}} & \text{(D.16)} \\ G_R(\infty, \bar{x}') =& 0 \qquad \implies C(\bar{x}') = 0. & \text{(D.17)} \end{aligned}$$

As the Greens function is continuous at the boundary, $\bar{x} = \bar{x}'$, we have

$$\begin{aligned} G_L(\bar{x}', \bar{x}') =& G_R(\bar{x}', \bar{x}') & \text{(D.18)} \\ \implies A(\bar{x}') =& D(\bar{x'})e^{-2\bar{\omega}\bar{x}'}. & \text{(D.19)} \end{aligned}$$

The last boundary condition needed to fully specify the Greens function comes from integrating equation (6.28) across some small region 2ϵ which crosses the boundary $\bar{x} = \bar{x}'$

$$\int_{\bar{x}'-\epsilon}^{\bar{x}'+\epsilon} d\bar{x} \frac{\partial^2 G(\bar{x}, \bar{x}')}{\partial \bar{x}^2} = -\omega'^2 \int_{\bar{x}'-\epsilon}^{\bar{x}'+\epsilon} d\bar{x} G(\bar{x}, \bar{x}') + 1. \tag{D.20}$$

The Green's function, as we have stated, must be continuous and thus if we let $\epsilon \to 0$ its integral is consequently zero. However, as we let $\epsilon \to 0$, the LHS of equation (D.20) takes a different value depending on whether we approach $\epsilon = 0$ from above or below. Consequently, as we take the limit $\epsilon \to 0$ equation (D.20) becomes,

$$\delta G_R(\bar{x}, \bar{x}') - \delta G_L(\bar{x}, \bar{x}') = 1 \tag{D.21}$$

where $\delta G(\bar{x}, \bar{x}')$ is the derivative if G with respect to $\bar{x}$ evaluated at $\bar{x} = \bar{x}'$.

Substituting this into equation (D.13) yields

$$-\bar{\omega} D(\bar{x}') e^{-\bar{\omega}\bar{x}'} = \bar{\omega} A(\bar{x}') e^{\bar{\omega}\bar{x}'} + 1 \tag{D.22}$$

$$-1 = 2\bar{\omega} D(\bar{x}') e^{-2\bar{\omega}\bar{x}'} \tag{D.23}$$

$$A(\bar{x}') = -\frac{1}{2\bar{\omega}} e^{-\bar{\omega}\bar{x}'} \qquad D(\bar{x}') = -\frac{1}{2\bar{\omega}} e^{\bar{\omega}\bar{x}'}. \tag{D.24}$$

Combining all this together, the Greens function has the form

$$G(\bar{x}, \bar{x}') = \begin{cases} G_L(\bar{x}, \bar{x}') = -\frac{e^{\bar{\omega}(\bar{x}-\bar{x}')}}{2\bar{\omega}} & \bar{x} < \bar{x}' \\ G_R(\bar{x}, \bar{x}') = -\frac{e^{\bar{\omega}(\bar{x}'-\bar{x})}}{2\bar{\omega}} & \bar{x} > \bar{x}' \end{cases}. \tag{D.25}$$

D.4 The momentum modulation

Here we demonstrate a plot of the momentum modulation, $A(p)$, which we applied to the Dirac field in Section 6.6.2.

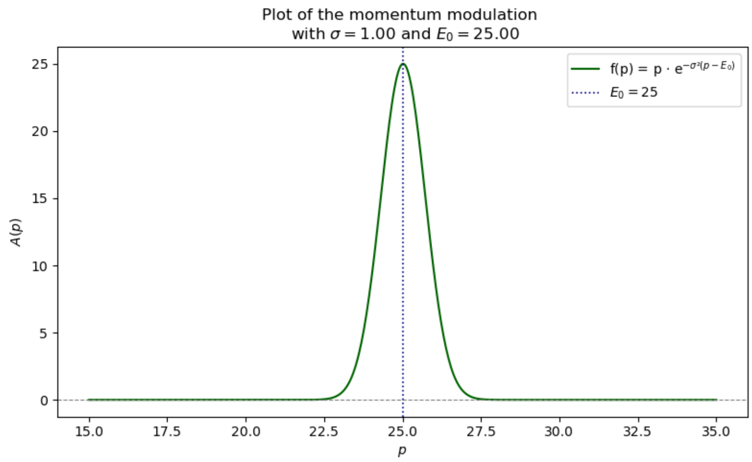

Figure D.1: The plot of the modulation applied to the longitudinal momentum of the electrons. This was chosen for its mathematical convenience whilst have a Gaussian-like shape.

D.5 The transverse modes of the axion field

From equation (6.45) we have

$$I_p(\bar{x}) = \frac{\bar{\omega}}{2} I_{p-1} + \frac{p-1}{2} I_{p-2} - \frac{e^{\bar{\omega}\bar{x}} \bar{x}^{p-1} e^{-\bar{x}^2}}{2}. \tag{D.26}$$

The first 5 iterations of the recursion are

$$
\begin{aligned}
I_0 =& \quad \frac{\sqrt{\pi}}{2}\left(1+\operatorname{erf}\left(\bar{x}-\frac{\bar{\omega}}{2}\right)\right)e^{\frac{\bar{\omega}^2}{4}} && \text{(D.27)}\\
I_1 =& \quad \frac{\sqrt{\pi}}{4}\bar{\omega}\left(1+\operatorname{erf}\left(\bar{x}-\frac{\bar{\omega}}{2}\right)\right)e^{\frac{\bar{\omega}^2}{4}}-\frac{e^{-\bar{x}(\bar{x}-\bar{\omega})}}{2} && \text{(D.28)}\\
I_2 =& e^{\frac{\bar{\omega}^2}{4}}\left[\frac{\sqrt{\pi}}{2}\left(1+\operatorname{erf}\left(\bar{x}-\frac{\bar{\omega}}{2}\right)\right)\left(\frac{\bar{\omega}^2}{4}+\frac{1}{2}\right)\right]-\frac{e^{-\bar{x}(\bar{x}-\bar{\omega})}}{2}\left(\bar{x}+\frac{\bar{\omega}}{2}\right) && \text{(D.29)}\\
I_3 =& e^{\frac{\bar{\omega}^2}{4}}\left[\frac{\sqrt{\pi}}{2}\left(1+\operatorname{erf}\left(x-\frac{\bar{\omega}}{2}\right)\right)\left(\frac{\bar{\omega}^3}{8}+\frac{3\bar{\omega}}{4}\right)\right]\\
&-\frac{e^{-\bar{x}(\bar{x}-\bar{\omega})}}{2}\left(\bar{x}^2+\frac{\bar{x}\bar{\omega}}{2}+\frac{\bar{\omega}^2}{4}+1\right) && \text{(D.30)}\\
I_4 =& e^{\frac{\bar{\omega}^2}{4}}\left[\frac{\sqrt{\pi}}{2}\left(1+\operatorname{erf}\left(x-\frac{\bar{\omega}}{2}\right)\right)\left(\frac{\bar{\omega}^4}{16}+\frac{3\bar{\omega}^2}{4}+\frac{3}{4}\right)\right]\\
&-\frac{e^{-\bar{x}(\bar{x}-\bar{\omega})}}{2}\left(\bar{x}^3+\frac{\bar{x}^2\bar{\omega}}{2}+\frac{\bar{x}\bar{\omega}^2}{4}+\frac{3\bar{x}}{2}+\frac{\bar{\omega}^3}{8}+\frac{5\bar{\omega}}{4}\right). && \text{(D.31)}
\end{aligned}
$$

Utilizing these in conjunction with equation (6.48) gives the first two axion modes

$$\begin{aligned}\varphi(\bar{x})|_{p=0} =& -\frac{1}{2\bar{\omega}}\left[e^{-\bar{\omega}\bar{x}}\left[\frac{\sqrt{\pi}}{2}\left(1+\operatorname{erf}\left(\bar{x}-\frac{\bar{\omega}}{2}\right)\right)e^{\frac{\bar{\omega}^2}{4}}\right]\right.\\ &\left.+(-1)^0 e^{\bar{\omega}\bar{x}}\left[\frac{\sqrt{\pi}}{2}\left(1+\operatorname{erf}\left(-\bar{x}-\frac{\bar{\omega}}{2}\right)\right)e^{\frac{\bar{\omega}^2}{4}}\right]\right]\end{aligned} \tag{D.32}$$

$$\varphi(\bar{x})|_{p=0} =\frac{\sqrt{\pi}}{4\bar{\omega}}\left[\operatorname{erf}(+)e^{\bar{\omega}\bar{x}}-\operatorname{erf}(-)e^{-\bar{\omega}\bar{x}}-2\cosh(\bar{\omega}\bar{x})\right]e^{\frac{\bar{\omega}^2}{4}} \tag{D.33}$$

$$\begin{aligned}\varphi(\bar{x})|_{p=1} =& -\frac{1}{2\bar{\omega}}\left[e^{-\bar{\omega}\bar{x}}\left[\frac{\sqrt{\pi}}{4}\bar{\omega}\left(1+\operatorname{erf}\left(\bar{x}-\frac{\bar{\omega}}{2}\right)\right)e^{\frac{\bar{\omega}^2}{4}}-\frac{e^{-\bar{x}(\bar{x}-\bar{\omega})}}{2}\right]\right.\\ &\left.+(-1)^1 e^{\bar{\omega}\bar{x}}\left[\frac{\sqrt{\pi}}{4}\bar{\omega}\left(1+\operatorname{erf}\left(-\bar{x}-\frac{\bar{\omega}}{2}\right)\right)e^{\frac{\bar{\omega}^2}{4}}-\frac{e^{\bar{x}(-\bar{x}-\bar{\omega})}}{2}\right]\right]\end{aligned} \tag{D.34}$$

$$\varphi(\bar{x})|_{p=1} =\frac{\sqrt{\pi}}{8}\left[2\sinh(\bar{\omega}\bar{x})-\operatorname{erf}(+)e^{\bar{\omega}\bar{x}}-\operatorname{erf}(-)e^{-\bar{\omega}\bar{x}}\right]e^{\frac{\bar{\omega}^2}{4}} \tag{D.35}$$

$$\begin{aligned}\varphi(\bar{x})|_{p=2} =& -\frac{1}{2\bar{\omega}}\left[e^{-\bar{\omega}\bar{x}}\left[e^{\frac{\bar{\omega}^2}{4}}\left[\frac{\sqrt{\pi}}{2}\left(1+\operatorname{erf}\left(\bar{x}-\frac{\bar{\omega}}{2}\right)\right)\left(\frac{\bar{\omega}^2}{4}+\frac{1}{2}\right)\right]\right.\right.\\ &\left.-\frac{e^{-\bar{x}(\bar{x}-\bar{\omega})}}{2}\left(\bar{x}+\frac{\bar{\omega}}{2}\right)\right]\\ &+(-1)^2 e^{\bar{\omega}\bar{x}}\left[e^{\frac{\bar{\omega}^2}{4}}\left[\frac{\sqrt{\pi}}{2}\left(1+\operatorname{erf}\left(-\bar{x}-\frac{\bar{\omega}}{2}\right)\right)\left(\frac{\bar{\omega}^2}{4}+\frac{1}{2}\right)\right]\right.\\ &\left.\left.-\frac{e^{\bar{x}(-\bar{x}-\bar{\omega})}}{2}\left(-\bar{x}+\frac{\bar{\omega}}{2}\right)\right]\right]\end{aligned} \tag{D.36}$$

$$\varphi(x)|_{p=2} =\frac{\sqrt{\pi}}{4\bar{\omega}}\left(\frac{\bar{\omega}^2}{4}+\frac{1}{2}\right)\left[\operatorname{erf}(+)e^{\bar{\omega}x}-\operatorname{erf}(-)e^{-\bar{\omega}x}-2\cosh(\bar{\omega}x)\right]e^{\frac{\bar{\omega}^2}{4}}+\frac{e^{-x^2}}{4} \tag{D.37}$$

$$\begin{aligned}\varphi(\bar{x})|_{p=3} =& -\frac{1}{2\bar{\omega}}\left[e^{-\bar{\omega}\bar{x}}\left[e^{\frac{\bar{\omega}^2}{4}}\left[\frac{\sqrt{\pi}}{2}\left(1+\operatorname{erf}\left(\bar{x}-\frac{\bar{\omega}}{2}\right)\right)\left(\frac{\bar{\omega}^3}{8}+\frac{3\bar{\omega}}{4}\right)\right]\right.\right.\\ &\left.-\frac{e^{-\bar{x}(\bar{x}-\bar{\omega})}}{2}\left(\bar{x}^2+\frac{\bar{x}\bar{\omega}}{2}+\frac{\bar{\omega}^2}{4}+1\right)\right]\\ &+(-1)^3 e^{\bar{\omega}\bar{x}}\left[e^{\frac{\bar{\omega}^2}{4}}\left[\frac{\sqrt{\pi}}{2}\left(1+\operatorname{erf}\left(-x-\frac{\bar{\omega}}{2}\right)\right)\left(\frac{\bar{\omega}^3}{8}+\frac{3\bar{\omega}}{4}\right)\right]\right.\\ &\left.\left.-\frac{e^{\bar{x}(-\bar{x}-\bar{\omega})}}{2}\left(\bar{x}^2-\frac{\bar{x}\bar{\omega}}{2}+\frac{\bar{\omega}^2}{4}+1\right)\right]\right] \qquad \text{(D.38)}\end{aligned}$$

$$\varphi(\bar{x})|_{p=3} = \frac{\sqrt{\pi}}{4\bar{\omega}}\left(\frac{\bar{\omega}^3}{8}+\frac{3\bar{\omega}}{4}\right)\left[2\sinh(\bar{\omega}\bar{x})-\operatorname{erf}(+)e^{\bar{\omega}\bar{x}}-\operatorname{erf}(-)e^{-\bar{\omega}\bar{x}}\right]e^{\frac{\bar{\omega}^2}{4}}+\frac{e^{-\bar{x}^2}}{4}\bar{x}. \qquad \text{(D.39)}$$

$$\begin{aligned}\varphi(\bar{x})_{p=4} =& = -\frac{1}{2\bar{\omega}}\left[e^{-\bar{\omega}\bar{x}}\left[e^{\frac{\bar{\omega}^2}{4}}\left[\frac{\sqrt{\pi}}{2}\left(1+\operatorname{erf}\left(\bar{x}-\frac{\bar{\omega}}{2}\right)\right)\left(\frac{\bar{\omega}^4}{16}+\frac{3\bar{\omega}^2}{4}+\frac{3}{4}\right)\right]\right.\right.\\ &\left.-\frac{e^{-\bar{x}(\bar{x}-\bar{\omega})}}{2}\left(\bar{x}^3+\frac{\bar{x}^2\bar{\omega}}{2}+\frac{\bar{x}\bar{\omega}^2}{4}+\frac{3\bar{x}}{2}+\frac{\bar{\omega}^3}{8}+\frac{5\bar{\omega}}{4}\right)\right]\\ &+(-1)^4 e^{\bar{\omega}\bar{x}}\left[e^{\frac{\bar{\omega}^2}{4}}\left[\frac{\sqrt{\pi}}{2}\left(1+\operatorname{erf}\left(-\bar{x}-\frac{\bar{\omega}}{2}\right)\right)\left(\frac{\bar{\omega}^4}{16}+\frac{3\bar{\omega}^2}{4}+\frac{3}{4}\right)\right]\right.\\ &\left.\left.-\frac{e^{\bar{x}(-\bar{x}-\bar{\omega})}}{2}\left(-\bar{x}^3+\frac{\bar{x}^2\bar{\omega}}{2}-\frac{\bar{x}\bar{\omega}^2}{4}-\frac{3\bar{x}}{2}+\frac{\bar{\omega}^3}{8}+\frac{5\bar{\omega}}{4}\right)\right]\right] \qquad \text{(D.40)}\end{aligned}$$

$$\begin{aligned}\varphi(\bar{x})_{p=4} =& \frac{\sqrt{\pi}}{4\bar{\omega}}\left(\frac{\bar{\omega}^4}{16}+\frac{3\bar{\omega}^2}{4}+\frac{3}{4}\right)\left[\operatorname{erf}(+)e^{\bar{\omega}\bar{x}}-\operatorname{erf}(-)e^{-\bar{\omega}\bar{x}}-2\cosh(\bar{\omega}\bar{x})\right]e^{\frac{\bar{\omega}^2}{4}}\\ &+\frac{e^{-\bar{x}^2}}{2}\left(\frac{\bar{x}^2}{2}+\frac{\bar{\omega}^2}{8}+\frac{5}{4}\right) \qquad \text{(D.41)}\end{aligned}$$

Bibliography

[1] A. Riotto and M. Trodden, "Recent progress in baryogenesis," *Annual Review of Nuclear and Particle Science*, vol. 49, no. 1, p. 35–75, 1999.

[2] F. Zwicky, "Republication of: The redshift of extragalactic nebulae," *General Relativity and Gravitation*, vol. 41, no. 1, p. 207–224, 2009.

[3] V. C. Rubin, J. Ford, W. K., and N. Thonnard, "Rotational properties of 21 SC galaxies with a large range of luminosities and radii, from NGC 4605 (R=4kpc) to UGC 2885 (R=122kpc).," , vol. 238, pp. 471–487, June 1980.

[4] F. Zwicky, "On the Masses of Nebulae and of Clusters of Nebulae," , vol. 86, p. 217, Oct. 1937.

[5] J. A. Frieman, M. S. Turner, and D. Huterer, "Dark energy and the accelerating universe," *Annual Review of Astronomy and Astrophysics*, vol. 46, no. 1, p. 385–432, 2008.

[6] M. Kowalski, D. Rubin, G. Aldering, R. J. Agostinho, A. Amadon, R. Amanullah, C. Balland, K. Barbary, G. Blanc, P. J. Challis, and et al., "Improved cosmological constraints from new, old, and combined supernova data sets," *The Astrophysical Journal*, vol. 686, no. 2, p. 749–778, 2008.

[7] P. A. R. Ade, N. Aghanim, M. Arnaud, M. Ashdown, J. Aumont, C. Baccigalupi, A. J. Banday, R. B. Barreiro, J. G. Bartlett, and N. e. a. Bartolo, "Planck 2015 results," *Astronomy & Astrophysics*, vol. 594, p. A13, 2016.

[8] Y. Fukuda, T. Hayakawa, E. Ichihara, K. Inoue, K. Ishihara, H. Ishino, Y. Itow, T. Kajita, J. Kameda, S. Kasuga, and et al., "Measurement of the flux and zenith-angle distribution of upward throughgoing muons by super-kamiokande," *Physical Review Letters*, vol. 82, no. 13, p. 2644–2648, 1999.

[9] Q. R. Ahmad, R. C. Allen, T. C. Andersen, J. D.Anglin, J. C. Barton, E. W. Beier, M. Bercovitch, J. Bigu, S. D. Biller, R. A. Black, and et al., "Direct evidence for neutrino flavor transformation from neutral-current interactions in the sudbury neutrino observatory," *Physical Review Letters*, vol. 89, no. 1, 2002.

[10] K. Eguchi, S. Enomoto, K. Furuno, J. Goldman, H. Hanada, H. Ikeda, K. Ikeda, K. Inoue, K. Ishihara, W. Itoh, and et al., "First results from kamland: Evidence for reactor antineutrino disappearance," *Physical Review Letters*, vol. 90, no. 2, 2003.

[11] J. Jaeckel and A. Ringwald, "The low-energy frontier of particle physics," *Annual Review of Nuclear and Particle Science*, vol. 60, no. 1, p. 405–437, 2010.

[12] A. Boyarsky, M. Drewes, T. Lasserre, S. Mertens, and O. Ruchayskiy, "Sterile neutrino dark matter," *Progress in Particle and Nuclear Physics*, vol. 104, p. 1–45, 2019.

[13] G. Jungman, M. Kamionkowski, and K. Griest, "Supersymmetric dark matter," *Physics Reports*, vol. 267, no. 5, pp. 195–373, 1996.

[14] R. D. Peccei and H. R. Quinn, "CP conservation in the presence of pseudoparticles," *Physical Review Letters*, vol. 38, no. 25, p. 1440–1443, 1977.

[15] R. D. Peccei and H. R. Quinn, "Constraints imposed by CP conservation in the presence of pseudoparticles," *Physical Review D*, vol. 16, no. 6, p. 1791–1797, 1977.

[16] S. Weinberg, "A new light boson?," *Physical Review Letters*, vol. 40, no. 4, p. 223–226, 1978.

[17] F. Wilczek, "Problem of strong P and T invariance in the presence of instatons," *Physical Review Letters*, vol. 40, no. 5, p. 279–282, 1978.

[18] J. E. Kim and G. Carosi, "Axions and the strong CP problem," *Rev. Mod. Phys.*, vol. 82, pp. 557–601, Mar 2010.

[19] D. A. Palken, B. M. Brubaker, M. Malnou, S. A. Kenany, K. M. Backes, S. B. Cahn, Y. V. Gurevich, S. K. Lamoreaux, S. M. Lewis, R. H. Maruyama, N. M. Rapidis, J. R. Root, M. Simanovskaia, T. M. Shokair, S. Singh, D. H. Speller, I. Urdinaran, K. van Bibber, L. Zhong, and K. W. Lehnert, "Improved analysis framework for axion dark matter searches," *Phys. Rev. D*, vol. 101, p. 123011, Jun 2020.

[20] B. Majorovits *et al.*, "MADMAX: A new road to axion dark matter detection," *J. Phys. Conf. Ser.*, vol. 1342, no. 1, p. 012098, 2020.

[21] T. Braine, R. Cervantes, N. Crisosto, N. Du, S. Kimes, L. J. Rosenberg, G. Rybka, J. Yang, D. Bowring, A. S. Chou, R. Khatiwada, A. Sonnenschein, W. Wester, G. Carosi, N. Woollett, L. D. Duffy, R. Bradley, C. Boutan, M. Jones, B. H. LaRoque, N. S. Oblath, M. S. Taubman, J. Clarke, A. Dove, A. Eddins, S. R. O'Kelley, S. Nawaz, I. Siddiqi, N. Stevenson, A. Agrawal, A. V. Dixit, J. R. Gleason, S. Jois, P. Sikivie, J. A. Solomon, N. S. Sullivan, D. B. Tanner, E. Lentz, E. J. Daw, J. H. Buckley, P. M. Harrington, E. A. Henriksen, and K. W. Murch, "Extended search for the invisible axion with the axion dark matter experiment," *Phys. Rev. Lett.*, vol. 124, p. 101303, Mar 2020.

[22] S. J. Asztalos, G. Carosi, C. Hagmann, D. Kinion, K. van Bibber, M. Hotz, L. J. Rosenberg, G. Rybka, J. Hoskins, J. Hwang, P. Sikivie, D. B. Tanner,

R. Bradley, and J. Clarke, "Squid-based microwave cavity search for dark-matter axions," *Phys. Rev. Lett.*, vol. 104, p. 041301, Jan 2010.

[23] L. J. Rosenberg, "Dark-matter QCD-axion searches," *Proceedings of the National Academy of Sciences*, vol. 112, no. 40, p. 12278–12281, 2015.

[24] C. O'Hare, "cajohare/axion limits: Axionlimits." `https://cajohare.github.io/AxionLimits/`, July 2020.

[25] T. Kaluza, "Zum Unitätsproblem der Physik," *Sitzungsberichte der Königlich Preussischen Akademie der Wissenschaften*, pp. 966–972, Jan. 1921.

[26] T. Banks, M. Dine, and M. Graesser, "Supersymmetry, axions, and cosmology," *Physical Review D*, vol. 68, no. 7, 2003.

[27] A. Hook, "TASI Lectures on the Strong CP Problem and Axions," *PoS*, vol. TASI2018, p. 004, 2019.

[28] G. Lüders, "Proof of the TCP theorem," *Annals of Physics*, vol. 2, no. 1, pp. 1–15, 1957.

[29] G. 'T Hooft, "Symmetry breaking through Bell-Jackiw anomalies," *Physical Review Letters*, vol. 37, no. 1, p. 8–11, 1976.

[30] S. Weinberg, "The U(1) problem," *Physical Review D*, vol. 11, no. 12, p. 3583–3593, 1975.

[31] J. Negele, "Instantons, the QCD vacuum, and hadronic physics," *Nuclear Physics B - Proceedings Supplements*, vol. 73, no. 1, pp. 92–104, 1999.

[32] T. Schafer and E. V. Shuryak, "Instantons in QCD," *Reviews of Modern Physics*, vol. 70, no. 2, p. 323–425, 1998.

[33] M. Pospelov and A. Ritz, "Theta vacua, QCD sum rules, and the neutron electric dipole moment," *Nuclear Physics B*, vol. 573, no. 1, pp. 177–200, 2000.

[34] A. Hook, "Tasi lectures on the strong CP problem and axions," 2021.

[35] R. D. Peccei and H. R. Quinn, "CP conservation in the presence of pseudoparticles," *Phys. Rev. Lett.*, vol. 38, pp. 1440–1443, Jun 1977.

[36] D. B. Kaplan and A. V. Manohar, "Current-mass ratios of the light quarks," *Physical Review Letters*, vol. 56, no. 19, p. 2004–2007, 1986.

[37] W. A. Bardeen, R. D. Peccei, and T. Yanagida, "Constraints on variant axion models," *Nucl. Phys. B*, vol. 279, pp. 401–428, 1987.

[38] A. R. Zhitnitsky, "On Possible Suppression of the Axion Hadron Interactions. (In Russian)," *Sov. J. Nucl. Phys.*, vol. 31, p. 260, 1980.

[39] M. Dine, W. Fischler, and M. Srednicki, "A Simple Solution to the Strong CP Problem with a Harmless Axion," *Phys. Lett. B*, vol. 104, pp. 199–202, 1981.

[40] J. E. Kim, "Weak-interaction singlet and strong CP invariance," *Physical Review Letters*, vol. 43, no. 2, p. 103–107, 1979.

[41] M. Shifman, A. Vainshtein, and V. Zakharov, "Can confinement ensure natural CP invariance of strong interactions?," *Nuclear Physics B*, vol. 166, no. 3, pp. 493–506, 1980.

[42] M. Kawasaki and K. Nakayama, "Axions: Theory and Cosmological Role," *Ann. Rev. Nucl. Part. Sci.*, vol. 63, pp. 69–95, 2013.

[43] L. D. Duffy and K. van Bibber, "Axions as dark matter particles," *New Journal of Physics*, vol. 11, p. 105008, oct 2009.

[44] C. Colaboration, "New CAST limit on the axion–photon interaction," *Nature Physics*, vol. 13, no. 6, p. 584–590, 2017.

[45] M. S. Turner, "Windows on the axion," *Physics Reports*, vol. 197, no. 2, p. 67–97, 1990.

[46] G. G. Raffelt, *Astrophysical Axion Bounds*, pp. 51–71. Berlin, Heidelberg: Springer Berlin Heidelberg, 2008.

[47] G. Raffelt and A. Weiss, "Red giant bound on the axion-electron coupling reexamined," *Physical Review D*, vol. 51, no. 4, p. 1495–1498, 1995.

[48] M. M. Bertolami, B. Melendez, L. Althaus, and J. Isern, "Revisiting the axion bounds from the galactic white dwarf luminosity function," *Journal of Cosmology and Astroparticle Physics*, vol. 2014, p. 069, oct 2014.

[49] P. Sikivie, "Experimental tests of the "invisible" axion," *Physical Review Letters*, vol. 51, no. 16, p. 1415–1417, 1983.

[50] K. Van Bibber, N. R. Dagdeviren, S. E. Koonin, A. K. Kerman, and H. N. Nelson, "Proposed experiment to produce and detect light pseudoscalars," *Physical Review Letters*, vol. 59, no. 7, p. 759–762, 1987.

[51] A. A. Anselm, "Experimental test for arion photon oscillations in a homogeneous constant magnetic field," *Physical Review D*, vol. 37, no. 7, p. 2001–2004, 1988.

[52] P. Arias, J. Jaeckel, J. Redondo, and A. Ringwald, "Optimizing light-shining-through-a-wall experiments for axion and other weakly interacting slim particle searches," *Physical Review D*, vol. 82, no. 11, 2010.

[53] R. Ballou, G. Deferne, M. Finger, M. Finger, L. Flekova, J. Hosek, S. Kunc, K. Macuchova, K. Meissner, P. Pugnat, and et al., "New exclusion limits

on scalar and pseudoscalar axion like particles from light shining through a wall," *Physical Review D*, vol. 92, no. 9, 2015.

[54] S. Andriamonje, S. Aune, D. Autiero, K. Barth, A. Belov, B. Beltrán, H. Bräuninger, J. M. Carmona, S. Cebrián, J. I. Collar, T. Dafni, M. Davenport, L. D. Lella, C. Eleftheriadis, J. Englhauser, G. Fanourakis, E. F. Ribas, H. Fischer, J. Franz, P. Friedrich, T. Geralis, I. Giomataris, S. Gninenko, H. Gómez, M. Hasinoff, F. H. Heinsius, D. H. H. Hoffmann, I. G. Irastorza, J. Jacoby, K. Jakovčić, D. Kang, K. Königsmann, R. Kotthaus, M. Krčmar, K. Kousouris, M. Kuster, B. Lakić, C. Lasseur, A. Liolios, A. Ljubičić, G. Lutz, G. Luzón, D. Miller, A. Morales, J. Morales, A. Ortiz, T. Papaevangelou, A. Placci, G. Raffelt, H. Riege, A. Rodríguez, J. Ruz, I. Savvidis, Y. Semertzidis, P. Serpico, L. Stewart, J. Vieira, J. Villar, J. Vogel, L. Walckiers, K. Zioutas, and C. Collaboration, "An improved limit on the axion–photon coupling from the CAST experiment," *Journal of Cosmology and Astroparticle Physics*, vol. 2007, pp. 010–010, apr 2007.

[55] R. Daido, T. Kobayashi, and F. Takahashi, "Dark matter in axion landscape," *Physics Letters B*, vol. 765, p. 293–299, 2017.

[56] N. Du, *Recent Results with the ADMX Experiment*, p. 17–22. Springer Proceedings in Physics, 2020.

[57] R. Khatiwada, D. Bowring, A. S. Chou, A. Sonnenschein, W. Wester, D. V. Mitchell, T. Braine, C. Bartram, R. Cervantes, N. Crisosto, and et al., "Axion dark matter experiment: Detailed design and operations," *Review of Scientific Instruments*, vol. 92, no. 12, p. 124502, 2021.

[58] D. F. Jackson Kimball, S. Afach, D. Aybas, J. W. Blanchard, D. Budker, G. Centers, M. Engler, N. L. Figueroa, A. Garcon, P. W. Graham, and

et al., *Overview of the Cosmic Axion Spin Precession Experiment (CASPEr)*, p. 105–121. Springer Proceedings in Physics, 2020.

[59] A. Ejlli, F. Della Valle, U. Gastaldi, G. Messineo, R. Pengo, G. Ruoso, and G. Zavattini, "The pvlas experiment: A 25 year effort to measure vacuum magnetic birefringence," *Physics Reports*, vol. 871, pp. 1 – 74, 2020. The PVLAS experiment: A 25 year effort to measure vacuum magnetic birefringence.

[60] E. Zavattini, G. Zavattini, G. Ruoso, E. Polacco, E. Milotti, M. Karuza, U. Gastaldi, G., F., and R. e. a. Cimino, "Experimental observation of optical rotation generated in vacuum by a magnetic field," *Physical Review Letters*, vol. 96, no. 11, 2006.

[61] P. W. Graham, I. G. Irastorza, S. K. Lamoreaux, A. Lindner, and K. A. Van Bibber, "Experimental searches for the axion and axion-like particles," *Annual Review of Nuclear and Particle Science*, vol. 65, no. 1, p. 485–514, 2015.

[62] D. J. E. Marsh and A.-R. Pop, "Axion dark matter, solitons and the cusp–core problem," *Monthly Notices of the Royal Astronomical Society*, vol. 451, pp. 2479–2492, 06 2015.

[63] K. A. Beyer and S. Sarkar, "Ruling out light axions: The writing is on the wall," *SciPost Physics*, vol. 15, no. 1, 2023.

[64] G. Raffelt and L. Stodolsky, "Mixing of the photon with low-mass particles," *Physical Review D*, vol. 37, no. 5, p. 1237–1249, 1988.

[65] A. Mirizzi, G. G. Raffelt1, and P. D. Serpico, *Photon-Axion Conversion in Intergalactic Magnetic Fields and Cosmological Consequences*, pp. 115–134. Berlin, Heidelberg: Springer Berlin Heidelberg, 2008.

[66] C. Csáki, N. Kaloper, and J. Terning, "Dimming supernovae without cosmic acceleration," *Physical Review Letters*, vol. 88, no. 16, 2002.

[67] K. Greisen, "End to the cosmic-ray spectrum?," *Phys. Rev. Lett.*, vol. 16, pp. 748–750, Apr 1966.

[68] G. T. Zatsepin and V. A. Kuz'min, "Upper Limit of the Spectrum of Cosmic Rays," *Soviet Journal of Experimental and Theoretical Physics Letters*, vol. 4, p. 78, Aug. 1966.

[69] C. Csaki, N. Kaloper, M. Peloso, and J. Terning, "Super GZK photons from photon axion mixing," *JCAP*, vol. 05, p. 005, 2003.

[70] I. G. Irastorza and J. Redondo, "New experimental approaches in the search for axion-like particles," *Progress in Particle and Nuclear Physics*, vol. 102, p. 89–159, 2018.

[71] A. J. Millar, J. Redondo, and F. D. Steffen, "Dielectric haloscopes: sensitivity to the axion dark matter velocity," *Journal of Cosmology and Astroparticle Physics*, vol. 2017, p. 006, oct 2017.

[72] J. T. Mendonça, "Axion excitation by intense laser fields," *Europhysics Letters*, vol. 79, p. 21001, jul 2007.

[73] B. Dobrich and H. Gies, "Axion-like-particle search with high-intensity lasers," *JHEP*, vol. 10, p. 022, 2010.

[74] K. Beyer, G. Marocco, R. Bingham, and G. Gregori, "Light-shining-through-wall axion detection experiments with a stimulating laser," *Physical Review D*, vol. 105, no. 3, 2022.

[75] L.-W. Wei, "Towards the first axion search results of the any light particle search II experiment," in *Proceedings of XVIII International Conference*

on Topics in Astroparticle and Underground Physics — PoS(TAUP2023), TAUP2023, p. 049, Sissa Medialab, Jan. 2024.

[76] T. Tajima and J. M. Dawson, "Laser electron accelerator," *Physical Review Letters*, vol. 43, no. 4, p. 267–270, 1979.

[77] D. A. Burton and A. Noble, "Plasma-based wakefield accelerators as sources of axion-like particles," *New Journal of Physics*, vol. 20, no. 3, p. 033022, 2018.

[78] J. Mendonca, J. Rodrigues, and H. Tercas, "Axion production in unstable magnetized plasmas," *Physical Review D*, vol. 101, no. 5, 2020.

[79] X. Bai, M. J. Jewell, J. Echevers, K. van Bibber, A. Droster, M. H. Esmat, S. Ghosh, E. Graham, H. Jackson, C. Laffan, S. K. Lamoreaux, A. F. Leder, K. W. Lehnert, S. M. Lewis, R. H. Maruyama, R. D. Nath, N. M. Rapidis, E. P. Ruddy, M. Silva-Feaver, M. Simanovskaia, S. Singh, D. H. Speller, S. Zacarias, and Y. Zhu, "Dark matter axion search with haystac phase II," *Phys. Rev. Lett.*, vol. 134, p. 151006, Apr 2025.

[80] M. Lawson, A. J. Millar, M. Pancaldi, E. Vitagliano, and F. Wilczek, "Tunable axion plasma haloscopes," *Physical Review Letters*, vol. 123, no. 14, 2019.

[81] E. Esarey, C. B. Schroeder, and W. P. Leemans, "Physics of laser-driven plasma-based electron accelerators," *Reviews of Modern Physics*, vol. 81, no. 3, p. 1229–1285, 2009.

[82] P. Tomassini, D. Terzani, F. Baffigi, F. Brandi, L. Fulgentini, P. Koester, L. Labate, D. Palla, and L. A. Gizzi, "High-quality 5 GeV electron bunches with resonant multi-pulse ionization injection," *Plasma Physics and Controlled Fusion*, vol. 62, p. 014010, oct 2019.

[83] B. Miao, J. Shrock, L. Feder, R. Hollinger, J. Morrison, R. Nedbailo, A. Picksley, H. Song, S. Wang, J. Rocca, and et al., "Multi-gev electron bunches from an all-optical laser wakefield accelerator," *Physical Review X*, vol. 12, no. 3, 2022.

[84] T. Maruyama, A. B. Balantekin, M.-K. Cheoun, T. Kajino, and G. J. Mathews, "Axion production from landau quantization in the strong magnetic field of magnetars," *Physics Letters B*, vol. 779, pp. 160–165, 2018.

[85] N. Huang, H. Deng, B. Liu, D. Wang, and Z. Zhao, "Features and futures of x-ray free-electron lasers," *The Innovation*, vol. 2, no. 2, p. 100097, 2021.

[86] K. Bhattacharya and P. B. Pal, "Neutrinos and magnetic fields: A Short review," *Proc. Indian Natl. Sci. Acad. A*, vol. 70, no. 1, pp. 145–161, 2004.